Dielectric Elastomer Actuators for Binary Robotics and Mechatronics

by

Jean-Sébastien Plante

Bachelor of Mechanical Engineering with
Concentration in Concurrent Engineering
Université de Sherbrooke, 1998

Master of Science, Mechanical Engineering
Université de Sherbrooke, 2001

Submitted to the Department of Mechanical Engineering
in partial fulfillment of the requirements for the degree of
Doctor of Philosophy in Mechanical Engineering

at the

Massachusetts Institute of Technology

February 2006

© Massachusetts Institute of Technology
All Rights Reserved

Signature of Author . . . . . .
Department of Mechanical Engineering
January 15, 2006

Certified by . . . . . .
Steven Dubowsky
Professor of Mechanical Engineering
Thesis Supervisor and Committee Chairman

Accepted by . . . . . .
Professor Lallit Anand
Chairman, Committee on Graduate Studies

Dielectric Elastomer Actuators for Binary Robotics and Mechatronics

by

Jean-Sébastien Plante

Submitted to the Department of Mechanical Engineering
on January 15, 2006, in partial fulfillment of the
requirements for the degree of
Doctor of Philosophy in Mechanical Engineering

ABSTRACT

Future robotics and mechatronics applications will require systems that are simple, robust, lightweight and inexpensive. A suggested solution for future systems is binary actuation. Binary actuation is the mechanical analogy to digital electronics, where actuators "flip" between two discrete states. Systems can be simple since low-level feedback control, sensors, wiring and electronics are virtually eliminated. However, conventional actuators, such as DC motors and gearbox are not appropriate for binary robotics because they are complex, heavy, and expensive.

This thesis proposes a new actuation technology for binary robotics and mechatronics based on dielectric elastomer (DE) technology. DE actuators are a novel class of polymer actuators that have shown promising low-cost performance. These actuators were not well understood and, as a result, faced major reliability problems.

Fundamental studies conducted in this thesis reveal that reliable, high performance DE actuation based on highly viscoelastic polymers can be obtained at high deformation rates, when used under fast, intermittent motion. Also, analytical models revealed that viscoelasticity and current leakage through the film govern performance. These results are verified by an in-depth experimental characterizion of DE actuation.

A new DE actuator concept using multi-layered diamond-shaped films is proposed. Essential design tools such as reliability/performance trade-offs maps, scaling laws, and design optimization metrics are proposed.

A unit binary module is created by combining DE actuators with bistable structures to provide intermittent motion in applications requiring long-duration state-holding. An application example of binary robots for medical interventions inside Magnetic Resonance Imaging (MRI) systems illustrates the technology's potential.

Thesis Supervisor: Steven Dubowsky, Professor of Mechanical Engineering

ACKNOWLEDGEMENTS

My past 3 years at MIT have been a wonderful experience. I would like to thank many people who contributed to this adventure:

MIT related:

- First and foremost, the entire MIT community and excellent teaching staff.
- My thesis supervisor, Professor Dubowsky. His wisdom showed me a lot of things about myself, research, science and life. Thanks.
- My committee members, Professors Asada and Abeyaratne, for their great guidance during this work.
- Professors Boyce and Anand for their valuable discussion. Professor Hunter for letting my use his fabrication equipment. Thanks to Nicaulas Sabourin for his laser cutting expertise.
- The entire crew of the Field and Space Robotics Laboratory. In particular my lab partner John Vogan whose face is now associated with the smell of burning Dielectric Elastomer actuators... Dr. Karl Iagnemma, Dr. Matt Lichter and Lauren Devita for help in technical writing. Sam Korb, Sam Kesner, and Emmanuel Sin for their help in experimental work.
- Dr. Tyge Schioler and future Dr. Matt Santer from Cambridge University for their joyful collaboration.
- The following financial sponsors: Cambridge MIT Institute (CMI), Center for Integration of Medicine and Innovative Technology (CIMIT), NASA Institute for Advanced Concept (NIAC), Université de Sherbrooke and Fond de recherche sur la nature et les technologies.

Non-MIT related:

- My wife Caroline, my soul and conscience.
- My family: André, Gérald E. and Micheline for their support.
- All my friends.
- Professors Martin Brouillette and François Charron from Université de Sherbrooke.

I dedicate this work to my beloved daughter Cattleya.

TABLE OF CONTENTS

ABSTRACT 2

ACKNOWLEDGEMENTS 3

TABLE OF CONTENTS 4

LIST OF FIGURES 7

LIST OF TABLES 12

CHAPTER 1: INTRODUCTION 13
1.1 Motivation 13
1.2 Background Literature 17
1.2.1 Binary Actuation 17
1.2.2 DE Actuator Modeling 18
1.2.3 DE Failure Problems 21
1.2.4 DE Actuator Design 23
1.3 Contributions of this Thesis 25
1.4 General Constraints and Assumptions 26
1.5 Thesis Organization 26

CHAPTER 2: FOUNDATION OF DIELECTRIC ELASTOMER ANALYSIS 28
2.1 Introduction 28
2.2 Diamond Actuator Concept 28
2.3 Continuum Mechanics: Kinematics 34
2.3.2 Diamond Actuators 38
2.3.3 Ideal Actuators 41
2.4 Continuum Mechanics: Stresses 43
2.4.1 Ogden Model 44
2.4.2 Bergstom-Boyce Model 45

CHAPTER 3: CHARACTERIZATION AND MODELING OF FUNDAMENTAL MECHANISMS OF DIELECTRIC ELASTOMER ACTUATORS 51
3.1 Introduction 51
3.2 Experimental Characterization 51
3.2.1 Experimental Setup 51
3.2.2 Experimental Results 57
3.3 Viscoelasticity Model 64
3.3.1 Analytical Development 64
3.3.2 Experimental Validation 69
3.4 Current Leakage Model 72

3.4.1 Analytical Development 72
3.4.2 Experimental Validation 79
3.5 Chapter Summary 80

CHAPTER 4: MODELING AND ANALYSIS OF FUNDAMENTAL FAILURE MODES OF DIELECTRIC ELASTOMER ACTUATORS 82
4.1 Introduction 82
4.2 Analytical Model 82
4.2.1 Ideal Actuator Model 83
4.2.2 Failure Criteria 85
4.2.3 Failure Predictions 89
4.3 Experiments 92
4.3.1 Data Acquisition 92
4.3.2 Experimental Results 93
4.4 Model Validation 96
4.4.1 Ideal Actuators 96
4.4.2 Diamond Actuators with External Load 98
4.5 Chapter Summary 100

CHAPTER 5: THE DESIGN OF DIELECTRIC ELASTOMER ACTUATORS 102
5.1 Introduction 102
5.2 Technical Benchmark: DE Actuators vs. Voice Coils 102
5.2.1 Performance Metrics 103
5.2.2 Physical Mechanisms 104
5.3 Design Trade-Off 105
5.4 Performance Scaling Laws 108
5.4.1 Stretch 108
5.4.2 Stretch Rate and Velocity 108
5.4.3 Force 109
5.4.4 Work Output 111
5.4.5 Verification 113
5.5 Design Optimization 114
5.6 Film Thickness Selection 116
5.6.1 Advantages of Thin Films 117
5.6.2 Advantages of Thick Films 117
5.7 Film Edge Design 119
5.8 Chapter Summary 121

CHAPTER 6: INTEGRATION TO BINARY ROBOTIC SYSTEMS 122
6.1 Introduction 122
6.2 Problem Definition 122
6.3 Bistable Actuation Concepts 123
6.3.1 Flip-Flop 123
6.3.2 Mini-Might 127
6.4 Application to MRI Manipulation 132

6.4.1 System Requirements 134
6.4.2 Proposed Design 135
6.4.3 7 DOF Prototype 139
6.5 Chapter Summary 141

CHAPTER 7: CONCLUSIONS 142
7.1 Contributions of this Thesis 142
7.2 Suggestions for Future Work 144

REFERENCES 145

APPENDIX A: DETAILS OF THE DIAMOND ACTUATOR 154

APPENDIX B: POLYMER FILM STRETCHING 160

APPENDIX C: OGDEN PARAMETERS 164

APPENDIX D: BERGSTROM-BOYCE PARAMETERS 168

APPENDIX E: IDEAL ACTUATOR PASSIVE REGION MODEL 172

APPENDIX F: SPACE EXPLORATION MICROBOTS 182

LIST OF FIGURES

Figure 1: Computer Simulation of FSRL's 6 legged walking rover climbing Mars surface [44]. 14
Figure 2: SMA binary manipulator prototype [76]. 15
Figure 3: Electromagnetic binary manipulator prototype [26]. 15
Figure 4: DE binary manipulator prototype [84]. 16
Figure 5: DE actuator operating principle [38]. 19
Figure 6: Maxwell stresses acting on DE actuators [80]. 20
Figure 7: DE actuator for binary actuation developed in 2002 [84]. 24
Figure 8: Rolled DE actuator [55]. 28
Figure 9: Diamond actuator schematic. 30
Figure 10: Film layer sub-assembly. 31
Figure 11: Multi-layer diamond actuator assembly. 31
Figure 12: Diamond actuator prototype under 100% strains. 32
Figure 13: Illustration of a deformation, adapted from [30]. 34
Figure 14: Deformations of a general DE film. 38
Figure 15: Deformations of a diamond actuator. 39
Figure 16: Actuation stretches of diamond actuators. 40
Figure 17: Ideal actuator. 42
Figure 18: Deformations of the active region of an ideal actuator. 42
Figure 19: Bergstrom-Boyce rheological model. 46
Figure 20: Bergstrom-Boyce kinematics, adapted from [6]. 47
Figure 21: Single active layer diamond actuator used for work cycle experiments. 52
Figure 22: Schematic of actuator dynamometer setup 53
Figure 23: Photograph of actuator dynamometer setup. 53
Figure 24: Typical input commands for work cycle experiments. 54
Figure 25: Typical current of a work cycle experiment. 55
Figure 26: Typical force of a work cycle experiment. 55
Figure 27: Example of data vector truncation. 57
Figure 28: Force difference map. 58
Figure 29: Power map. 59

Figure 30: Current consumption map. 60
Figure 31: Current consumption map, isolevel view, units in milliampere. 60
Figure 32: Cycle work output map. 61
Figure 33: Cycle work output map, isolevel view, units in Joule. 62
Figure 34: Cycle efficiency map. 63
Figure 35: Cycle efficiency map, isolevel view, units in percentage. 63
Figure 36: Viscoelastic model structure. 64
Figure 37: Interstitial frame rheological model. 66
Figure 38: Structural and interstitial frames model, prediction (dark) vs. experiment (light). 67
Figure 39: Free body diagram of diamond actuator frame. 67
Figure 40: Viscoelastic model, prediction (dark) vs. experiment (light), case 1. 70
Figure 41: Viscoelastic model, prediction (dark) vs. experiment (light), case 2. 70
Figure 42: Viscoelastic model, prediction (dark) vs. experiment (light), case 3. 71
Figure 43: Viscoelastic model, prediction (dark) vs. experiment (light), case 4. 71
Figure 44: Viscoelastic model, prediction (dark) vs. experiment (light), case 5. 72
Figure 45: DE actuator thermodynamic system. 74
Figure 46: Diffusive current leakage process. 75
Figure 47: Current leakage model predictions (white) vs. experiments (grey). 79
Figure 48: Current consumption of considered mechanisms: (a) variable capacitance, (b) conduction leakage, (c) diffusion leakage, (d) mechanical power output and (e) viscous dissipation. 80
Figure 49: Ideal actuator decomposed into active and passive regions. 84
Figure 50: Failure modes of DE actuators. 86
Figure 51: Film geometry during pull-in instability. 87
Figure 52: Example of pull-in failure criterion. 88
Figure 53: Calculated actuation area expansion at failure as a function of area pre-stretch at very high stretch rates ($\dot{\lambda}_{UNI}$ =1.8 s^{-1}). 89
Figure 54: Calculated actuation area expansion at failure as a function of area pre-stretch at high stretch rates ($\dot{\lambda}_{UNI}$ =0.094 s^{-1}). 90
Figure 55: Calculated actuation area expansion at failure as a function of area pre-stretch at low stretch rates ($\dot{\lambda}_{UNI}$ =3.3x10^{-4} s^{-1}). 90

Figure 56: Experimental breakdown voltages for rigid and compliant electrodes measured at high stretch rate ($\dot{\lambda}_{UNI}$ =0.094 s^{-1}). 94

Figure 57: Experimental ultimate actuation area expansion vs. pre-stretch area expansion at high stretch rate ($\dot{\lambda}_{UNI}$ =0.094 s^{-1}). 95

Figure 58: Failure analytical predictions for high stretch rate ($\dot{\lambda}_{UNI}$ =0.094 s^{-1}) compared with experimental values. 97

Figure 59: Failure analytical predictions for low stretch rate ($\dot{\lambda}_{UNI}$ =3.3x10^{-4} s^{-1}) compared with experimental values. 97

Figure 60: Failure analytical predictions for high stretch rate ($\dot{\lambda}_{UNI}$ =0.094 s^{-1}) with loading stress compared with experimental values of 10 diamond actuators. 99

Figure 61: Failure analytical predictions for low stretch rate ($\dot{\lambda}_{UNI}$ =3.3x10^{-4} s^{-1}) with loading stress compared with experimental values of 10 diamond actuators. 99

Figure 62: Steady state transducer systems: (a) voice coil, (b) DE actuator. 104

Figure 63: DE actuator design domain map. 106

Figure 64: Diamond actuator scaling: 107 mm vs. 54 mm 113

Figure 65: Effect of structural efficiency on specific work output. 116

Figure 66: Effect of film thickness on current consumption. 118

Figure 67: Film edge crack photograph (4X). 119

Figure 68: Film edge cracking mechanism. 120

Figure 69: Flip-flop bistable mechanism. 124

Figure 70: Flip-flop bistable actuator concept. 124

Figure 71: Flip-flop bistable actuator prototype. 125

Figure 72: Flip-flop bistable actuator force profiles. 125

Figure 73: Mini-might concept, assembled and exploded views. 127

Figure 74: Mini-might dimensions in millimeters: (a) closed, (b) opened. 128

Figure 75: Mini-might mechanism details. 129

Figure 76: Mini-might opening sequence. 130

Figure 77: Mini-might bistable actuator prototype. 131

Figure 78: Mini-might bistable actuator force profiles. 131

Figure 79: Transperinal Brachytherapy schematic. 133

Figure 80: Perforated guide-plate for manual Brachytherapy. 134

Figure 81: Workspace for needle insertion in transperinal prostate cancer treatment. (Courtesy of Daniel Katcher, Brigham and Women Hospital). 135

Figure 82: 30 DOF binary crane structure [70]. 136
Figure 83: 24 DOF snake-like MRI manipulator concept (in millimeters). 137
Figure 84: End effector's x, y, z position of the snake-like MRI manipulator. 138
Figure 85: End effector's θ_x angle of the snake-like MRI manipulator. 138
Figure 86: End effector's θ_y angle of the snake-like MRI manipulator. 139
Figure 87: 7 DOF MRI manipulator prototype. 140
Figure 88: Range of motion of the 7 DOF MRI manipulator prototype. 141
Figure 89: Engineering drawing, structural frame, 107 mm actuator. 155
Figure 90: Engineering drawing, interstitial frame, 107 mm actuator. 155
Figure 91: Engineering drawing, structural frame, 54 mm actuator. 156
Figure 92: Engineering drawing, interstitial frame, 54 mm actuator. 156
Figure 93: Engineering drawing, interstitial frame array, 54 mm actuator. 158
Figure 94: Interstitial frames assembly jig. 158
Figure 95: Adhesive in interstitial frame hinges. 159
Figure 96: Experimental film stretching setup. 161
Figure 97: Film stretching sequence. 162
Figure 98: Experimental vs. constant volume film thickness. 163
Figure 99: Uniaxial deformation of a rectangular sample. 165
Figure 100: Experimental stress/stretch curves for uniaxial extension of VHB 4905/4910 at different stretch rates. The solid curves superposed on (a), (b) and (c) are curve-fitted Ogden models. 167
Figure 101: Bergstrom-Boyce network A parameters curve fit. 170
Figure 102: Deformation of the passive region model. 173
Figure 103: Example of stretch distribution in the passive region. 175
Figure 104: Example of engineering stress distribution in the passive region. 176
Figure 105: Passive region's deformed shape computed with Adina® when inner face is: (a) discontinuous, and (b), continuous (not to scale). 177
Figure 106: Planar stress in the active region vs. actuation stretch for analytical and FE models. 178
Figure 107: Schematic of the planar stress in the active region vs. actuation stretch. 179
Figure 108: Microbots mission concept. Image rendering by Gus Frederick. 183
Figure 109: Microbots hopping mechanism. 184

Figure 110: Changing the attitude of the Microbots using the directional hopping mechanism concept. 184
Figure 111: DE actuator hopping mechanism. 185
Figure 112: Sequence of images of the mobility system prototype performing a jump. Total cycle time is about 20 seconds. 186

LIST OF TABLES

Table 1: Specifications of a 107 mm diamond actuator with 3 active layers. 33
Table 2: Specifications of a 54 mm diamond actuator with 6 active layers. 33
Table 3: Current leakage model parameters 78
Table 4: Experimental actuation area expansion at failure for low stretch rate, $\dot{\lambda}_{UNI}$ =3.3x10^{-4} s^{-1} 95
Table 5: Scaling laws verification..... 114
Table 6: Best film bonding interface parameters. 121
Table 7: Flip-flop bistable actuator specifications. 126
Table 8: Mini-might bistable actuator specifications..... 132
Table 9: Ogden model parameters from uniaxial tests. 166
Table 10: Bergstrom-Boyce network B parameters..... 171

CHAPTER

1

INTRODUCTION

1.1 Motivation

Future robotics and mechatronics applications will require devices that are simple, robust, lightweight and inexpensive. Current systems using conventional actuators such as electric motors with gears are complex, expensive, heavy, and have high power consumption. A suggested solution for future systems is the concept known as *binary actuation*. Binary actuation can be thought of as the mechanical analogy to digital electronics, where each actuator "flips" between one of two possible discrete states. Systems can be simple since low-level feedback control is virtually eliminated, along with the associated sensors, wiring, and electronics [3,42]. Such devices are fundamentally robust, lightweight, inexpensive, and easy to control. Further benefits of binary actuation using bistable mechanisms are that power consumption is eliminated while the system is in a fixed configuration since actuators can be turned off.

A number of potential applications of binary actuation ranging from space exploration to industrial systems have been proposed [14,16,42]. Figure 1 shows such an application consisting of a 6 legged walking robot for planetary exploration. Each leg is composed of 21 binary joints, each actuated by a binary actuator (not shown for clarity). Laboratory experimental systems along with computational simulations have been developed to demonstrate the principles of binary actuation [42,43]. These studies have shown that real applications will require 10's to 100's of binary actuators, and that the

analysis, planning, and control of such systems are well within the capabilities of modern computation.

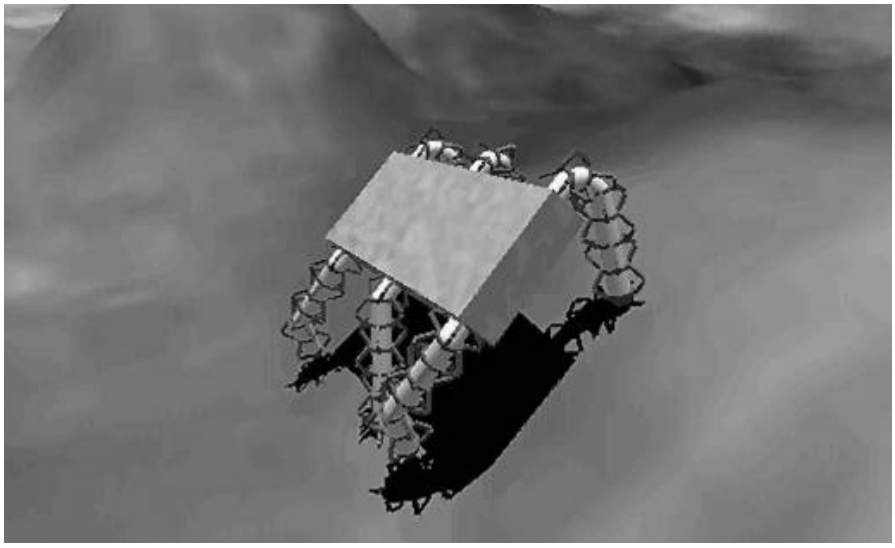

Figure 1: Computer Simulation of FSRL's 6 legged walking rover climbing Mars surface [44].

To date, only a few practical applications of binary actuation technology have been developed. Conventional actuators are too large, complex, expensive and heavy to implement in large numbers [24]. Therefore, for the concept of binary robotics to be successful, new cheap, simple, and lightweight actuators must be developed.

Alternative actuation technologies have been considered but all show at least one weakness for binary robotic systems [26]. Shape Memory Alloys (SMA) relies on volume contractions driven by alloy phase changes, a very inefficient process. They are also relatively slow and sensitive to external temperature changes. Ionic polymers change volume when their polymer chains absorb or swell ions. Such systems must be kept in aqueous environments and are slow. Optimized linear electromagnetic systems (solenoids) experienced overheating issues and were heavy. Examples of past binary manipulators developed with SMA and electromagnetic technologies are shown in Figure 2 and Figure 3.

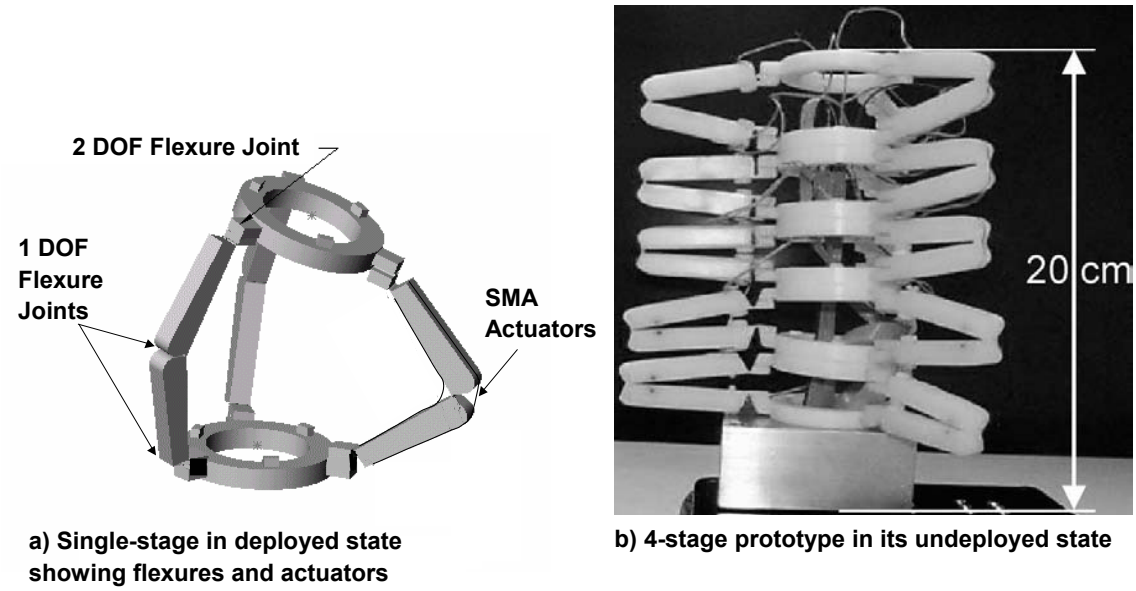

Figure 2: SMA binary manipulator prototype [76].

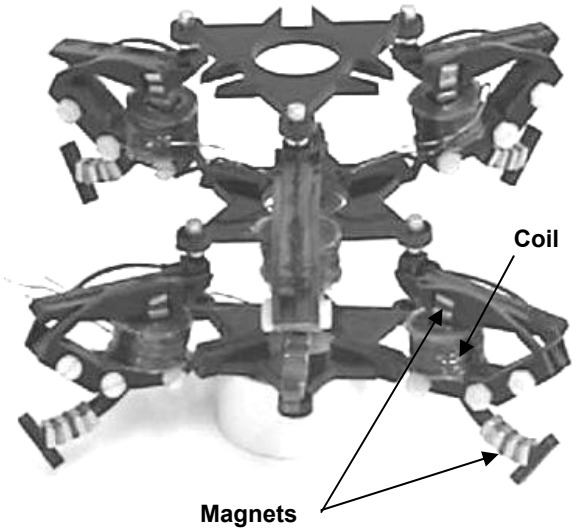

Figure 3: Electromagnetic binary manipulator prototype [26].

In contrast with most alternative actuation technologies, Dielectric Elastomer (DE) actuators have shown good performance and are inherently inexpensive [49,58]. Possible applications of DE actuators vary from medical devices to space robotics. In particular, laboratory demonstrations of blood pumps, imaging systems and

reconfigurable large space telescopes were studied [24,25,80,84]. A prototype of one such actuated telescope mirror is shown in Figure 4.

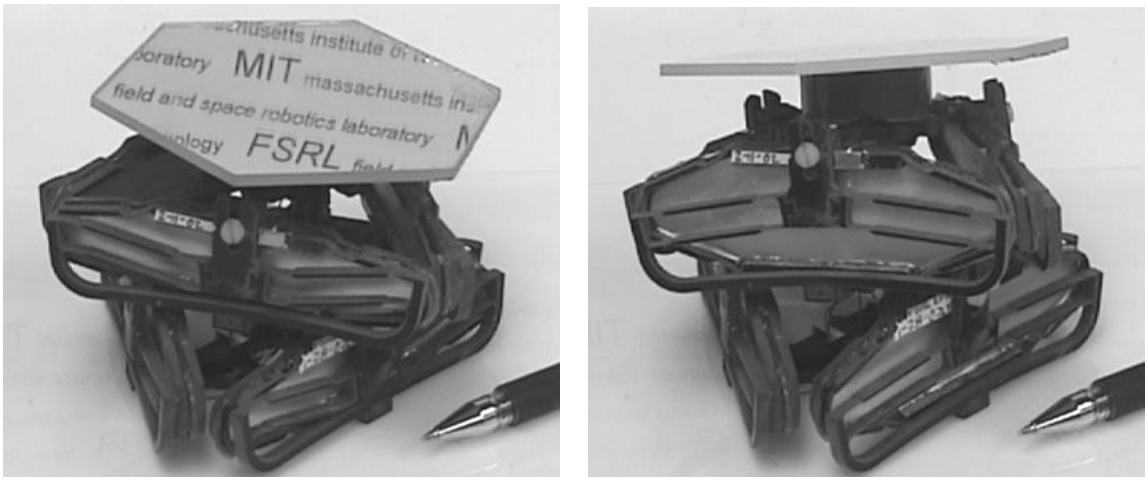

Figure 4: DE binary manipulator prototype [84].

Dielectric Elastomer actuators are lightweight, simple, have large displacements and good force capabilities [79,55,32]. Early assessments of ideal DE performance based on 3M's VHB 4905/4910 elastomer, a common material used in DE actuators, suggested:

- extensions of up to 3 times their initial length [79];
- bulk material force-to-weight ratio of 1000:1 [79];
- bulk material specific energy densities of 3-4 J/g [55];

However, practical systems performance is far from the ideal numbers reported above [28,32,36]. Early practical DE actuators showed low reliability, short lifetimes, and low efficiencies [80,84]. Such practical implementation problems suggested that DE actuators were not completely understood and consequently that their design was not capturing their true physics.

The purpose of this thesis is to make binary actuation based on DE actuators practical. To do so, the fundamental mechanisms of DE actuation need to be fully understood. Specifically, the mechanisms responsible for the reliability and performance

of practical actuators need to be quantified. Such an understanding is the key to developing DE actuators for binary actuation that reflect DE physical reality.

1.2 Background Literature

This section presents a review of literature on binary actuation and the principal challenges to DE actuation.

1.2.1 Binary Actuation

Binary actuation for mechanical systems was first proposed in the 1960's and 70's [3,67]. Most work done on the subject in the last 30 years has focused on the trajectory planning of binary manipulators which involves searching through a discrete set of configurations. Researchers have provided important results on the kinematics and inverse kinematics of binary mechanisms [14,16,17]. Real time computation has been demonstrated with combinatorial search algorithms and genetic algorithms [42,45].

These early studies as well as many recent ones focused on kinematically constrained actuator arrangements [17,45,64]. In Gruebler's law terms, a kinematically constrained system is one where the number of degree of freedom is equal to the number of actuated joints and each actuator can be actuated without conflict with any other actuators [22]. . The prototypes of Figure 2, Figure 3, and Figure 4 are all kinematically constrained arrangements. After more than 30 years of development, even the simplest kinematically constrained binary systems are still impractical due to inadequate actuation technology.

More recently, over-constrained binary systems were studied. In Gruebler's law terms, an over-constrained system is one where there are more actuated joints than degrees of freedom [22]. Flipping one actuator requires deformation of the system and will generally work only if additional compliance is introduced [51,88]. Limited

experimental work was conducted on over-constrained systems. One experiment studied a single degree-of-freedom (DOF) joint powered by pneumatic cylinders coupled with springs. The system showed the expected dynamic behavior but was bulky, expensive and impractical due to current actuation technologies [88].

Theoretically, over-constrained systems constitute the most general case of binary actuation with kinematically constrained systems representing a small subset where the kinematics allows the actuators to be decoupled. By using redundant actuators, over-constrained systems can potentially develop higher total system stiffness than kinematically constrained systems. Positioning errors could also decrease as the number of actuators increase because of the "elastic average" created by actuator redundancy [72].

1.2.2 DE Actuator Modeling

In general, reported performance numbers of DE actuators were isolated best-case values. There was no published experimental data showing how working conditions influence performance. In fact, the governing physics of DE actuators has not been completely understood.

The basic mechanism of DE actuators is the electromechanical coupling between electric charges and mechanical forces. This coupling results from two physical mechanisms: Maxwell Stresses and Electrostriction[1]. Studies have shown the electrostriction contribution to be negligible at room temperature and frequencies of about 1 Hz for 3M's VHB 4905/4910, a common material used in DE actuators [33,46]. Maxwell stresses are generated on an elastomer film's surface via electrically charged deformable electrodes and are responsible for DE actuator deformations, see Figure 5.

[1] Electrostriction results from a material's dipole reorientation in an electric field.

The Maxwell stresses are compressive in nature and therefore the film must be pre-stretched to avoid buckling.

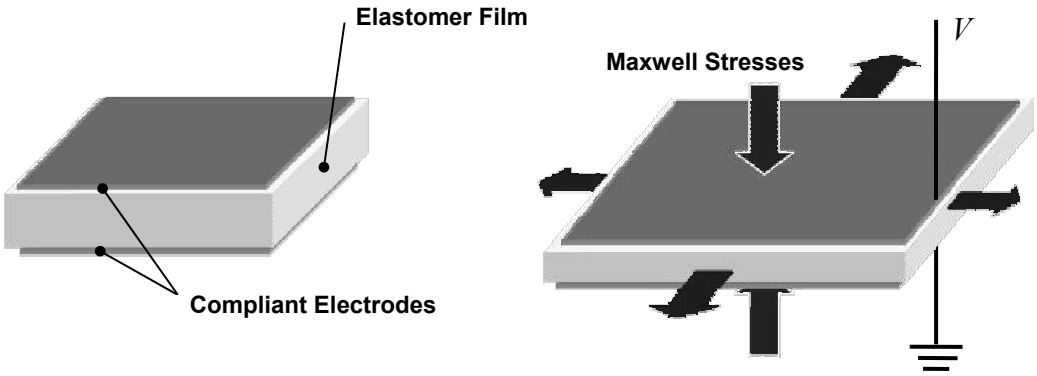

Figure 5: DE actuator operating principle [38].

Maxwell stresses on DE electrodes have two components: a compressive and a planar stress, both generated by the charged electrodes, see Figure 6 [38,57]. The combined actions of those stresses can be expressed by an equivalent Maxwell pressure, P, given by [38,57]:

$$P = \varepsilon_d \varepsilon_0 \left(\frac{V}{u} \right)^2 \tag{1.1}$$

where ε_0 is the free-space permittivity (8.85×10^{-12} F/m), ε_d is the material's dielectric constant, V is the voltage applied across the electrodes, and u is the film thickness.

Equation (1.1) is valid for uniform electrical charge distribution on infinitely large electrodes and uniform film thickness. It should be noted that Eq. (1.1) represents only an approximation of the real film loading [48]. Its simplicity and accuracy makes it the generally accepted electromechanical coupling model for most DE actuators.

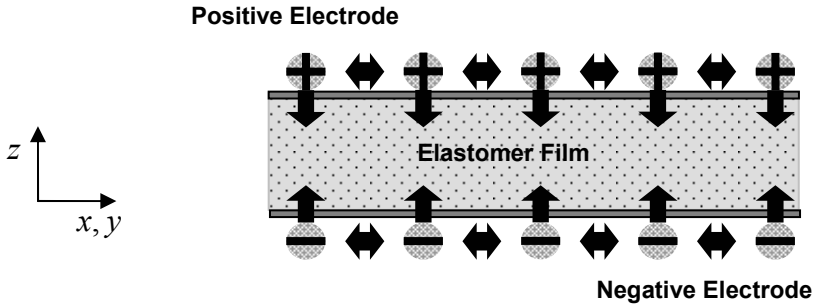

Figure 6: Maxwell stresses acting on DE actuators [80].

Early analyses of DE deformation used linear (Hookean) material models but were shown inadequate to describe the significant nonlinear behavior of DE actuation (large displacements and nonlinear elasticity) [37,57,74]. These issues can be addressed with continuum mechanics methods [2,30,53]. Accordingly, researchers have used hyper-elastic material models like the Mooney-Rivlin and Ogden models to study simple DE actuator shapes [24,25,32,59,85]. Those models were shown to be capable of representing experimental data of DE actuators under constant stretch rates (deformation rate). However, frequency response experiments have shown significant displacement attenuation with increasing frequency or stretch rate, with up to 90% attenuation at 10Hz [35,46]. This important stretch rate dependence is attributed to viscoelasticity and should obviously be accounted for in DE analysis.

Viscoelastic effects of DE films were briefly investigated using a Mooney-Rivlin hyper-elastic model coupled with a Maxwell viscosity model [40]. This analysis considered uniaxial deformation with stretches[2] of up to 1.8. Other similar studies were conducted up to stretches of 3.0 [87]. The deformation of expanding DE circles was studied using various hyper-elastic models coupled with quasi-linear viscoelasticity within Finite Element Models [85]. The extensions considered in these models were

[2] The term "stretch" is a measure of deformation used in continuum mechanics and defined by: $\lambda = \frac{l}{l_0}$.

substantially lower than typical DE actuators extensions that can reach stretches of 5.0. Most importantly, they addressed geometries that are not representative of practical actuators, and were not experimentally validated over real working conditions. Other material models of nonlinear viscoelastic materials undergoing large deformation have been developed but have not been applied to DE materials [6,7,20]. A detailed and comprehensive description of viscoelasticity's role on DE actuators performance has not been developed prior to this study.

Besides viscoelasticity, another important physical mechanism affecting DE actuator performance is even less understood: current leakage through the film. Such currents are measured experimentally but no physical explanation of their nature has yet been given and their quantitative impact on actuator efficiency is unknown [37,57,80,84].

In summary, proper DE performance models have yet to be developed and validated experimentally. The following fundamental effects need to be considered in these models:

1. very large deformations;
2. nonlinear elastic behavior;
3. viscoelasticity;
4. current leakage.

1.2.3 DE Failure Problems

The vast majority of DE actuator development so far has consisted of developing new actuator shapes and exploring potential applications [12,28,34,36,55,56,61,62,71,79,80,84]. After more than 10 years of research and impressive laboratory performance results, DE actuators are still not available commercially as off-the-shelf design components, presumably because of their reliability

problems. Indeed, experiments have shown "infant mortalities"[3] of 30%, shelf lives of about a week for high performance actuators built with highly pre-stretched films, and most importantly, erratic and misunderstood failures during operation [80,84].

The first investigations of DE failure focused on a failure mode called *pull-in*. A pull-in failure occurs when the Maxwell pressure becomes greater than the film's compressive stress. This positive feedback leads to an unstable compression of the elastomer material and catastrophic failure. This failure mode was investigated with linear (Hookean) stress/stretch models [37,57,74]. However, these models were inadequate and predicted pull-in failures at about half the extensions observed experimentally [55,79].

More recently, pull-in failure was briefly investigated using hyper-elastic continuum mechanics [85]. This study predicted pull-in to be of no concern because it should occur above the material dielectric strength. However, experimental evidence presented in this thesis shows pull-in to be an important and observable failure mode. Clearly, the circumstances leading to pull-in failures have not been understood.

The role of viscoelasticity on DE actuator failures has not yet been investigated. Previous studies addressed these failures by treating them as purely elastic systems [37,57,74].

The role of film dielectric strength on maximum extension was studied and its important effect on DE extension is illustrated by the figure of merit: $E^2 Y^{-1}$ where E is the maximum electric field or dielectric strength, and Y is the apparent Young's modulus (if the material was linear) [74]. Since the dielectric strength is squared, it strongly affects DE performance limits. Experimental results have shown that the dielectric strength of VHB 4905/4910 increases from about 40 MV/m to 240 MV/m when stretched to 36 times its initial area [33,60], a major positive impact when viewed in light of

[3] Immediate failure upon first voltage application.

$E^2 Y^{-1}$. Failure models including variable dielectric strength have not yet been developed.

In summary, past DE research has mostly addressed new applications rather than practical failure problems. Hence, failure modes still need to be identified and the conditions in which they occur have to be described. The impact of failure modes on DE performance levels is also unknown. Any attempt to study DE failure should address the following fundamental effects:

1. very large deformations;
2. nonlinear elastic behavior;
3. viscoelasticity;
4. variable dielectric strength.

1.2.4 DE Actuator Design

Prior to this thesis, DE actuators have been seen as simple nonlinear elastic materials with almost perfect electrical isolation properties. An example of a recently-studied actuator is shown in Figure 7. These actuators were used in the binary manipulator prototype of Figure 4. This particular actuator design uses a pre-stretched film preloaded by a pair of compliant frames. The Linear Bistable Element (LBE) counteracts the forces due to film stiffness in order to increase output strains. Such actuators are capable of bidirectional forces of about 0.5 N (for a single film layer) and output strains of about 60% [84]. Even if they used bistable components (LBE), these early actuators were not truly bistable because they had to be kept activated to maintain their extended position. This operation scheme was consistent with the understanding at that time and ignores the fundamental mechanisms of viscoelasticity and current leakage. As a result, DE actuators appeared impractical due to unexplainable failures and viscous relaxation.

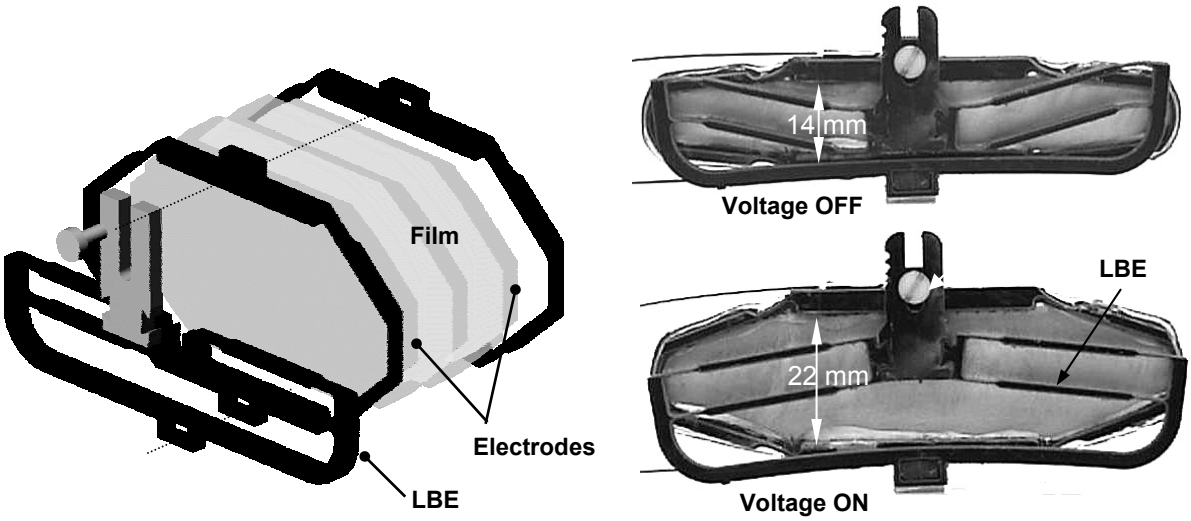

a) CAD representation showing film and electrodes

b) Prototype shown before and after actuation

Figure 7: DE actuator for binary actuation developed in 2002 [84].

DE actuator designs were not rigorously characterized in the literature. It was therefore difficult to compare various concepts and evaluate progress. For example, the principal design objective of any DE actuator is to optimize work output for a given actuator mass. This objective is of critical importance for mobile and weight sensitive applications but, prior to this thesis, there was no data to precisely described actuator work output performance [84]. Further, there were no useful design tools to help the designer size a DE actuator for a given application.

Even if incomplete, the early work on DE actuators led to important design principles:

- The positive effect of film pre-stretch on actuation performance [35,60].
- The potential output strain enhancement by using asymmetric pre-stretches. The idea is to highly pre-stretch the film in its passive direction and to leave it almost unstretched, and therefore soft, in its active direction [35,60].

- The use of nonlinear restoring forces to cancel the film stiffness in order to amplify actuator displacement [59,80]. By canceling the film stiffness, the actuator could, in theory, move freely until it fails.

In summary, a set of physics-based DE design tools did not exist, largely because DE actuator mechanics were not completely understood. Consequently, the question of how to design reliable, high performance DE actuators has been unanswered.

1.3 Contributions of this Thesis

This thesis develops fundamental physical models of DE actuation and addresses mechanical design issues essential to their successful application.

The critical problems of actuator reliability and failure mechanisms are addressed. Analytical models of the physical mechanisms of DE actuation are developed and their predictions are compared against experimental data to assess their validity. The performance of DE actuators is also characterized experimentally over a large range of working conditions.

These analytical models are used to improve the design of DE actuators through new design tools and system concepts. Tools like design domain maps for performance trade-offs, scaling laws and a design optimization metrics are developed. New design concepts that exploit the strengths and weakness of the technology are developed. In particular, a novel bistable mechanism is proposed to allow DE actuators to function intermittently, an essential condition for their reliability. An application example to MRI manipulation shows bistable DE actuators to be a valid approach to binary robotics and mechatronics.

1.4 General Constraints and Assumptions

The performance of DE actuators depends on the film material properties. Many polymer film materials were studied in the past 10 years, and the material giving the best performance in terms of energy output for a given film mass is 3M's VHB 4905/4910 [9,11,35,37,38,39,58,75,77,89]. Briefly, the key properties of this material are its large deformation capability and high dielectric strength. Moreover, VHB 4905/4910 is commercially available as an adhesive tape, and does not require elaborate fabrication processes such as mixing, degassing, centrifuging, and curing. Therefore, this thesis uses this material as a reference material.

The mechanical properties of VHB 4905/4910 are temperature sensitive, varying by three orders of magnitude from -50^{o} to 125^{o}C [89]. This thesis is limited to room temperature. Also, the mechanical properties are assumed isotropic before pre-stretching.

The film is incompressible. The rubber-like material VHB 4905/4910 has a Poisson's ratio of 0.49, which is very close to the incompressible value of 0.5 [1].

The film dielectric constant, ε_d, of VHB 4905/4910 was recently found to decrease with film stretching. Variation by a factor of up to two followed by partial recovery was reported [19]. No models have been proposed and more data is needed to fully understand this effect. Therefore, this thesis uses a fixed dielectric constant of ε_d=4.5 [33].

1.5 Thesis Organization

The thesis has seven chapters. Chapter 1 presents motivation and background for the thesis. It also describes the past work done to understand DE actuators and to address their failure problem. Chapter 2 presents ideas and concepts used in analysis throughout this thesis. Chapters 3 and 4 address fundamental modeling issues. Chapter 3 starts with

a detailed study of the physical mechanisms influencing DE performance and Chapter 4 follows by investigating the crucial question of DE actuator reliability. Chapter 5 addresses the question of how to design reliable, high performance DE actuators. New DE actuator design tools are developed from the fundamental results. Chapter 6 integrates DE actuators into binary robotic systems by using bistable mechanisms. An application example to Magnetic Resonance Imaging (MRI) manipulation illustrates the technology capabilities. Finally, Chapter 7 summarizes the thesis and suggests avenues for future research.

CHAPTER

2

FOUNDATION OF DIELECTRIC ELASTOMER ANALYSIS

2.1 Introduction

This chapter presents basic ideas used in DE actuators analyses throughout this thesis. First, the diamond actuator concept used as a reference actuator in most experimental work is presented. Second, the continuum mechanics modeling framework required to handle the large displacements and nonlinear material properties is presented.

2.2 Diamond Actuator Concept

As mentioned in Chapter 1, many DE actuator concepts have been proposed in the past ten years. The rolled and planar actuator classes have shown particularly good performance. The rolled actuator concept consists of wrapping a long DE film around a pre-loaded coil spring, see Figure 8 [34,55,56,62].

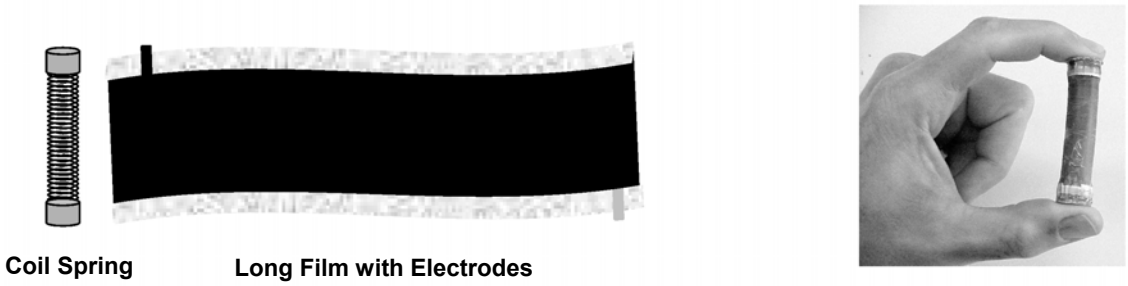

Figure 8: Rolled DE actuator [55].

The planar concept consists of bonding many individual planar film layers onto a preloaded compliant frame (i.e., see Figure 7 on page 24) [80,83,84]. The main advantage of these concepts is their ability to pack many active layers in a small space.

The performance of DE actuators depends greatly on actuator geometry. Hence, this thesis focuses on a specific class of planar actuators called diamond actuators. Such actuators consist in a 4 bar linkage geometry as shown in Figure 9. The film occupies the inside space of the diamond and is preloaded by a pair of elastic bands. Under voltage application, the Maxwell pressure compresses the film, causing its area to expand. As a result, the film planar area must increase because the film's volume is constant: $A_{act} > A_{pre}$. The choice of this actuator geometry is motivated by the following reasons:

- The diamond shape provides a uniform stress/stretch state during actuator deformation (this is demonstrated in the diamond actuator kinematical development presented in Section 2.3.2). Hence, the film is loaded uniformly everywhere and thus the entire film's mass contributes equally and optimally to work output production. In contrast, rolled actuators are under 3D states of stress. Their high film pre-stretch in the hoop direction translates into a gradually increasing compressive stress from the outer radius to the inner radius, similar to a thick-wall cylindrical pressure vessel. Moreover, uniform stress/stretch eases actuator modeling because Finite Element Models are not required.
- The diamond shape has large output strains for a given film area expansion [80][1]. Diamond actuators thus exploit the large deformations capabilities of VHB 4905/4910. Large strains maximize work output

[1] Part of the development of the diamond frame actuator was done in collaboration with John Vogan. The reader is referred to his thesis to learn more about the nonlinear restoring force of diamond actuators [80].

production and are also very important to developing high performance binary robots [43,76].

- The diamond shape provides a convenient mounting location for preloading elastic bands giving a nonlinear restoring force. The elastic bands act like an over-the-center mechanism acting on the central hinges, see Figure 9. The moment arm distance with the central hinges increases with actuation, $d_{act} > d_{pre}$, thereby increasing the restoring moment. Such nonlinear restoring forces cancel the film stiffness making the film apparently free-floating and thus maximize actuation strains [59,80,84]. This unique feature of diamond actuators eliminates the need for additional complex, nonlinear springs to compensate the film stiffness such as used in early DE actuators [84].

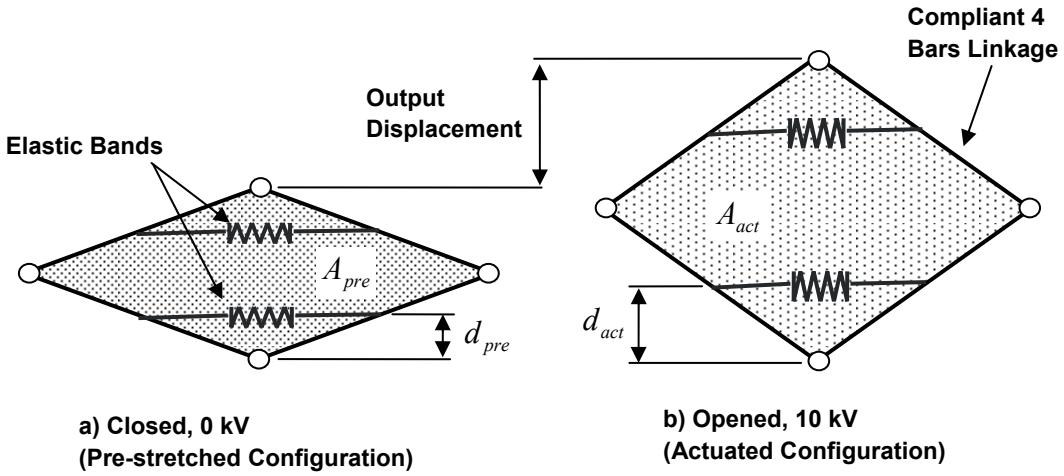

Figure 9: Diamond actuator schematic.

The diamond actuator conceptualized in this thesis has the ability to use multiple film layers to increase its force capabilities. Each film layer is assembled with a pair of thin interstitial frames, see Figure 10. These sub-assemblies are then inserted between a

pair of structural frames, see Figure 11. The interstitial and structural frames use compliant flexure joints to provide angular motion.

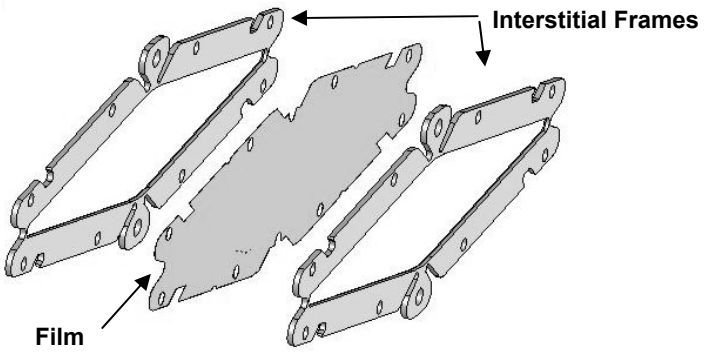

Figure 10: Film layer sub-assembly.

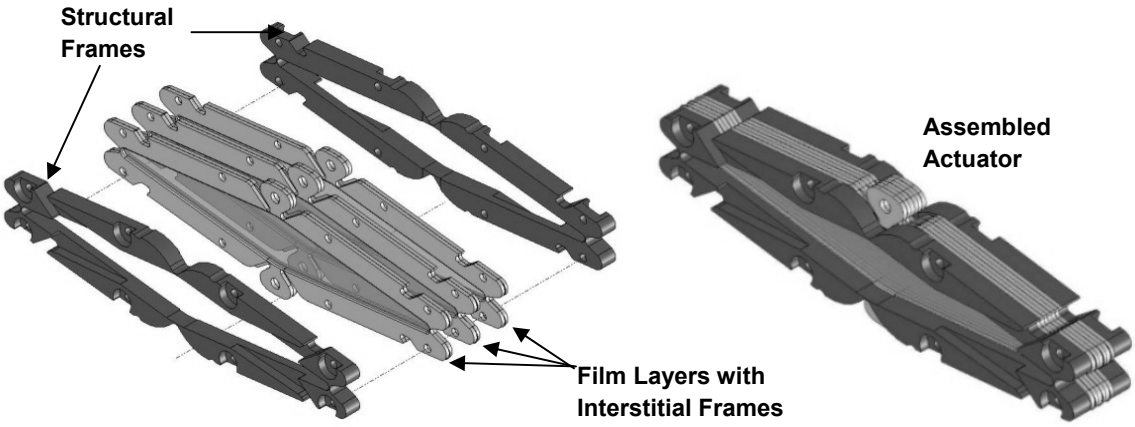

Figure 11: Multi-layer diamond actuator assembly.

Two diamond actuator sizes are considered in this thesis. Diamond actuator sizes are referred to by their diamond major axis and the sizes considered are 107 and 54 mm. A triple active layer prototype of 107 mm is shown performing 100% extensions on Figure 12. The performance characteristics of the two actuators are listed in Table 1 and

Table 2. The test velocities were scaled with size to insure identical stretch rates (see Section 5.4).

Parts manufacturing and assembly details are discussed in Appendix A. Due to hand-manufacturing limitations, the number of active layers was limited to low values of about 6 layers for the 54 mm actuator. There are no fundamental limits to the number of active layers. With proper manufacturing techniques (not yet developed), actuators with 100's to 1000's of layers are possible.

Extensive fatigue tests under various working conditions were not conducted in this thesis. However, a single preliminary fatigue test was conducted to verify if the performance of diamond actuators can be repeated. A 107 mm actuator using a single active layer was subject to a 10 kV square wave with a period of 8 s and a duty cycle of 30%. The actuator survived 15,200 cycles at 60% strain under no external load. Such high cycles suggests that the performance of diamond actuators is repeatable. Failure eventually occurred by cracks at the film/frame interface. This local failure mode is discussed in Section 5.7.

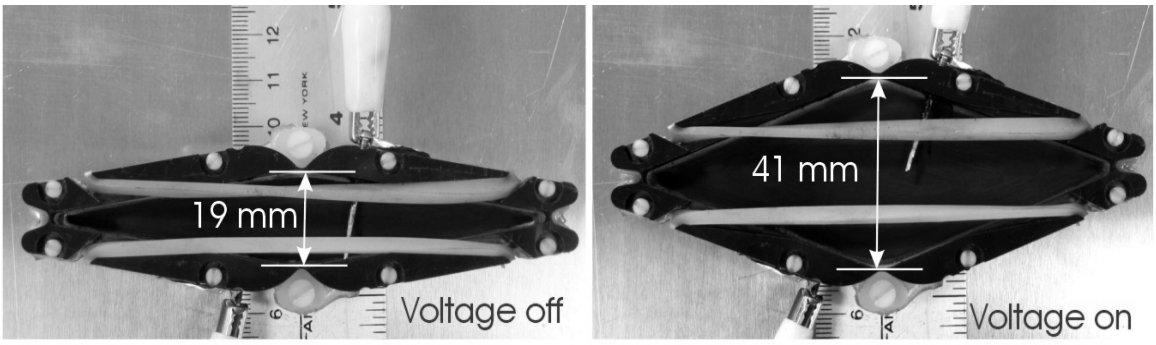

Figure 12: Diamond actuator prototype under 100% strains.

Table 1: Specifications of a 107 mm diamond actuator with 3 active layers.

Parameters		Values	Units
Assembly	Pre-stretches: $\lambda_{1,pre}$x$\lambda_{2,pre}$	5x2.2	
	Initial minor axis, y_0	18	mm
	Initial film thickness	1.5	mm
Mass	3 Films	0.43	g
	6 Interstitial frame (0.25mm)	3	g
	2 Structural frames	9	g
	2 Elastic bands	3	g
	Fasteners	1.3	g
	Total	16.7	g
Best Performance @1.6 mm/s and 10 kV	Average force	~ 2.1	N
	Stroke	27	mm
	Stretch (strain)	2.5 (150%)	
	Force-to-weight ratio	13	
	Peak efficiency	18%	
	Specific work output	0.12	J/g of film
		0.003	J/g of actuator

Table 2: Specifications of a 54 mm diamond actuator with 6 active layers.

Parameters		Values	Units
Assembly	Pre-stretches: $\lambda_{1,pre}$x$\lambda_{2,pre}$	5x2.2	
	Initial minor axis, y_0	9	mm
	Initial film thickness	1.5	mm
Mass	6 Films	0.24	g
	12 Interstitial frames (0.08mm)	2.0	g
	2 Structural frames	5.9	g
	2 Elastic bands	1.4	g
	Fasteners	1.3	g
	Total	10.9	g
Best Performance @0.8 mm/s and 10 kV	Average force	~ 1.9	N
	Stroke	12	mm
	Stretch (strain)	2.5 (150%)	
	Force-to-weight ratio	18	
	Peak efficiency	18%	
	Specific work output	0.10	J/g of film
		0.002	J/g of actuator

2.3 Continuum Mechanics: Kinematics

As pointed out in Chapter 1, DE actuators undergo large displacements. Classical Hookean mechanics is not valid and advanced continuum mechanics methods are required [30,53]. This section describes the kinematics concept used in continuum mechanics. In particular, the kinematics of diamond actuators and ideal actuators are described. These notions will be used later in Chapter 3 and 4 respectively.

A *deformation* is the time-space process of a body undergoing a change in its physical configuration over time as shown in Figure 13. The vector map $\boldsymbol{\chi}$ is called the *motion* of the body B and maps a material point defined by a vector $\mathbf{X}$ in the reference configuration to a new spatial location defined by a vector $\mathbf{x}$ in the deformed configuration. The reciprocal vector map $\boldsymbol{\chi}^{-1}$ is the *inverse motion*. The Euclidian reference frame $\mathbf{e}_1, \mathbf{e}_2, \mathbf{e}_3$ is considered inertial.

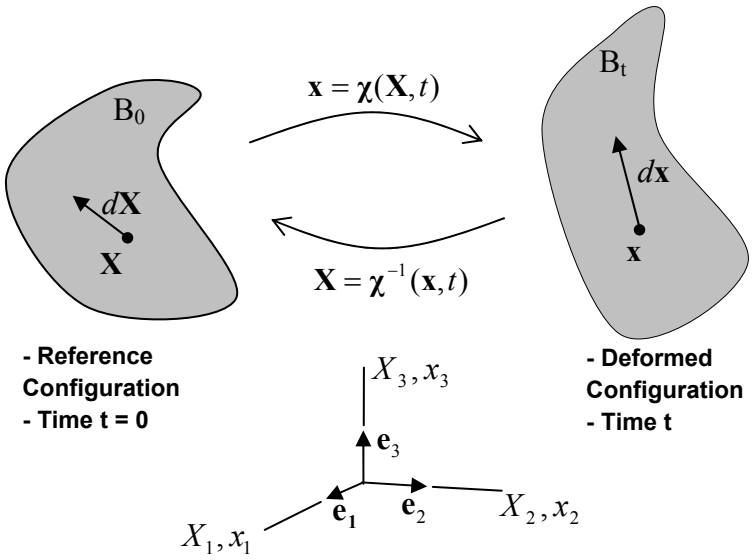

Figure 13: Illustration of a deformation, adapted from [30].

Consider a vector $d\mathbf{X}$ between two infinitesimally close points on the body in the reference configuration whose deformation lead to a corresponding infinitesimal vector,

$d\mathbf{x}$, in the deformed configuration as shown in Figure 13. These vectors can be expressed by their lengths times a unit vector: $d\mathbf{X} = dS\mathbf{e}$ and $d\mathbf{x} = ds\mathbf{e}'$. The stretch, λ, along the unit vector's direction is the ratio of the lengths between the deformed and reference configurations [30]:

$$\lambda = \frac{ds}{dS} \tag{2.1}$$

Extension and compression deformations respectively correspond to $\lambda > 1$ and $\lambda < 1$.

A fundamental concept of hyper-elasticity is the *deformation gradient* tensor, $\mathbf{F}$, defined by:

$$\mathbf{F} = \frac{\partial \boldsymbol{\chi}(\mathbf{X}, t)}{\partial \mathbf{X}} = \nabla \boldsymbol{\chi}(\mathbf{X}, t)$$

$$\mathbf{F} = \begin{bmatrix} \frac{\partial x_1}{\partial X_1} & \frac{\partial x_1}{\partial X_2} & \frac{\partial x_1}{\partial X_3} \\ \frac{\partial x_2}{\partial X_1} & \frac{\partial x_2}{\partial X_2} & \frac{\partial x_2}{\partial X_3} \\ \frac{\partial x_3}{\partial X_1} & \frac{\partial x_3}{\partial X_2} & \frac{\partial x_3}{\partial X_3} \end{bmatrix} \tag{2.2}$$

The deformation gradient tensor can be decomposed into a *pure rotation* and a *pure stretch* by the polar decomposition [30]:

$$\mathbf{F} = \mathbf{RU} = \mathbf{VR} \tag{2.3}$$

where $\mathbf{R}$ is the rotation, $\mathbf{U}$ is the right stretch tensor, and $\mathbf{V}$ is the left stretch tensor. The *principal stretches*, $\lambda_1, \lambda_2, \lambda_3$, are defined by the spectral representation of $\mathbf{U}^2$ [30]:

$$\mathbf{U}^2 = \sum_{i=1}^{3} \lambda_i^2 \mathbf{N}_i \otimes \mathbf{N}_i \tag{2.4}$$

where $\mathbf{N}_i$ are the associated eigenvectors expressed in the reference configuration. The eigenvectors define the mutually orthogonal *principal directions* of stretch along which the principal stretches are measured.

All analysis in this thesis use deformations which can readily be described in the principal directions. Such deformations are called *pure stretch* and their rotation tensor is the identity: $\mathbf{R} = \mathbf{I}$. Their deformation gradient tensors are diagonal with diagonal elements being the principal stretches:

$$\mathbf{F} = \begin{bmatrix} \lambda_1 & 0 & 0 \\ 0 & \lambda_2 & 0 \\ 0 & 0 & \lambda_3 \end{bmatrix} \tag{2.5}$$

The kinematics of incompressible materials like VHB 4905/4910 is further simplified because, to maintain a constant volume, the determinant of the deformation tensor must equal one for all deformations: $\det \mathbf{F} = J = 1$. The determinant is given by the product of the principal stretches which is equal to one for all deformations:

$$\lambda_1 \lambda_2 \lambda_3 = 1 \tag{2.6}$$

The deformation of a general DE film is decomposed into a *pre-stretch* and *actuation* deformations, see Figure 14. The film's dimensions in the reference configuration are expressed in the X_1, X_2, X_3 system. The dimensions in the pre-stretched or actuated configurations are expressed in the x_1, x_2, x_3 system. For pure stretch deformations such as considered in this thesis, the coordinate system directions X_1, X_2, X_3 and x_1, x_2, x_3 coincide with the principal directions, 1,2,3. The principal stretches of the pre-stretch, actuation and total deformations are defined by the dimensionless ratios given by:

$$\begin{aligned}
\lambda_{1,pre} &= \frac{x_{1,pre}}{X_1} \quad \lambda_{2,pre} = \frac{x_{2,pre}}{X_2} \quad \lambda_{3,pre} = \frac{x_{3,pre}}{X_3} \\
\lambda_{1,act} &= \frac{x_{1,act}}{x_{1,pre}} \quad \lambda_{2,act} = \frac{x_{2,act}}{x_{2,pre}} \quad \lambda_{3,act} = \frac{x_{3,act}}{x_{3,pre}} \\
\lambda_{1,tot} &= \frac{x_{1,act}}{X_1} \quad \lambda_{2,tot} = \frac{x_{2,act}}{X_2} \quad \lambda_{3,tot} = \frac{x_{3,act}}{X_3}
\end{aligned} \tag{2.7}$$

It can be shown using Eq. (2.7) that the principal stretches of the three deformations are linked by:

$$\lambda_{1,tot} = \lambda_{1,pre}\lambda_{1,act} \qquad \lambda_{2,tot} = \lambda_{2,pre}\lambda_{2,act} \qquad \lambda_{3,tot} = \lambda_{3,pre}\lambda_{3,act} \tag{2.8}$$

The film must be pre-stretched prior to actuation to prevent buckling under the compressive Maxwell pressure. The pre-stretch deformation is an imposed biaxial deformation that produces principal true stresses[2] in the pre-stretched configuration, $\sigma_{1,pre}, \sigma_{2,pre}, \sigma_{3,pre}$, where $\sigma_{3,pre} = 0$. For isotropic materials like VHB 4905/4910, the principal directions of stretch coincide with the principal directions of stress [30]. The

[2] In this thesis, "true" stresses or Cauchy stresses are labeled by "σ" while engineering stresses or First Piola-Kirchoff stresses are labeled by "S". The difference is the area "A" defining the stress: one is expressed in the reference configuration, $S = F/A_{reference}$, and the other is the deformed configuration, $\sigma = F/A_{deformed}$.

pre-stretched configuration is perturbed by the Maxwell pressure, P, resulting from voltage application. The film further deforms and the stresses in the actuated configuration reach a new equilibrium, $\sigma_{1,act}, \sigma_{2,act}, \sigma_{3,act}$.

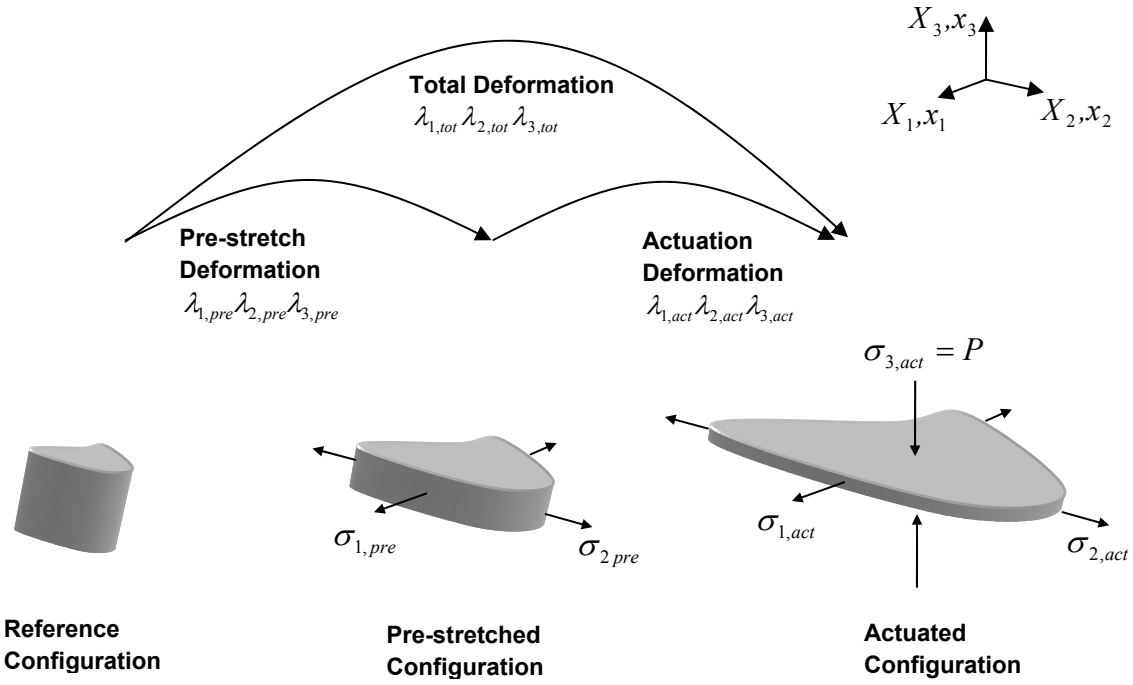

Figure 14: Deformations of a general DE film.

The kinematical descriptions of two actuators used in this thesis are given bellow.

2.3.2 Diamond Actuators

The polymer films of diamond actuators (see Section 2.2) are under biaxial extension such as shown in Figure 15. Characteristic dimensions are the diamond minor axis, y, the film thickness, u, edge length, l, and angle, θ.

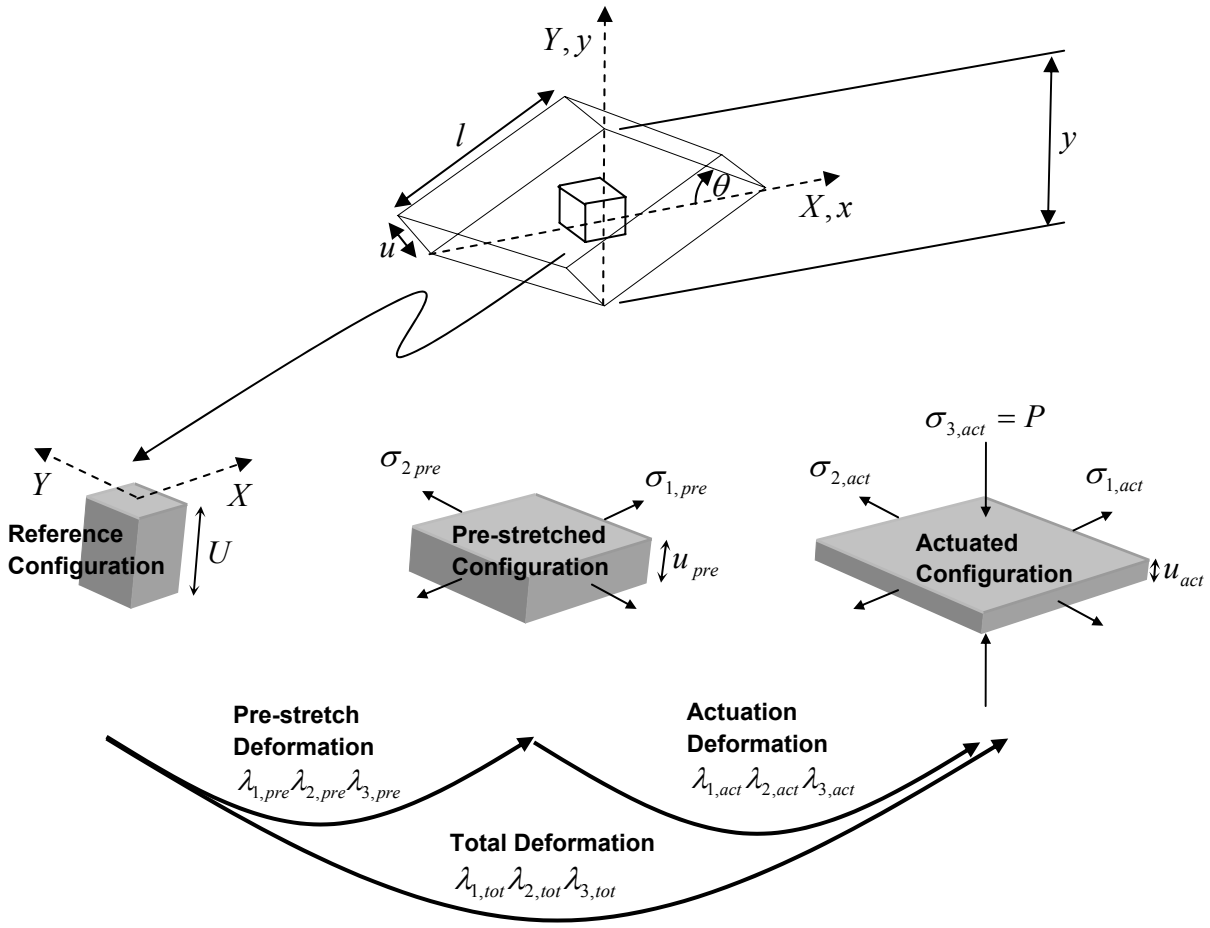

Figure 15: Deformations of a diamond actuator.

All deformations of the diamond actuator shown in Figure 15 are pure stretch and the principal directions 1,2,3 thus coincide with the X, Y, Z and x, y, z directions. The planar pre-stretches, $\lambda_{1,pre}$ and $\lambda_{2,pre}$, are independent design parameters applied to the film before assembly, see Appendix B. The incompressibility relation, $\lambda_1\lambda_2\lambda_3 = 1$, gives the corresponding thickness pre-stretch:

$$\lambda_{3,pre} = \frac{1}{\lambda_{1,pre}\lambda_{2,pre}} \tag{2.9}$$

The actuation stretches are uniform on the film's surface. Consider two points, a and b taken on the side of a diamond actuator as shown by Figure 16. The x coordinate of those two points are shown in two configurations corresponding to opening angles, θ_0 and θ. The x direction stretches between these configurations are:

$$\lambda_{x,a} = \frac{x_a}{x_{a,0}} \qquad \lambda_{x,b} = \frac{x_b}{x_{b,0}} \tag{2.10}$$

Expressing the x coordinates in terms of diamond side length l and opening angle θ gives:

$$\lambda_{x,a} = \frac{l_a \cos\theta}{l_a \cos\theta_0} = \frac{\cos\theta}{\cos\theta_0} \qquad \lambda_{x,b} = \frac{l_b \cos\theta}{l_b \cos\theta_0} = \frac{\cos\theta}{\cos\theta_0} \tag{2.11}$$

The length terms cancel making the stretches of both points equal and solely dependant on actuator opening angles θ_0 and θ. The same reasoning can be applied to the y coordinate where the a and b stretches are given by: $\lambda_{y,a} = \lambda_{y,b} = \frac{\sin\theta}{\sin\theta_0}$. The actuation stretches do not depend on the x-y positions and are thus uniform.

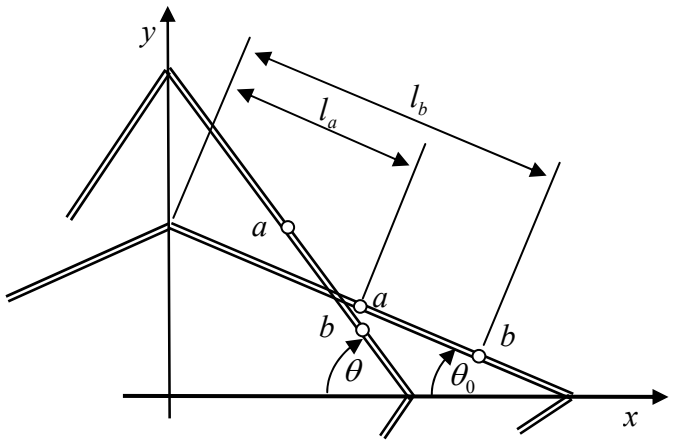

Figure 16: Actuation stretches of diamond actuators.

The actuation stretches are thus given by:

$$\lambda_{1,act} = \frac{\cos\theta}{\cos\theta_0} \qquad \lambda_{2,act} = \frac{\sin\theta}{\sin\theta_0} \qquad \lambda_{3,act} = \frac{1}{\lambda_{1,act}\lambda_{2,act}} \tag{2.12}$$

where θ_0 is the angle in the pre-stretched configuration. The total stretches are given by:

$$\lambda_{1,tot} = \lambda_{1,pre}\lambda_{1,act} \qquad \lambda_{2,tot} = \lambda_{2,pre}\lambda_{2,act} \qquad \lambda_{3,tot} = \frac{1}{\lambda_{3,tot}\lambda_{3,tot}} \tag{2.13}$$

The total stretch in the z direction conveniently gives the deformed film thickness in terms of its initial thickness, U :

$$u = U\lambda_{3,tot} \tag{2.14}$$

2.3.3 Ideal Actuators

Ideal actuators consist of a small conductive circle coated in the center of a large pre-stretched film as shown in Figure 17 (to be precise, these devices should not be called actuators as they cannot do external work). Under Maxwell pressure, the expanding circle's radius increases from its pre-stretched value, r_{pre}, to its actuated value, r_{act}.

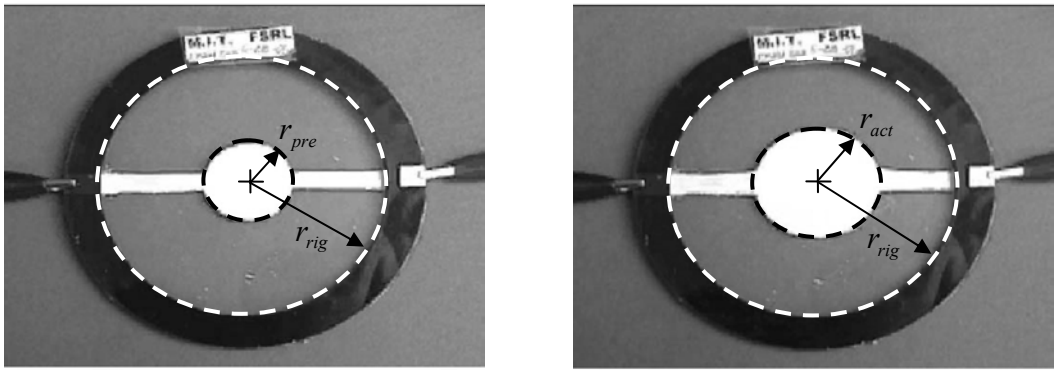

a) Pre-stretched (V= 0kV) **b) Actuated (V= 10kV)**

Figure 17: Ideal actuator.

The deformation of the active region (conductive circle) is illustrated in Figure 18. The dimensions in the reference configuration are expressed in the R,Θ,Z system. The dimensions in the pre-stretched and actuated dimensions are expressed in the r,θ,z system.

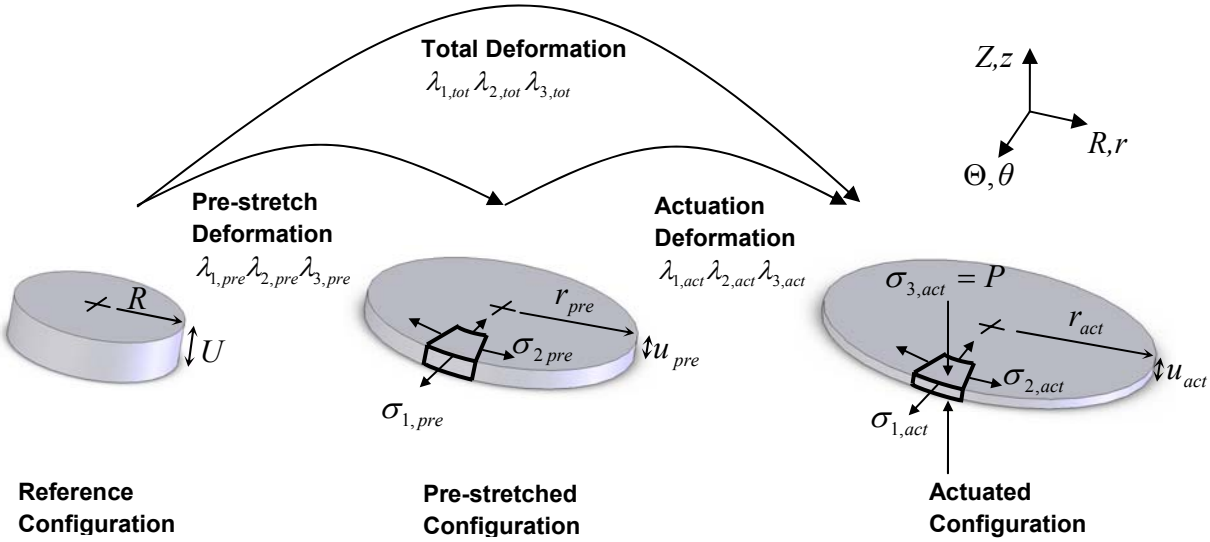

Figure 18: Deformations of the active region of an ideal actuator.

The pre-stretches are equibiaxial $\lambda_{1,pre} = \lambda_{2,pre}$ and the passive region is axisymmetric. The active region actuation deformation is thus equibiaxial: $\lambda_{1,act} = \lambda_{2,act}$. The circular active region remains circular during actuation.

The active region experiences pure stretch deformations and the R,Θ,Z and r,θ,z directions in Figure 18 coincide with the principal directions denoted by the indices 1,2,3. The planar pre-stretches, $\lambda_{1,pre}=\lambda_{2,pre}$, are design parameters applied to the film before assembly, see Appendix B. Making use of the incompressibility relationship: $\lambda_1\lambda_2\lambda_3=1$, the principal stretches of the three deformations are defined from the following dimensionless ratios (see Figure 18):

$$\lambda_{1,pre}=\lambda_{2,pre}=\frac{r_{pre}}{R} \qquad \lambda_{3,pre}=\frac{1}{\lambda_{1,pre}^2} \tag{2.15}$$

$$\lambda_{1,act}=\lambda_{2,act}=\frac{r_{act}}{r_{pre}} \qquad \lambda_{3,act}=\frac{1}{\lambda_{1,act}^2} \tag{2.16}$$

$$\lambda_{1,tot}=\lambda_{2,tot}=\lambda_{1,pre}\lambda_{1,act} \qquad \lambda_{3,tot}=\frac{1}{\lambda_{1,tot}^2} \tag{2.17}$$

Under these conditions, each deformation reduces to a single unknown geometric dimension given here by the expanding dot radius.

2.4 Continuum Mechanics: Stresses

This section describes the constitutive stress concept used in continuum mechanics to handle materials with non-linear material properties [30,53]. In particular, the Bergstrom-Boyce and Ogden constitutive stresses models are described. These notions will be used later in Chapter 3 and 4 respectively.

The principal stresses in the film are computed from the principal stretches by constitutive models of the form $\sigma_i=f(\lambda_i) \qquad i=1,2,3$, or $\sigma_i=f(\lambda_i,t) \qquad i=1,2,3$ if viscoelastic (i.e. see references [2,6,7,20,30,53]). The principal stretches used in these

models must refer to the (stress-free) reference configuration. Accordingly, the stresses $\sigma_{1,pre}, \sigma_{2,pre}, \sigma_{3,pre}$ are computed from $\lambda_{1,pre}, \lambda_{2,pre}, \lambda_{3,pre}$ and the stresses $\sigma_{1,act}, \sigma_{2,act}, \sigma_{3,act}$ are computed from $\lambda_{1,tot}, \lambda_{2,tot}, \lambda_{3,tot}$. The two different constitutive models used in this thesis are described bellow.

2.4.1 Ogden Model

Ogden's stress model is defined in term of the material's Helmoltz free-energy[3] (in terms of principal stretches) is [30]:

$$\psi = \tilde{\psi}(\lambda_1, \lambda_2, \lambda_3) = \sum_{a=1}^{N} \frac{\mu_a}{\alpha_a} \left[(\lambda_1)^{\alpha_a} + (\lambda_2)^{\alpha_a} + (\lambda_3)^{\alpha_a} - 3 \right] \tag{2.18}$$

where N is the model's order, μ_a and α_a are material parameters curve-fitted over experimental stress/stretch data. Appendix C shows how three parameters sets were obtained from uniaxial tests performed at three different stretch rates, $\dot{\lambda}_{UNI}$. These material parameters have no physical meaning and can theoretically take any value necessary to match experimental data. Ogden's form has shown good performance in modeling elastomer materials used in DE actuators [32,85].

The derivative of the Helmoltz free energy function of Eq. (2.18) with respect to the deformation gradient tensor leads to the First Piola-Kirchoff or engineering stresses. For a second order model, $N = 2$, these stresses are given by [30]:

$$S_i = -\left(\frac{p}{\lambda_i} \right) + \mu_1 (\lambda_i)^{(\alpha_1 - 1)} + \mu_2 (\lambda_i)^{(\alpha_2 - 1)} \qquad i = 1,2,3 \tag{2.19}$$

[3] For hyper-elastic materials, the Helmoltz free-energy only depends on the deformation of the material and is therefore sometimes referred to the strain-energy function.

where p is a Lagrange multiplier defined by the boundary conditions. Physically, p can be viewed as a hydrostatic pressure.

The Piola transformation between the engineering stress (reference configuration) and true stress (deformed configuration) tensors is used to obtain the true stresses [30]:

$$\boldsymbol{\sigma} = J^{-1}\mathbf{S}\mathbf{F}^{T} \tag{2.20}$$

where $\boldsymbol{\sigma}$ is the true stress tensor and $\mathbf{S}$ is the engineering stress tensor. For incompressible materials ($J = 1$), Eq. (2.20) written in components reduces to:

$$\sigma_i = S_i \lambda_i \qquad i = 1,2,3 \tag{2.21}$$

Applying the transformation of Eq. (2.21) to the engineering stress expression of Eq. (2.19) yields:

$$\sigma_i = -p + \mu_1 (\lambda_i)^{\alpha_1} + \mu_2 (\lambda_i)^{\alpha_2} \qquad i = 1,2,3 \tag{2.22}$$

2.4.2 Bergstom-Boyce Model

The Bergstrom-Boyce (BB) model is described here in the context of modeling diamond actuators. Minor changes were made to improve its prediction capability for VHB 4905/4910. The reader is referred to the paper by Bergstrom and Boyce for further information [6].

The Bergstrom-Boyce approach is based on the generally accepted idea that elastomers act as if they were made from two superposed solids: one purely elastic and one viscous. This idea is graphically represented on Figure 19. Solid A is a purely

elastic network of polymer chains while solid B is a plastic or viscous network connected in series with a second elastic network.

The resulting true stress on the material is the sum of the stresses acting on each network:

$$\boldsymbol{\sigma} = \boldsymbol{\sigma}_{\mathbf{A}} + \boldsymbol{\sigma}_{\mathbf{B}} \tag{2.23}$$

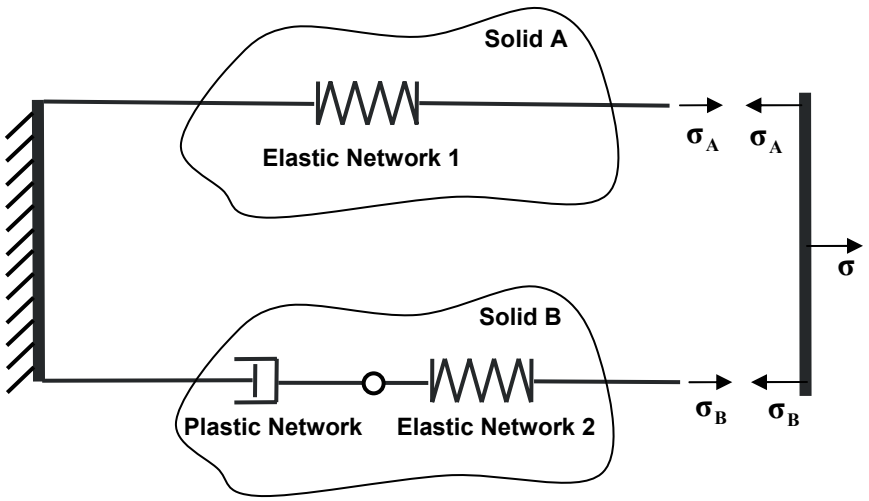

Figure 19: Bergstrom-Boyce rheological model.

Diamond actuator deformations are pure stretch (no rotations). The film deformation gradient $\mathbf{F}$ is thus given directly by the principal stretches of Eq. (2.13):

$$\mathbf{F} = \begin{bmatrix} \lambda_{1,tot} & 0 & 0 \\ 0 & \lambda_{2,tot} & 0 \\ 0 & 0 & \lambda_{3,tot} \end{bmatrix} \tag{2.24}$$

The deformation gradient is the same for networks A and B:

$$\mathbf{F} = \mathbf{F}_{\mathbf{A}} = \mathbf{F}_{\mathbf{B}} \tag{2.25}$$

The deformation gradient of network B is further decomposed into a plastic and elastic part by the Kroner-Lee decomposition, see Figure 20:

$$\mathbf{F} = \mathbf{F}_B^e \mathbf{F}_B^p \tag{2.26}$$

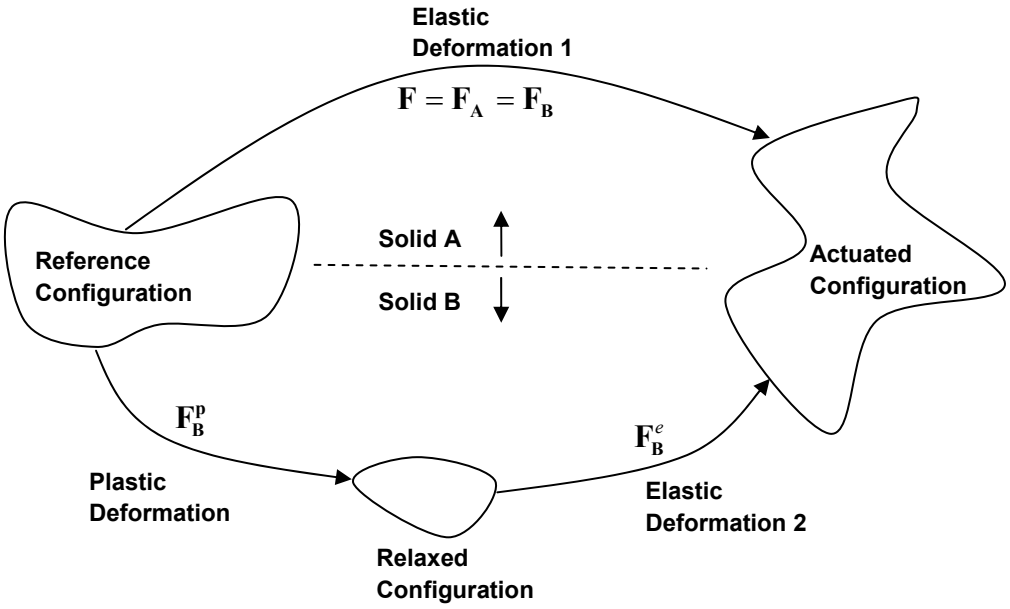

Figure 20: Bergstrom-Boyce kinematics, adapted from [6].

This plastic-elastic decomposition implies that network B reaches the final configuration in two steps: (1) it deforms plastically from the reference configuration to a relaxed configuration and (2) it deforms elastically from the relaxed configuration to the actuated configuration.

Network Stresses

The first change to the BB model is to swap the two elastic models from 8-chains models to Ogden models. For VHB 4905/4910, the Ogden models gave significantly better accuracy, especially for network B. Network A uses a first order Ogden model:

$$\sigma_{A,i} = -p + \mu_1 \left(\lambda_{A,i}\right)^{\alpha_1} \qquad i = 1,2,3 \tag{2.27}$$

and network B uses a second order Ogden model:

$$\sigma_{B,i} = -p + \mu_1 \left(\lambda_{B,i}^{e}\right)^{\alpha_1} + \mu_2 \left(\lambda_{B,i}^{e}\right)^{\alpha_2} \qquad i = 1,2,3 \tag{2.28}$$

Flow

The plastic deformation part of network B controls viscous hardening dynamics. The viscous flow rule is given by:

$$\dot{\mathbf{F}}_{\mathbf{B}}^{\mathbf{p}} = \mathbf{F}_{\mathbf{B}}^{\mathbf{e}^{-1}} \left(\dot{\gamma}_B \, \mathbf{N}_{\mathbf{B}}\right) \mathbf{F}_{\mathbf{B}}^{\mathbf{e}} \mathbf{F}_{\mathbf{B}}^{\mathbf{p}} \tag{2.29}$$

where $\dot{\gamma}_B$ is the flow rate and $\mathbf{N}_{\mathbf{B}}$ is the direction. The flow rate is given by:

$$\dot{\gamma}_B = \hat{C}_1 \left(\bar{\lambda}_B^p - 1\right)^{-C_2} \left(\tau_B\right)^m e^{-C_3 \bar{\lambda}_B^p} \tag{2.30}$$

where $\hat{C}_1, C_2, C_3, m$ are material parameters. The flow rate is affected by the stretches and the stresses acting on network B. The stretch affected terms $\left(\bar{\lambda}_B^p - 1\right)^{-C_2}$ and $e^{-C_3 \bar{\lambda}_B^p}$ of Eq. (2.30) represent the flow decreasing effect of high stretches. The exponential term, $e^{-C_3 \bar{\lambda}_B^p}$, was added to the original model to give more sensitivity to flow blockage at high stretches. These terms are based on the effective stretch given by:

$$\bar{\lambda}_B^p = \sqrt{\frac{\left(\lambda_{B,1}^p\right)^2 + \left(\lambda_{B,2}^p\right)^2 + \left(\lambda_{B,3}^p\right)^2}{3}} \tag{2.31}$$

The stress affected term $(\tau_B)^m$ of Eq. (2.30) represents the flow increasing effect of high shear stresses. The equivalent shear stress, τ_B, is defined by:

$$\tau_B = \sqrt{\tfrac{1}{2} tr[\boldsymbol{\sigma}^*_{B0}\boldsymbol{\sigma}^*_{B0}]} \tag{2.32}$$

The equivalent shear stress is calculated from the deviatoric (or traceless) part of the Cauchy stress tensor acting on network B:

$$\boldsymbol{\sigma}^*_{\mathbf{B0}} = \boldsymbol{\sigma}^*_{\mathbf{B}} - \tfrac{1}{3} tr[\boldsymbol{\sigma}^*_{\mathbf{B}}]\mathbf{I} \tag{2.33}$$

The Cauchy stress, $\boldsymbol{\sigma}^*_{\mathbf{B}}$, used in Eq. (2.33) is the true stress in the relaxed configuration where the flow occurs. This stress is found by pulling back the actuated configuration stress in the relaxed configuration:

$$\boldsymbol{\sigma}^*_{\mathbf{B}} = \mathbf{F}^{\mathbf{e}\,-1}_{\mathbf{B}}\boldsymbol{\sigma}_{\mathbf{B}}\mathbf{F}^{\mathbf{e}\,-\mathbf{T}}_{\mathbf{B}} \tag{2.34}$$

The flow direction coincides with the driving stress direction:

$$\mathbf{N}_{\mathbf{B}} = \frac{1}{\sqrt{2}\tau_B}\boldsymbol{\sigma}^*_{B0} \tag{2.35}$$

Equations (2.23) to (2.35) are assembled together to compute the stresses in the polymer film. The calculations are started assuming the actuator has been at rest for a long time in the pre-stretched configuration without viscous stresses. The stress-free initial conditions on network B are:

$$\mathbf{F_B^p} = \begin{bmatrix} \lambda_{1,pre} & 0 & 0 \\ 0 & \lambda_{2,pre} & 0 \\ 0 & 0 & \lambda_{3,pre} \end{bmatrix}$$
$$\mathbf{F_B^e} = \begin{bmatrix} 1 & 0 & 0 \\ 0 & 1 & 0 \\ 0 & 0 & 1 \end{bmatrix} \tag{2.36}$$

The various parameters used in the Bergstrom-Boyce model are determined in Appendix D.

CHAPTER

3

CHARACTERIZATION AND MODELING OF FUNDAMENTAL MECHANISMS OF DIELECTRIC ELASTOMER ACTUATORS

3.1 Introduction

The objectives of this chapter are to identify the key physical phenomena that influence DE actuators performance and to develop analytical models to describe their performance. The performance of a typical DE design is first characterized experimentally over a large range of working conditions. Governing mechanisms are then postulated and analytical models are derived. Finally, model predictions are compared to experimental data.

3.2 Experimental Characterization

3.2.1 Experimental Setup

This chapter focuses on the 107 mm diamond actuator concept presented in Chapter 2. Figure 21 shows the test system that consists of a single pre-stretched polymer film bonded to a pair of interstitial frames before being sandwiched between a pair of structural frames.

Actuator performance is evaluated on a complete actuation cycle. Conservative elements like the preloading elastic bands which have negligible viscous losses give no

net work over closed cycles. Hence, the elastic bands were not used in this performance study to reduce all possible error sources.

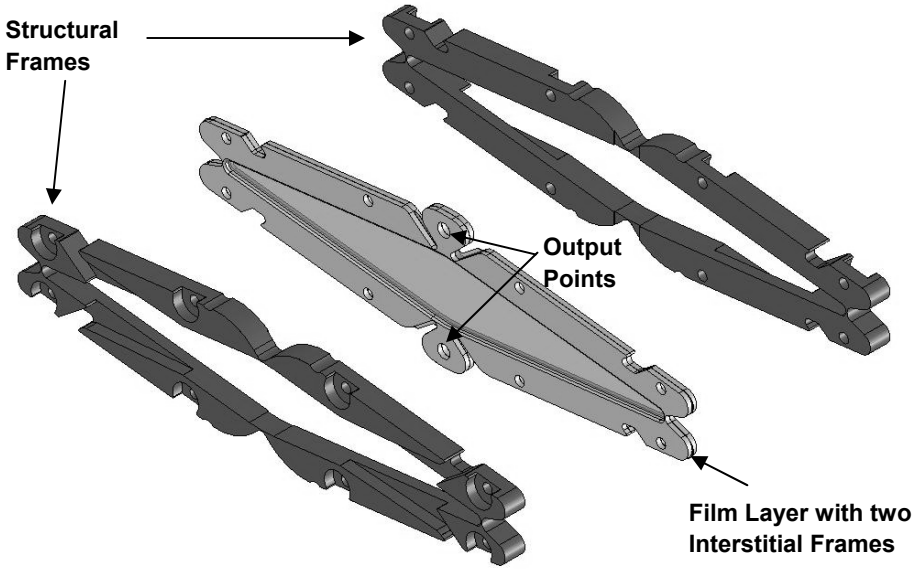

Figure 21: Single active layer diamond actuator used for work cycle experiments.

The actuator described above is tested using an actuator dynamometer system developed in this study and its performance is measured under various working conditions, see Figure 22 and Figure 23. The system consists of a moving ram that operates under controlled position and velocity, y and $\dot{y}$, where y is the diamond shape's minor axis. Force, F, is measured with a 5 lbf strain gauge load cell (Omega LCEB-5). Voltage, V, is read from the HV power supply (Matsusada AMS-10P/N2) and current, i, is measured by reading the voltage drop across a resistor in a custom circuit.

The actuator dynamometer was used under standardized test procedures called w*ork cycles*. A work cycle imposes three working conditions, V, y, and $\dot{y}$, and measures two actuator outputs, F and i.

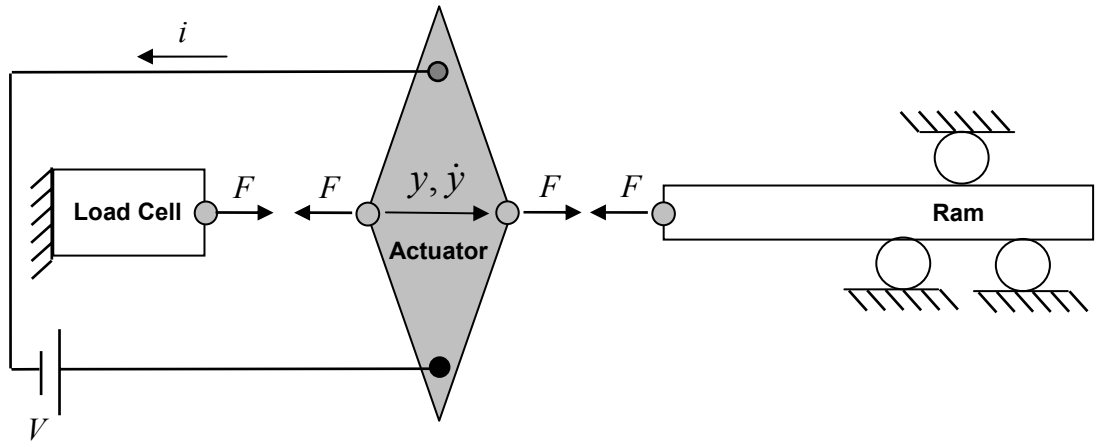

Figure 22: Schematic of actuator dynamometer setup

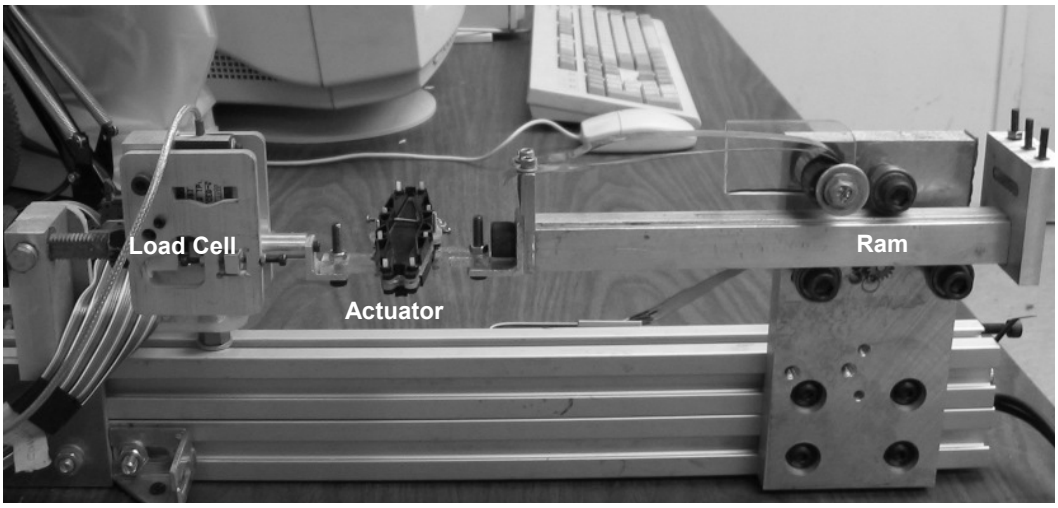

Figure 23: Photograph of actuator dynamometer setup.

Typical voltage and position/velocity commands are shown in Figure 24. The actuator starts in the closed position in an equilibrium state. The moving ram then extends the actuator at a constant velocity while a constant voltage is applied to the actuator as a step function. When the actuator reaches its maximum length, $y_{\max}$, the voltage is removed and the moving ram switches direction to close the actuator at the same constant velocity.

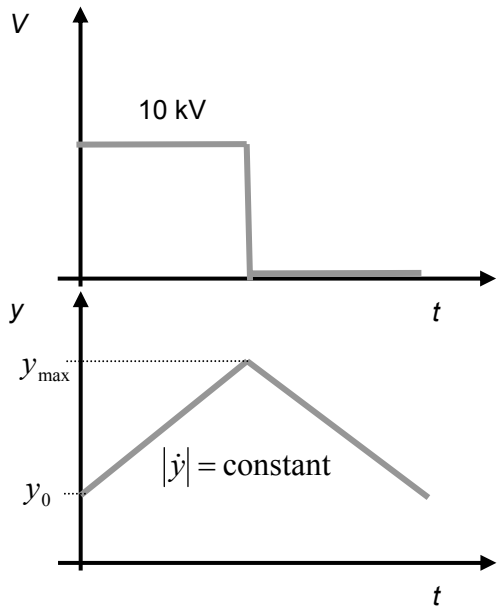

Figure 24: Typical input commands for work cycle experiments.

Typical current and force output measurements are shown in Figure 25 and Figure 26 for $\dot{y} = 1.3\,\text{mm/s}$. All work cycle results are presented in terms of actuator stroke defined by: $s = y - y_0$. The capacitor charging and discharging involves large currents over short time scales compared to overall experiment and were not considered. The data corresponding to these peaks was thus trimmed from Figure 25. The force output of Figure 26 shows a drop when voltage is initially applied and a force increase when voltage is removed. These steps are visible because voltage was switched manually and the exact switching time does not coincide perfectly with motion. The force difference between the opening and closing forces, ΔF, is the usable force to do work on an outside system.

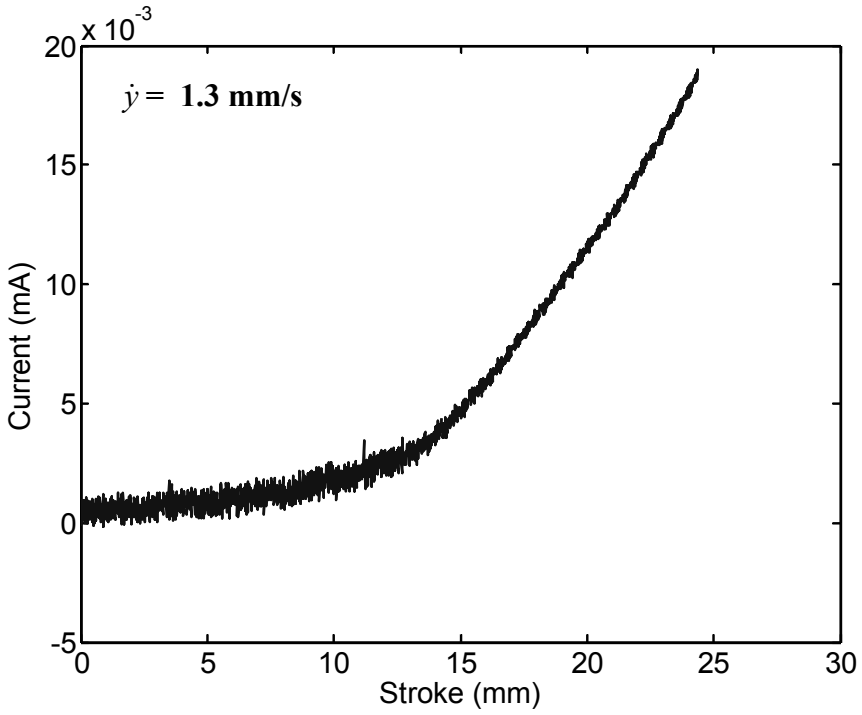

Figure 25: Typical current of a work cycle experiment.

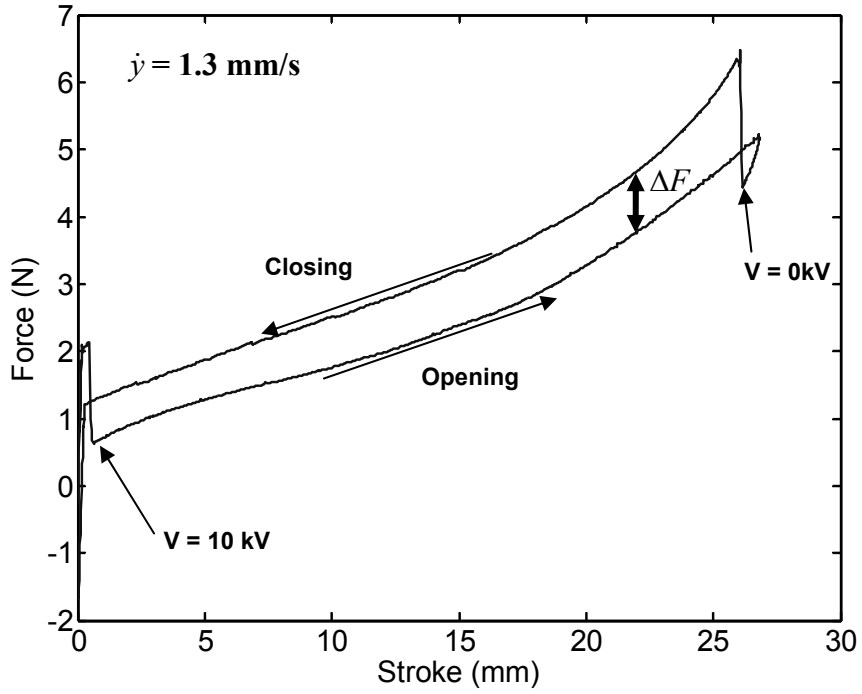

Figure 26: Typical force of a work cycle experiment.

These experimental data are used to evaluate a set of five basic performance metrics defined by:

1. Force difference: ΔF (see Figure 26),
2. Power, defined by :

$$\dot{W}_O = \Delta F \dot{y} \tag{3.1}$$

3. Current consumption: i
4. Cycle work output, defined by:

$$W_O = \int_0^{s_{\max}} \Delta F(s) ds \tag{3.2}$$

5. Cycle efficiency, defined by:

$$\eta = \frac{W_O}{W_I} = \frac{\int_0^{s_{\max}} \Delta F(s) ds}{\frac{V}{\dot{y}} \int_0^{s_{\max}} i(s) ds + \int_0^{s_{\max}} \left(\Delta F_e(s) - \Delta F(s) \right) ds} \tag{3.3}$$

where the upper integral limit $s_{\max}$ in Eqs. (3.2) and (3.3) is the maximum cycle stroke. The second term of the denominator in Eq. (3.3) is the input energy from the dynamometer going to the film's viscous dissipation. The dissipation force, $\Delta F_e(s) - \Delta F(s)$, is difference from the equilibrium case, $\Delta F_e(s)$, where velocities are low enough to neglect viscous forces.

To keep the number of experiments tractable, measurements were only performed at the maximum stroke allowed by the diamond actuator. The data vectors were then truncated to generate new data vectors for lower strokes. An example of the procedure is

given on Figure 27 where data obtained at s_{max}=27 mm is deprived of its right part to form a new data set for the particular case of s_{max}=15 mm. The procedure is repeated at intervals of 1mm within the bracket: $s_{max} \in [1,27]$.

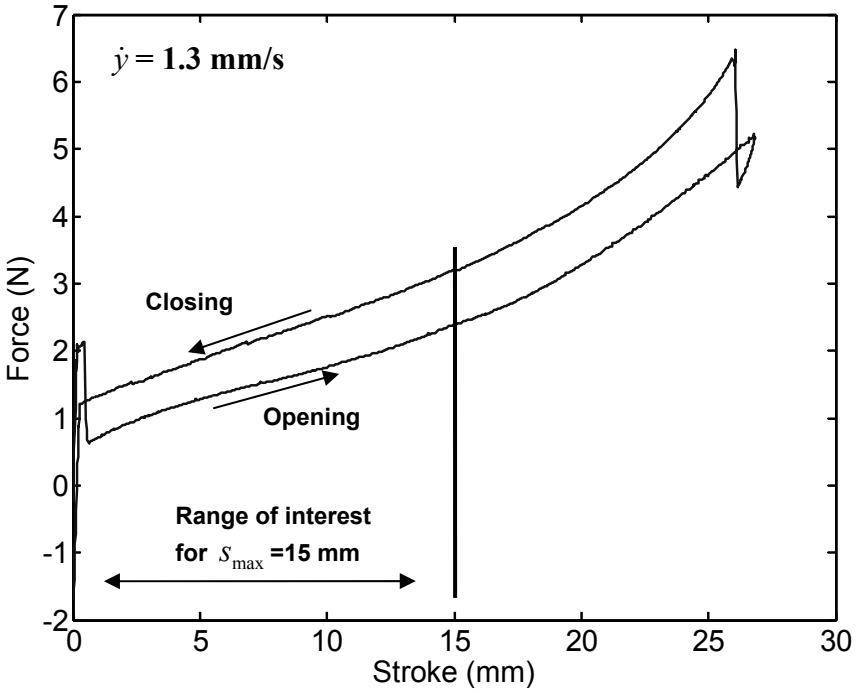

Figure 27: Example of data vector truncation.

3.2.2 Experimental Results

The five performance metrics described in the preceding section are mapped as a function of actuator velocity and cycle stroke such that: $Metric = f(\dot{y}, s)$. For all experiments, initial position is y_0=18 mm and actuator voltage is V=10 kV.

Experimental results are presented in Figure 28 to Figure 35 and discussed in the following paragraphs. The maps show a reduced maximum cycle stroke of s_{max}=21 mm to recuperate data from low stretch rate tests that failed at lower strokes. The results apply to actuators similar to the diamond actuator. It is expected (but has not been verified) that the results describe general trends of DE actuators.

Force Difference (Figure 28):

The force difference does not appear to vary significantly with stroke. This suggests that, for diamond actuators, the increase in Maxwell pressure resulting from the film thickness reduction during actuation is approximately counteracted by actuator geometrical effects.

The force difference decreases drastically as velocity increases. This behavior is typical of highly viscoelastic materials. The force difference even becomes negative for velocities higher than 6 mm/s. At this point, actuators become energy sinks instead of sources due to high viscoelastic losses.

Actuator forces are highest when velocity is zero (like DC motors and voice coils). Here, a velocity of 1.6 mm/s is arbitrarily taken as a typical operating velocity, and at this velocity, the force difference is approximately 0.75 N. The active layer mass is 0.14g and the force-to-weight ratio on a film basis is an impressive 500:1.

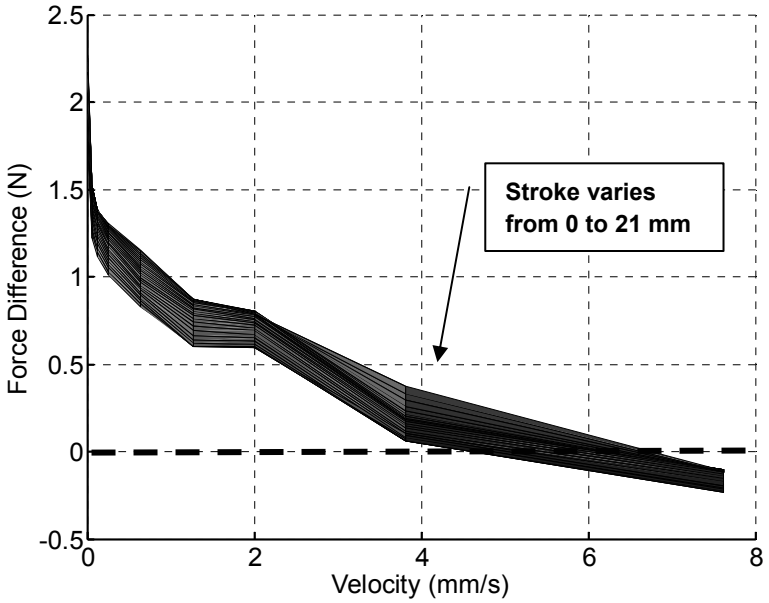

Figure 28: Force difference map.

Power (Figure 29):

Power is function of force difference, see Eq. (3.1). Hence the power map, like the force difference one, does not vary significantly with stroke. The decreasing force with velocity leads to a power peak located around 2 to 3 mm/s, and its value is approximately 1.5 mW. The corresponding specific power per unit film mass is 0.01 W/g.

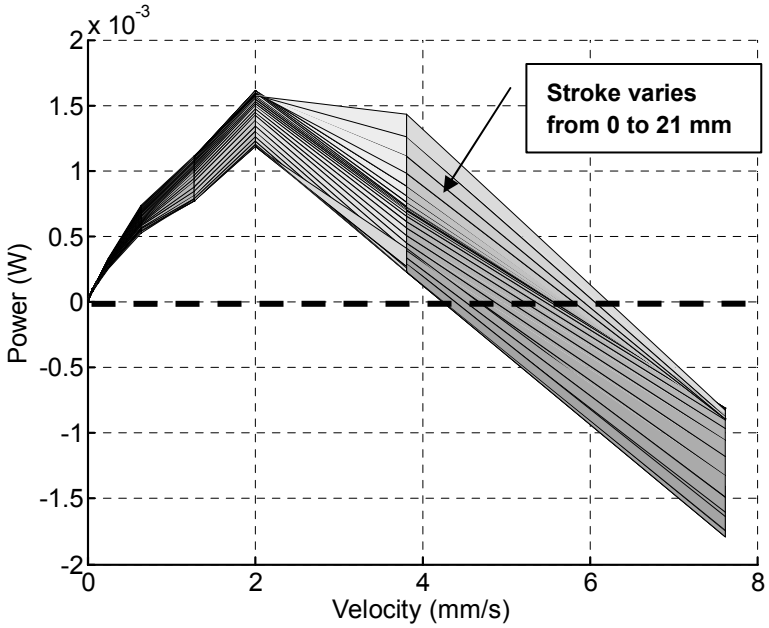

Figure 29: Power map.

Current Consumption (Figure 30 and Figure 31):

High current consumption was observed at large strokes and low velocities, respectively identified by arrows A and B in Figure 31. These local high currents do not correspond proportionally into higher force differences. Hence, these large currents are wasted energy.

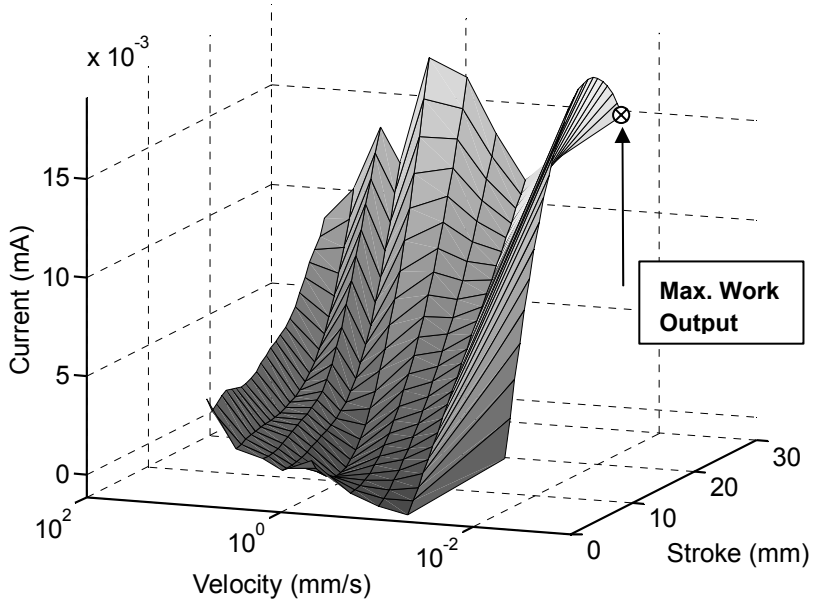

Figure 30: Current consumption map.

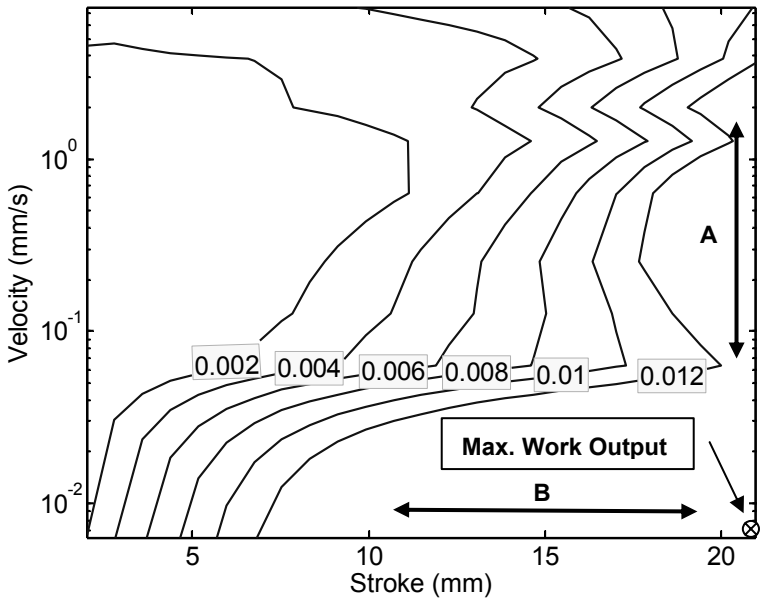

Figure 31: Current consumption map, isolevel view, units in milliampere.

Cycle Work Output (Figure 32 and Figure 33):

The figures show that maximum work output is obtained at low velocity and high stroke. However, such conditions are not used in practice because they are unreliable due to pull-in failure under external load (see the failure mode study of Chapter 4 and the design domain maps in Section 5.3).

At an arbitrary operating velocity of 1.6 mm/s, the work output at s_{max} =27 mm is about 0.14 J. With a film mass of 0.14g, the specific work output per unit film mass is 0.1 J/g; more than an order of magnitude lower than the film elastic energy at failure of 3-4 J/g reported by SRI International [55]. In practice, actuators cannot be actuated from zero-stretch until failure. They must start from a minimal pre-stretched level and stop before their fail. Hence practical work output per unit film mass such as measured here (0.1 J/g) are much lower.

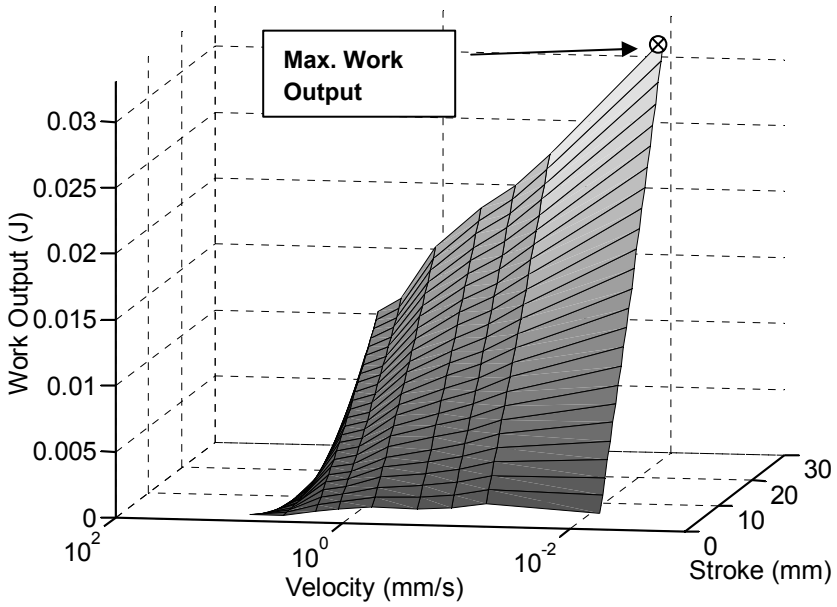

Figure 32: Cycle work output map.

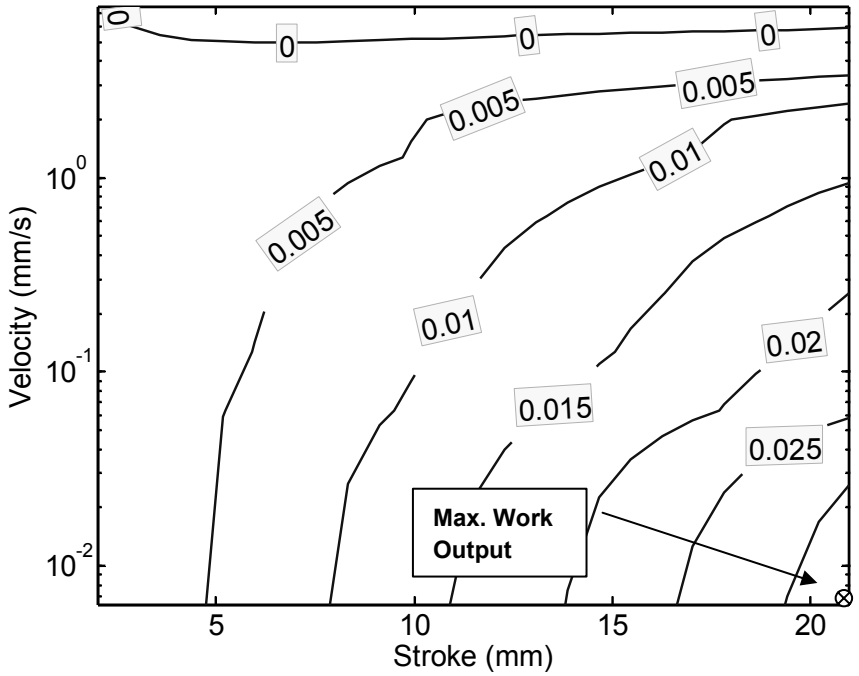

Figure 33: Cycle work output map, isolevel view, units in Joule.

Cycle Efficiency (Figure 34 and Figure 35):

The efficiency map in Figure 34 shows an optimum region obtained at the lowest extension possible and at velocities of about 1mm/s. The peak efficiency is about 12% at a stroke of about 1mm. Such low efficiencies show how practical systems differ from the ideal values of 80% reported by SRI International [37,55]. Such high efficiencies are reported when operating at 80 Hz, where output strains are small, typically less than 1%. Actuator behavior at such small strains is of limited practical use and is not considered here.

Based on the force and current maps of Figure 28 and Figure 30, the efficiency map seems to be shaped by low force at high velocities and by large current consumption at low velocity and high extensions. These effects are hypothetically caused respectively by viscoelasticity and current leakage. Analytical models developed in the next two sections support this hypothesis.

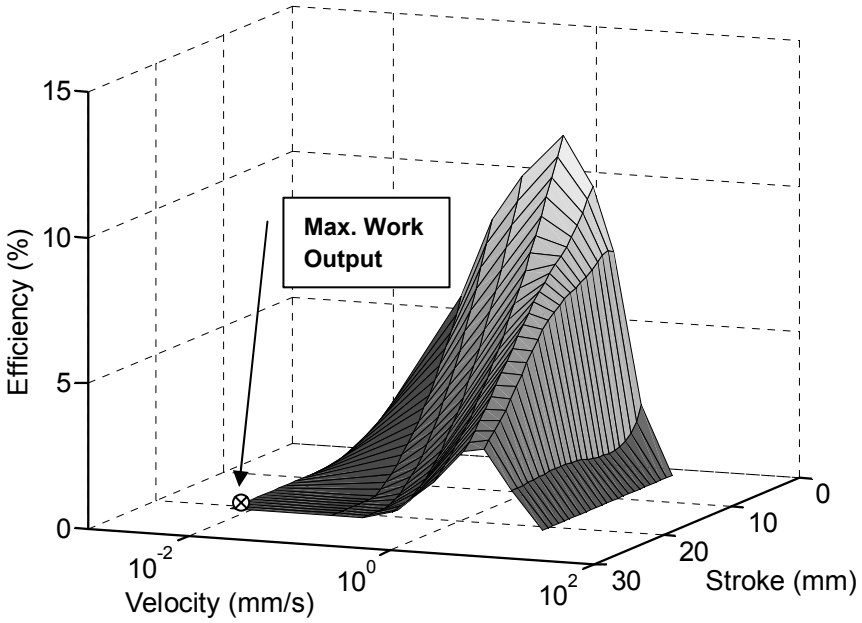

Figure 34: Cycle efficiency map.

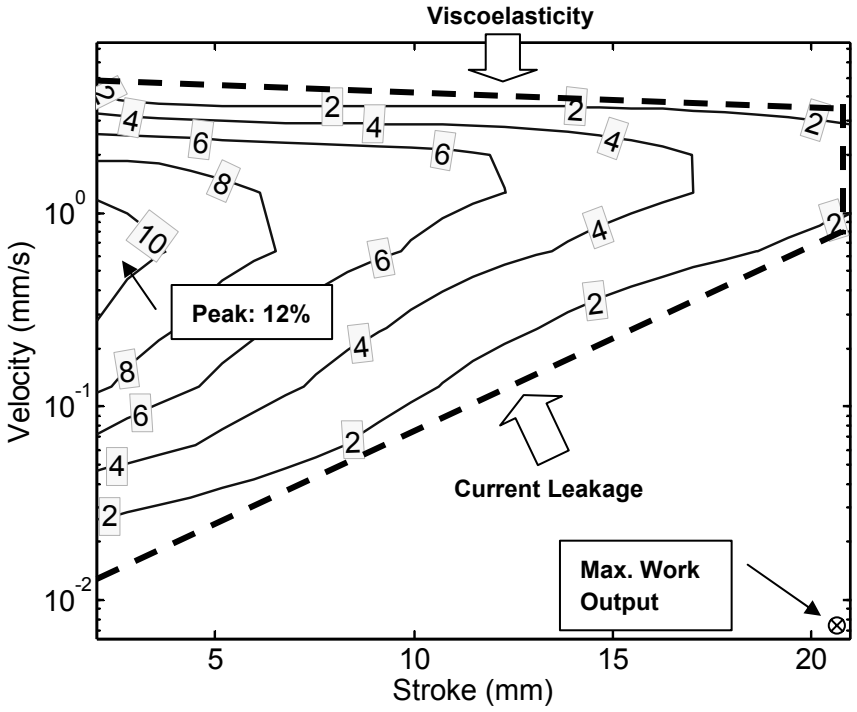

Figure 35: Cycle efficiency map, isolevel view, units in percentage.

3.3 Viscoelasticity Model

A diamond actuator model integrating possible viscous effects is developed. The objective of this model is to replicate the force/stroke curves of the work cycle experiments (see Figure 26 on page 55).

3.3.1 Analytical Development

The modeled system is the 107 mm diamond actuator used in the work cycle experiments (see Figure 21 on page 52). The system is split into four sub-models, where the total actuator force is the sum of the sub-model forces, see Figure 36:

$$F = F_S + F_I + F_F + F_M \tag{3.4}$$

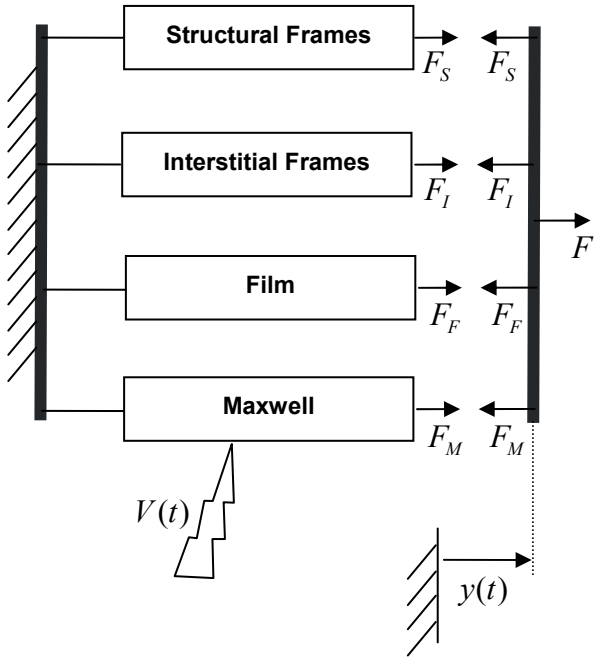

Figure 36: Viscoelastic model structure.

The Maxwell pressure is modeled separately from the film. This approach is mathematically correct because the film is an incompressible solid under uniform stresses. In such cases, the Maxwell pressure acts hydrostatically and does not contributes directly to the film's deformation energy. The film deformation energy is solely affected by actuator motion and thus the Maxwell pressure can be considered independently.

The four sub-models were implemented numerically in Matlab's Simulink® environment to predict the force response under prescribed position and voltage commands, $y(t)$ and $V(t)$. The models leading to the force components F_S, F_I, F_F, F_M are detailed in the following paragraphs and validated against experimental data in the next section.

Structural and Interstitial Frames Forces, F_S and F_I :

The structural frames are made from acetal (Delrin), a highly elastic engineering plastic with low viscous effects. Hence the structural frames are considered as purely elastic and their force/stroke response is obtained by fitting a fourth order spring over experimental data. The spring function is given below for two frames (units are Newtons and millimeters):

$$F_S = 2.399\text{x}10^{-5} y^3 - 0.001754 y^2 + 0.05111 y - 0.6022 \tag{3.5}$$

The interstitial frames are made from Nylon 6/6 which, unlike acetal, presents significant viscous effects. The interstitial frames are modeled by the simple rheological model of Figure 37. The total force is the sum of the branch forces:

$$F_I = F_1 + F_2 \tag{3.6}$$

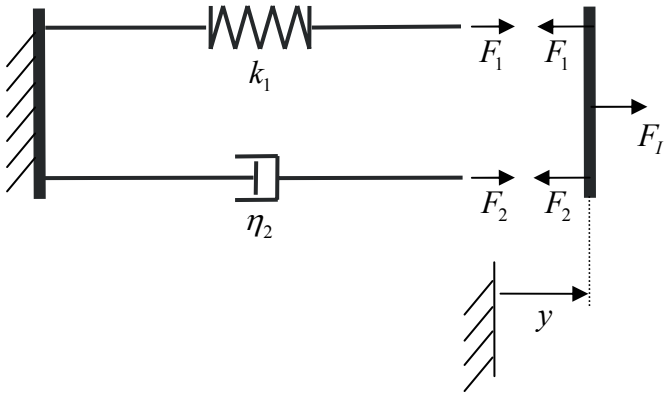

Figure 37: Interstitial frame rheological model.

Branch one is a fourth order spring fitted over average force/position of a complete work cycle. The spring function is given below for two frames (units are Newtons and millimeters):

$$F_1 = 3.470\text{x}10^{-5} y^3 - 0.002647 y^2 + 0.08373 y - 0.7953 \tag{3.7}$$

Branch two is a nonlinear damper. The damping function is shaped to give higher viscous forces at low stretch rates than a conventional linear damper. The damping function is given below for two frames (units are Newtons and millimeters per second):

$$F_2 = 0.11\left(1 + 35e^{-\left|\frac{\dot{y}}{0.09}\right|}\right)\dot{y} \tag{3.8}$$

The experimental data used to calibrate the structural and interstitial frames sub-models were obtained from a work cycle experiment conducted without a film. As shown by Figure 38 the combined structural and interstitial frames models show excellent agreement with experimental data. The data was acquired with an initial diamond minor axis length of y_0=10 mm.

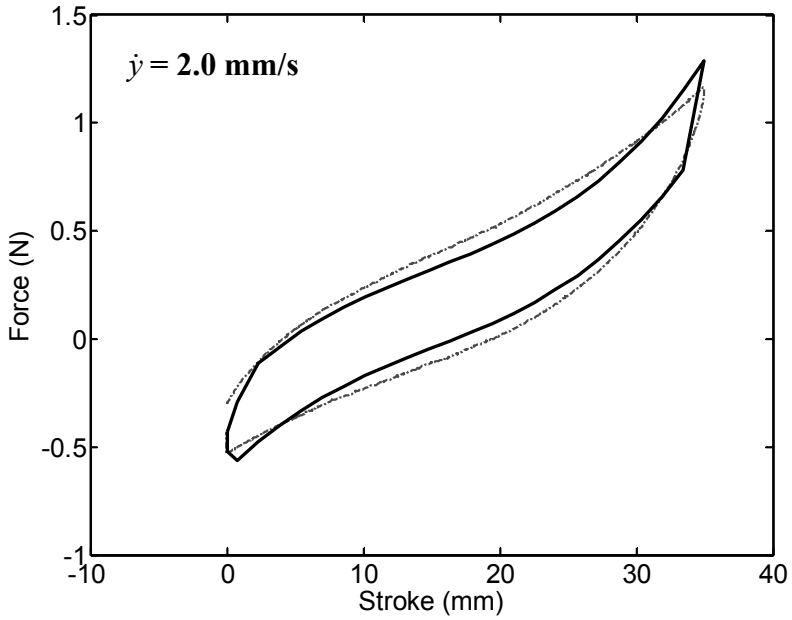

Figure 38: Structural and interstitial frames model, prediction (dark) vs. experiment (light).

Film Force, F_F:

The relation between the film's planar stresses and the film force, F_F, is found from the free body diagram of a quarter of a diamond actuator frame shown in Figure 39.

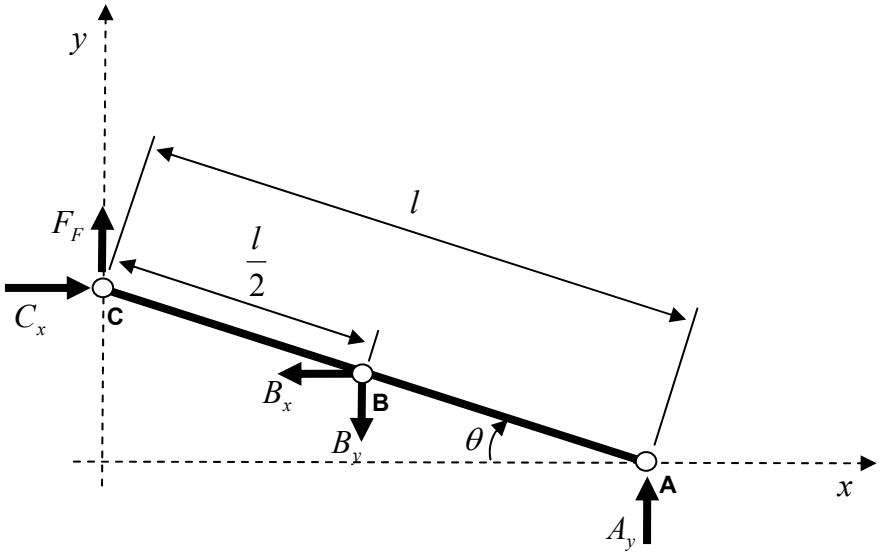

Figure 39: Free body diagram of diamond actuator frame.

In Figure 39, the planar stresses projected on the film side face give an equivalent force at point B whose components are:

$$\begin{aligned} B_x &= \sigma_1 ul \sin\theta \\ B_y &= \sigma_2 ul \cos\theta \end{aligned} \tag{3.9}$$

The equilibrium equations of the diamond frame of Figure 39 are obtained from force and moment balances:

$$\begin{aligned} \sum F_x \quad &\rightarrow \quad C_x - B_x = 0 \\ \sum F_y \quad &\rightarrow \quad F_F + A_y - B_y = 0 \\ \sum M_{/B} &\rightarrow \quad A_y \frac{l}{2}\cos\theta - F_F \frac{l}{2}\cos\theta - B_x \frac{l}{2}\sin\theta = 0 \end{aligned} \tag{3.10}$$

The three equations (3.10) are solved for the film force. The resulting expression is multiplied by 2 to account for the second side of the actuator and gives:

$$F_F = B_y - B_x \tan\theta \tag{3.11}$$

Finally, combining Eqs. (3.9) and (3.11) gives an expression for the film force in function of the film planar stresses:

$$F_F = ul\left(\sigma_2 \cos\theta - \sigma_1 \tan\theta \sin\theta\right) \tag{3.12}$$

The planar stresses, σ_1 and σ_2, required in Eq. (3.12) are computed from the modified Bergstrom-Boyce model and kinematical description of diamond actuators

presented in Chapter 2. Note that the model is used with $\sigma_3 = 0$ because Maxwell pressure is modeled independently.

Maxwell Force, F_M :

Equation (3.12) is used to find the relation between the hydrostatic Maxwell pressure, P, and its reciprocal Maxwell force, F_M, by substituting for $\sigma_1 = \sigma_2 = -P$:

$$F_M = Pul\cos\theta\left(\tan^2\theta - 1\right) \tag{3.13}$$

The result of Eq. (3.13) was confirmed by using the virtual work principle (see reference [5]).

3.3.2 Experimental Validation

The full viscoelastic model was validated against five work cycle experiments. The results are shown in Figure 40 to Figure 44. The results show that, in general, the model agrees well with experiments, even when velocity is varied by more than three orders of magnitude. Also, it should be noted that the work cycles were conducted with many different actuators. Thus the model adapts well to the variability inherent in DE actuator manufacturing.

The model confirms that viscoelastic forces impede actuator output force as velocity increases until the force difference eventually becomes zero. The good prediction performance of the viscoelastic model suggests its reliability for engineering design use.

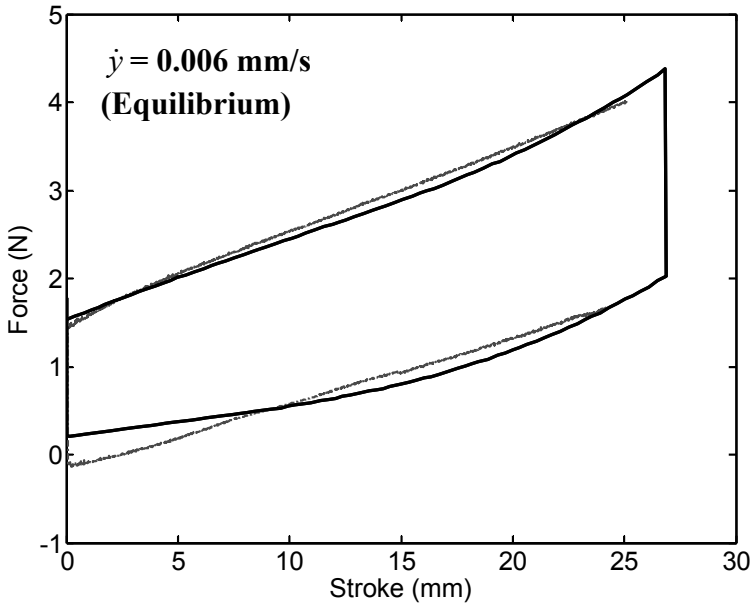

Figure 40: Viscoelastic model, prediction (dark) vs. experiment (light), case 1.

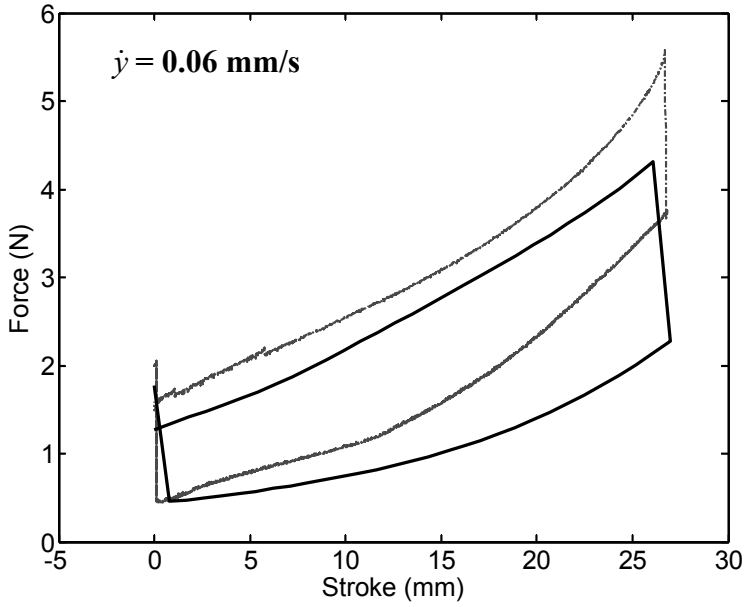

Figure 41: Viscoelastic model, prediction (dark) vs. experiment (light), case 2.

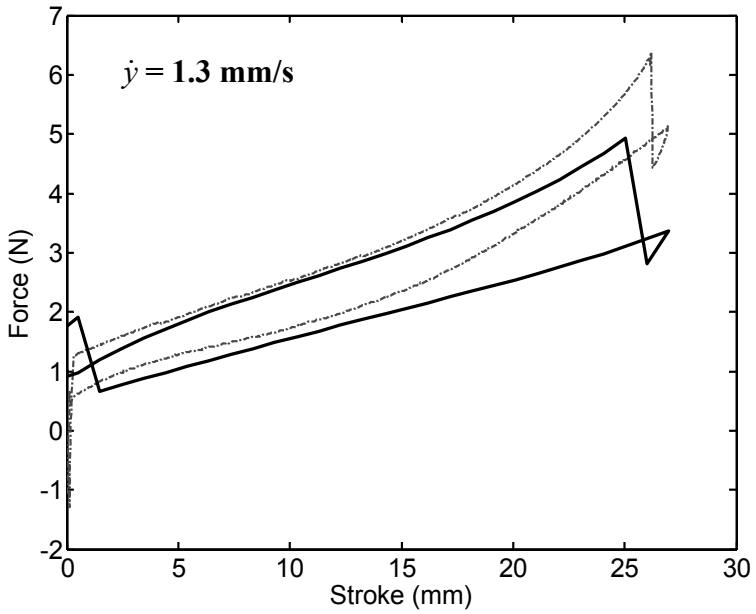

Figure 42: Viscoelastic model, prediction (dark) vs. experiment (light), case 3.

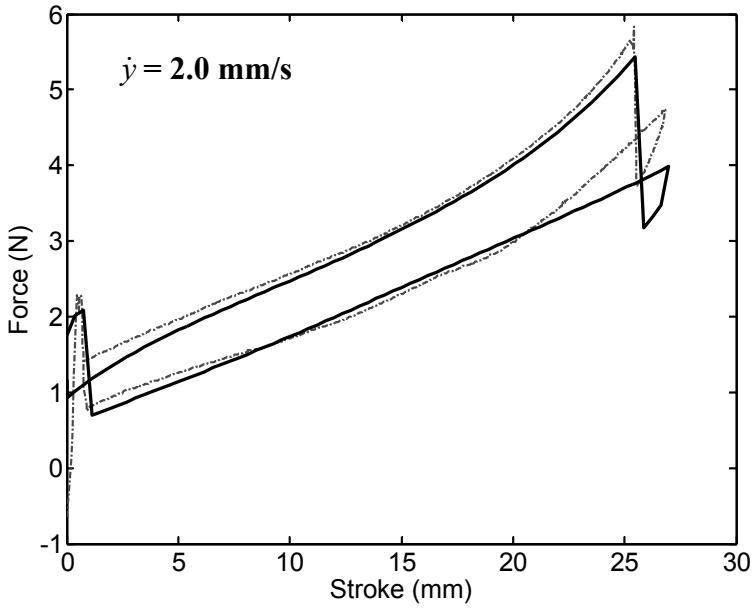

Figure 43: Viscoelastic model, prediction (dark) vs. experiment (light), case 4.

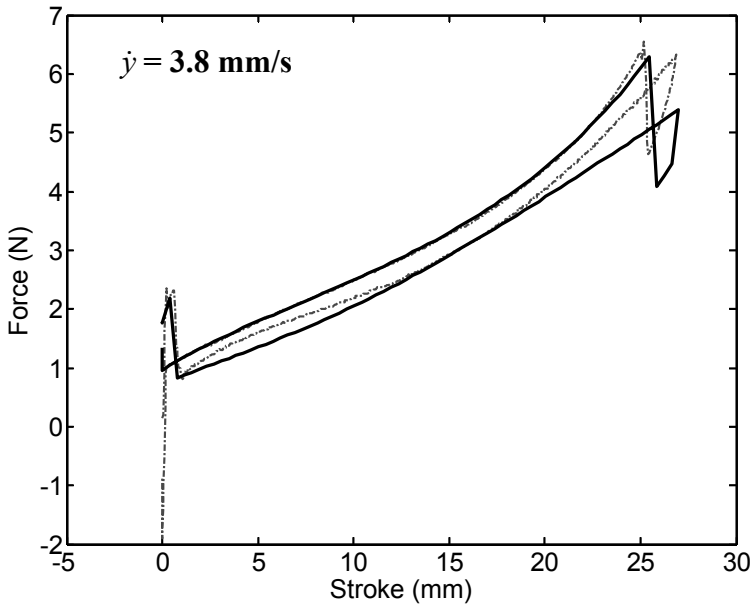

Figure 44: Viscoelastic model, prediction (dark) vs. experiment (light), case 5.

3.4 Current Leakage Model

An actuator current consumption model integrating possible current leakage mechanisms is developed. The objective of this model is to predict the current consumption map of the work cycle experiments (see Figure 30 on page 60).

3.4.1 Analytical Development

Electrical conduction in polymers depends on molecular microstructure and can be caused by many mechanisms acting simultaneously [66]. The objective here is not to describe the conductivity of polymers from a microscopic standpoint, but to study its general effects on performance.

The analysis is based on the thermodynamics of diamond actuators during work cycle experiments. Figure 45 represents such an actuator in its opening cycle where voltage is applied. The first law of thermodynamics in terms of power balance gives:

$$\dot{W}_{ELE} = \dot{W}_{MEC} + \dot{\xi} + \left(\dot{Q}_{DIFF} + \dot{Q}_{COND}\right) \tag{3.14}$$

where $\dot{W}_{ELE}$ is the electrical power, $\dot{W}_{MEC}$ is the mechanical power, $\dot{\xi}$ is the rate of change of the system's energy, $\dot{Q}_{COND}$ is the conductive current leakage, and $\dot{Q}_{DIFF}$ is the diffusive current leakage.

The terms of Eq. (3.14) are expressed in the next paragraphs as functions of the work cycle variables, $\Delta F, i, y, \dot{y}, V$, in order to predict the current consumption from work cycle measurements. In these experiments, the film deformation and viscous dissipation energy is supplied by the actuator dynamometer, and thus are not considered in balance of Eq. (3.14). The temperature rise of the film material and its effect on film properties are neglected.

The following development uses geometric relations for the film area, A, film volume, υ, and minor axis y given in terms of the geometric parameters l, u, and θ defined in Figure 15 on page 39:

$$A = 2l^2 \cos\theta \sin\theta \tag{3.15}$$

$$\upsilon = Au = 2ul^2 \cos\theta \sin\theta \tag{3.16}$$

$$y = 2l \sin\theta \tag{3.17}$$

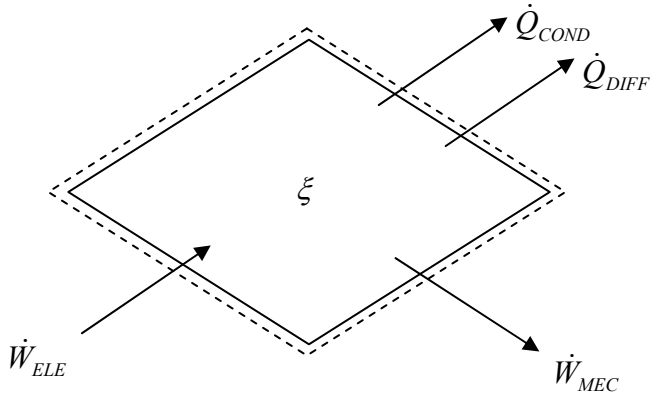

Figure 45: DE actuator thermodynamic system.

The electrical power input is:

$$\dot{W}_{ELE} = Vi \tag{3.18}$$

The mechanical power output is:

$$\dot{W}_{MEC} = \Delta F \dot{y} \tag{3.19}$$

The system's energy accumulation term, $\dot{\xi}$, is assumed to be solely caused by the electrical capacitance variation during actuation. The time rate of change of the energy stored in the capacitor is, under constant voltage:

$$\dot{\xi} = \frac{1}{2}\frac{dC}{dy}\dot{y}V^2 \tag{3.20}$$

The capacitance derivative, $\frac{dC}{dy}$, is found numerically from the plate capacitor equation, $C = \varepsilon\varepsilon_0 \frac{A}{u}$, expressed in terms of y using Eqs. (3.15) to (3.17):

$$C = \varepsilon\varepsilon_0 \frac{y^2 l^2}{\upsilon} \cos^2\left(\sin^{-1}\left(\frac{y}{2l}\right)\right) \tag{3.21}$$

The conductive current leakage heat loss term, $\dot{Q}_{COND}$, can be described by standard electronic conduction (Ohm's law):

$$R = \varphi \frac{u}{A} \tag{3.22}$$

where φ is the material's electrical resistivity, A is the film area, and u is the film thickness. The resistivity is assumed constant (in first approximation) but the area and thickness, A and u, change during extension. The heat loss due to conduction is thus given by:

$$\dot{Q}_{COND} = \frac{V^2}{R} = \frac{V^2 A}{\varphi u} \tag{3.23}$$

The diffusive current leakage heat loss term, $\dot{Q}_{DIFF}$, arises due to charge carriers that diffuse through the film under high electric fields, see Figure 46. These charge carriers locally increase the film conductivity by "doping" the polymer.

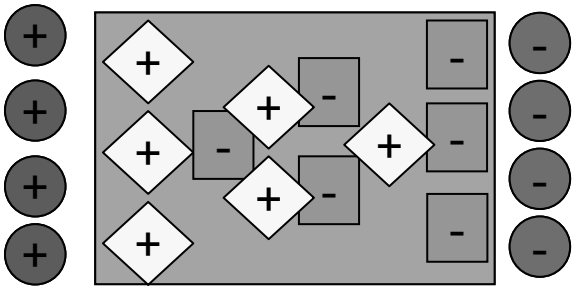

Figure 46: Diffusive current leakage process.

A first order diffusion model is derived from the Poisson-Nernst-Planck drift-diffusion model for ionic solutions. In this model, the constitutive law for the current flux, j (Amps/m^2), is given by [23]:

$$j(z,t) = \mu e E \eta(z,t) - eD\frac{\partial \eta(z,t)}{\partial z} \tag{3.24}$$

where E is the electric field, $\eta(z,t)$ is the charge carrier concentration, z is the position along the electric field (taken here as the film thickness), t is the time, e is the electron charge, μ is the mobility coefficient and D is the diffusion coefficient. For polymers, the current due to concentration gradients can be neglected (second term on the right hand side of Eq. (3.24)) [66]. Hence, the current is only function of the charge carrier concentration and can be expanded as the flux times the area as:

$$i(z,t) = \mu e E A \eta(z,t) \tag{3.25}$$

Substituting for the electric field, $E = \frac{V}{u}$, and film area, $A = \frac{\upsilon}{u}$, gives:

$$i(z,t) = \mu e \upsilon V \frac{\eta(z,t)}{u^2} \tag{3.26}$$

The charge carrier concentration in the film $\eta(z,t)$ is assumed to follow the well known diffusion equation:

$$\frac{\partial \eta(z,t)}{\partial t} = \alpha \frac{\partial^2 \eta(z,t)}{\partial z^2} \tag{3.27}$$

where α is the diffusion constant. As a first approximation, the film is assumed to behave like a semi-infinite medium, leading to the well-known solution of:

$$\eta(z,t) = (\eta_i - \eta_s)\text{erf}\left(\frac{z}{2\sqrt{\alpha t}}\right) + \eta_s \tag{3.28}$$

where η_s is the charge carrier concentration on the film surface and η_i is the concentration at infinity (far away from the surface). The diffusion current is limited by the smallest charge carrier concentration occurring at a depth equal to the film thickness $z = u$. Equation (3.28) evaluated at $z = u$ with $\eta_i = 0$ leads to:

$$\eta(t) = \left(1 - \text{erf}\left(\frac{u}{2\sqrt{\alpha t}}\right)\right)\eta_s \tag{3.29}$$

The diffusion current is given by combining Eqs. (3.26) and (3.29) and lumping constants in a single term K:

$$i(t) = K\frac{\left(1 - \text{erf}\left(\frac{u}{2\sqrt{\alpha t}}\right)\right)}{u^2}V \tag{3.30}$$

The corresponding diffusion leakage-based heat loss is then:

$$\dot{Q}_{DIFF} = K\frac{\left(1 - \text{erf}\left(\frac{u}{2\sqrt{\alpha t}}\right)\right)}{u^2}V^2 \tag{3.31}$$

The power balance of Eq. (3.14) can now be rewritten in terms of the work cycle variables by using Eqs. (3.18), (3.19), (3.20), (3.23) and (3.31):

$$Vi = \Delta F\dot{y} + \frac{1}{2}\frac{dC}{dy}\dot{y}V^2 + \frac{V^2 A}{\varphi u} + K\frac{\left(1-\mathrm{erf}\left(\frac{u}{2\sqrt{\alpha t}}\right)\right)}{u^2}V^2 \tag{3.32}$$

Dividing by the actuator voltage V and rearranging terms yields the current consumption model:

$$i = V\left(\frac{1}{2}\frac{dC}{dy}\dot{y} + \frac{A}{\varphi u} + K\frac{\left(1-\mathrm{erf}\left(\frac{u}{2\sqrt{\alpha t}}\right)\right)}{u^2}\right) + \frac{1}{V}\left(\Delta F\dot{y}\right) \tag{3.33}$$

The model parameters of Eq. (3.33) were defined by educated guesses and are summarized in Table 3.

Table 3: Current leakage model parameters

Parameters	Values	Units
α	$4\text{x}10^{-4}$	$mm^2.s^{-1}$
K	$1.1\text{x}10^{-8}$	$Amp.mm^2.V^{-1}$
φ	$1\text{x}10^{11}$	Ohm.m

3.4.2 Experimental Validation

The current consumption predictions were compared with experimental data on Figure 47. The model shows good agreement considering its numerous simplifications. The key trend followed by the analytical model is the large current consumption at large extensions and low speeds.

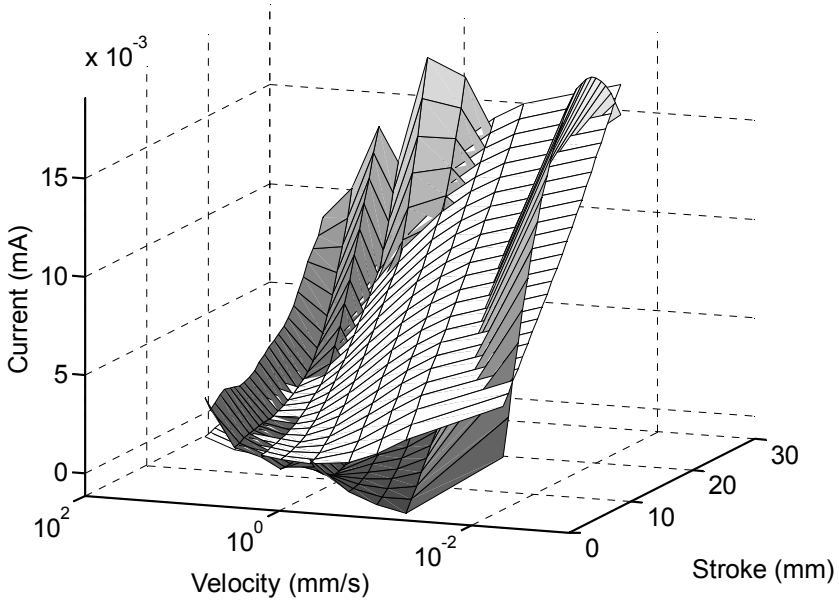

Figure 47: Current leakage model predictions (white) vs. experiments (grey).

Individual current maps of each term of Eq. (3.33) are shown on Figure 48. It can be seen that diffusion leakage, (c), dominates the overall current consumption by an order of magnitude (note the different vertical scales). This mechanism explains the high currents observed at both high strokes and low velocities. Conduction leakage, (b), shows that current flow increases with actuator stroke. However, values are much lower than diffusion leakage. The velocity dependent term of variable capacitance, (a), explains the higher currents observed at high velocities. The mechanical output power, (d), is very small with respect to total current consumption.

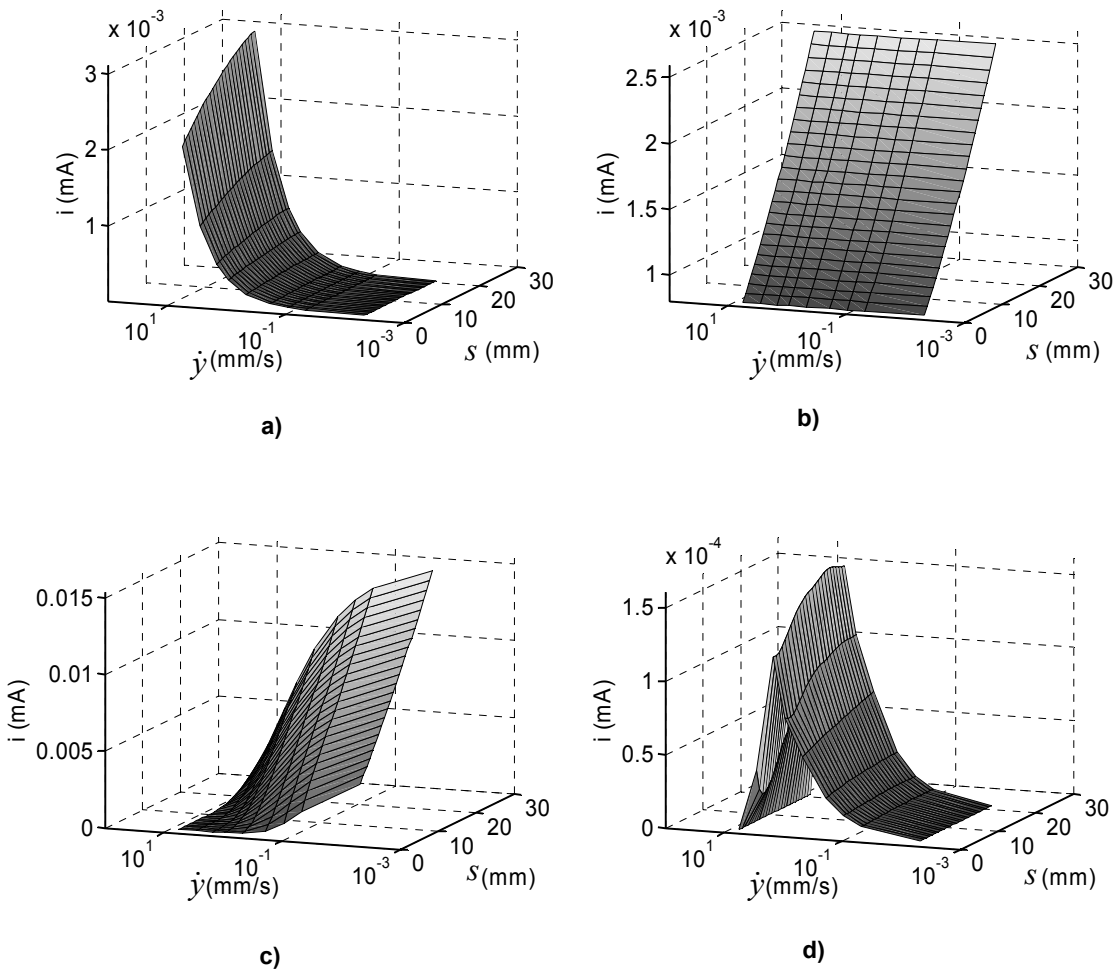

Figure 48: Current consumption of considered mechanisms: (a) variable capacitance, (b) conduction leakage, (c) diffusion leakage, and (d) mechanical power output.

3.5 Chapter Summary

This chapter presented an experimental and analytical study of the performance of DE actuators. Viscoelasticity was studied with a Bergstrom-Boyce polymer model which explains how DE actuator forces attenuate when velocity increases. The current leakage model shows how diffusion leakage dominates actuator current consumption. Such high

leakage degrades efficiency at high stroke and low velocity. Current leakage is still a very complex mechanism that needs further investigation to be fully understood.

CHAPTER

4

MODELING AND ANALYSIS OF FUNDAMENTAL FAILURE MODES OF DIELECTRIC ELASTOMER ACTUATORS

4.1 Introduction

The objective of this chapter is to provide an engineering-based answer to the question of whether or not DE technology can be used reliably in practical applications. DE reliability is assessed here by identifying the failure modes and associated performance limits as well as the working conditions leading to failure. An analytical model of DE actuation is developed. Failure criteria are then formulated and used to predict failure under various working conditions. The predictions are verified experimentally and conclusions are drawn.

4.2 Analytical Model

The majority of practical DE actuators developed to date are variants of what can be called rolled and planar classes [34,62,83]. These designs provide good mechanical energy conversion perspective, but are sensitive to localized failure modes such as stress concentrations at the film edges [55]. To minimize these unwanted local effects, this study considers ideal actuators such as described in Chapter 2. The film deformation of these devices occurs far away from the film's attachment point ($r_{rig} > r_{act}$) and local

failures due to the film bonding interface are minimized, putting emphasis on fundamental or large scale failure modes. Some of these local failure modes are addressed elsewhere [80].

Here, analytical models of fundamental failure modes of ideal actuators are developed that reflect the basic physics of DE actuation under a range of working conditions. These models are challenging. They must consider the very large deformations, nonlinear elastic behavior, viscoelasticity, and varying dielectric strength of DE actuators. In the analysis presented here, the following basic assumptions/restrictions are made:

- The film is a hyper-elastic material. The film's viscoelasticity is modeled by defining different elastic material models at different stretch rates. Hence, all deformations are assumed to occur at constant stretch rates. This strategy is more flexible and reliable than the Bergstrom-Boyce model used in Chapter 3. These advantages are a must when studying various failure criteria under broad pre-stretch range and different loading conditions.
- As shown experimentally in Section 4.3.2, the effect of non-equibiaxial pre-stretches on failure is of secondary importance.
- The material's dielectric strength for a given stretch state is obtained experimentally.

4.2.1 Ideal Actuator Model

Based on the kinematical description of ideal actuators of Chapter 2, the objective is to find the actuation stretches, $\lambda_{i,act}$, for any given voltage, V, pre-stretch, $\lambda_{i,pre}$, and stretch rate of the uniaxial test used to define the elastomer constitutive model, $\dot{\lambda}_{UNI}$:

$$\lambda_{i,act} = f(V, \lambda_{i,pre}, \dot{\lambda}_{UNI}) \qquad i = 1,2,3 \tag{4.2}$$

Equation (4.2) doesn't have an explicit solution. To solve this problem, the model is expressed in terms of voltage:

$$V = f(\lambda_{i,pre}, \lambda_{i,act}, \dot{\lambda}_{UNI}) \qquad i = 1,2,3 \tag{4.2}$$

and the actuation stretches are found from a numerical inverse.

The ideal DE actuator is separated in two distinct regions: the *active region* and the *passive region*, see Figure 49. Each region is modeled separately and boundary conditions are applied between the two. The active region model is described bellow whereas the passive region and boundary condition are presented in Appendix E.

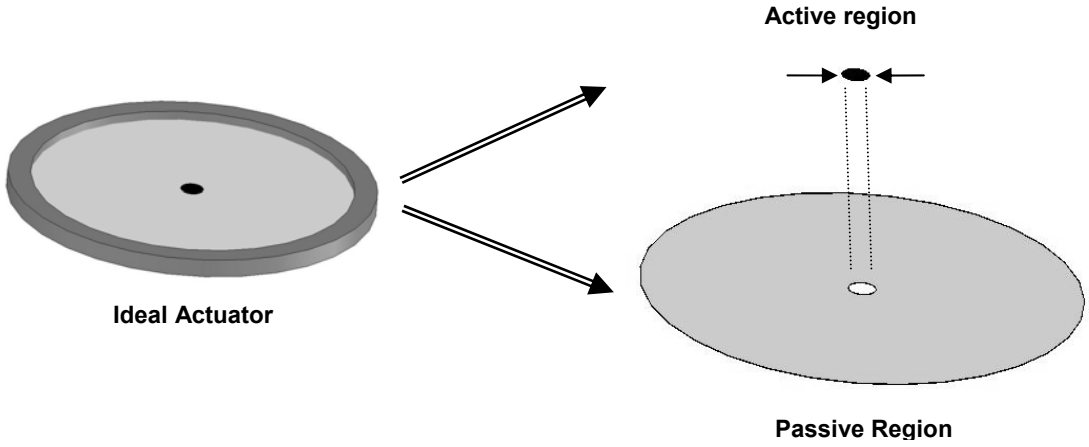

Figure 49: Ideal actuator decomposed into active and passive regions.

Referring to Figure 18 on page 42, the radial actuation stretch, $\lambda_{1,act}$, is reached when the equivalent Maxwell pressure, P, of Eq. (1.1) is in equilibrium with the film's axial stress:

$$P(V,\lambda_{1,pre},\lambda_{1,act}) = -\sigma_{3,act}(\lambda_{1,pre},\lambda_{1,act}) \tag{4.3}$$

The axial stress, $\sigma_{3,act}$, is obtained by writing Ogden's stress formulation as given by Eq. (2.22) of Chapter 2 in the actuated configuration:

$$\begin{aligned}
\sigma_{1,act} &= -p + \mu_1\left(\lambda_{1,tot}\right)^{\alpha_1} + \mu_2\left(\lambda_{1,tot}\right)^{\alpha_2} \\
\sigma_{2,act} &= \sigma_{1,act} \\
\sigma_{3,act} &= -p + \mu_1\left(\lambda_{3,tot}\right)^{\alpha_1} + \mu_2\left(\lambda_{3,tot}\right)^{\alpha_2}
\end{aligned} \tag{4.4}$$

The first component of Eq. (4.4) gives the hydrostatic pressure p:

$$p = \mu_1\left(\lambda_{1,tot}\right)^{\alpha_1} + \mu_2\left(\lambda_{1,tot}\right)^{\alpha_2} - \sigma_{1,act} \tag{4.5}$$

which is then inserted back into the third component of Eq. (4.4) to give a closed form expression of the axial stress:

$$\sigma_{3,act} = \sigma_{1,act} - \mu_1\left(\lambda_{1,tot}\right)^{\alpha_1} - \mu_2\left(\lambda_{1,tot}\right)^{\alpha_2} + \mu_1\left(\lambda_{3,tot}\right)^{\alpha_1} + \mu_2\left(\lambda_{3,tot}\right)^{\alpha_2} \tag{4.6}$$

The film planar stress $\sigma_{1,act}$ in Eq. (4.6) is obtained from the passive region model presented in Appendix E.

4.2.2 Failure Criteria

Three failure modes are considered: material strength, dielectric strength, and pull-in, see Figure 50. Failures that result from localized effects such as material defects, stress concentration, and field concentration are not considered here [80].

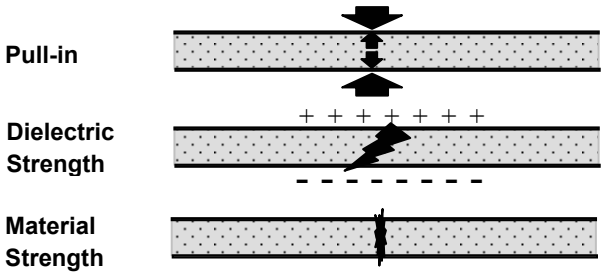

Figure 50: Failure modes of DE actuators.

The failure criteria are described in terms of area expansion ratio: $A_{final} / A_{initial}$, which is equal to the inverse of the axial stretch and to the square of a planar stretch:

$$\frac{A_{final}}{A_{initial}} = \frac{1}{\lambda_3} = \lambda_1^2 \tag{4.7}$$

Under equibiaxial assumption, area expansion is essentially equivalent to the more common effective stretch concept [2]:

$$\overline{\lambda} = \frac{1}{\sqrt{3}} \sqrt{\lambda_1^2 + \lambda_2^2 + \lambda_3^2} \tag{4.8}$$

Material Strength Failure

Material failure occurs when folded polymer chains are straightened beyond their unfolded length. This kind of failure is thus primarily a function of stretch and not stress. Therefore, the models developed above to compute the stresses are not required to predict material strength failures. Material strength failures take place when the film area expansion is higher than the film's experimentally determined limit of 36 [40,33]:

$$\lambda_{1,tot}^2 > 36 \tag{4.9}$$

Dielectric Strength Failure

The breakdown voltage limit of a dielectric material is generally obtained experimentally. Predicting dielectric failure with reasonable accuracy from theoretical models requires representing the complex molecular and atomic interactions and is not tractable [81]. Dielectric failure is thus predicted from an empirical breakdown voltage vs. total stretch curve obtained for rigid (non-deforming) electrodes, see Figure 56 in Section 4.3.2. The maximum actuation stretch is obtained when the model's electric field is higher than the experimental dielectric strength:

$$E > E_{EXP}(\lambda_{1,tot}) \tag{4.10}$$

Pull-in Instability Failure

Pull-in instability appears when the equilibrium condition of Eq. (4.3) cannot be reached and the film collapses into highly complex 3D wrinkling patterns, eventually leading to failure, see Figure 51. Ultimately, the failure either comes from a dielectric or material breakdown. This study considers a simplified one dimensional model capable of predicting the onset of pull-in instability.

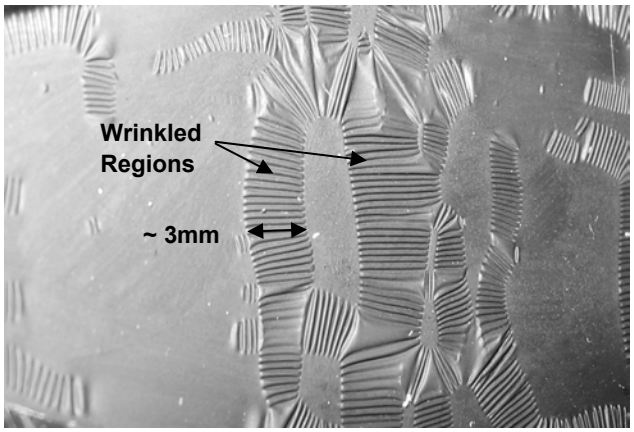

Figure 51: Film geometry during pull-in instability.

Pull-in instability occurs when the magnitude of the Maxwell pressure, P, increases at a greater rate than the film axial stress $\sigma_{3,act}$. For a given pre-stretch, the pull-in threshold is found by analyzing the equilibrium between the two opposing stresses as shown in Figure 52. The axial stress magnitude, $\left|\sigma_{3,act}\right|$, obtained from Eq. (4.6) is plotted as a function of actuation stretch. Also shown are the equivalent Maxwell pressures, P, obtained from Eq. (1.1) at three different voltages as a function of actuation stretch. The location of the ultimate actuation stretch before pull-in is at the value of the tangent point of the *last* Maxwell pressure curve, P, to intersect the film's axial stress curve, $\left|\sigma_{3,act}\right|$. Voltages below the critical pull-in voltage are stable while those above are unstable. Figure 52 shows that voltage V_1 has a stable solution, V_3 would result in pull-in, and voltage V_2 is the critical pull-in voltage for this material and pre-stretch.

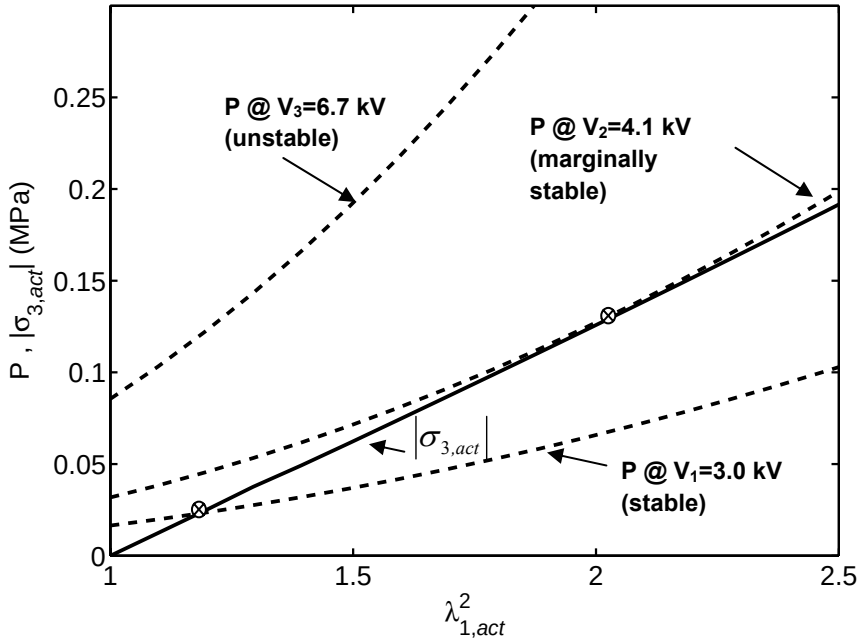

Figure 52: Example of pull-in failure criterion.

As shown in Figure 52, the location of the equilibrium point is sensitive to the material's stress response. VHB 4905/4910 is a highly viscoelastic material whose stress

level is strongly affected by stretch rate, see Appendix C. Hence, it is reasonable that pull-in failure is strongly affected by stretch rate.

4.2.3 Failure Predictions

The analytical model and failure criteria were used to predict the ultimate actuation vs. pre-stretch area expansion of an ideal actuator. Predictions were made for three different stretch rates, respectively called very high, high and low stretch rates and corresponding to $\dot{\lambda}_{UNI}$=1.8 s^{-1}, 0.094 s^{-1} and 3.3x10^{-4} s^{-1}. The very high stretch rate of $\dot{\lambda}_{UNI}$=1.8 s^{-1} represents the highest rates allowed by the film's viscous effects. The high stretch rate of $\dot{\lambda}_{UNI}$=0.094 s^{-1} is typical of many DE applications, while the low stretch rate of $\dot{\lambda}_{UNI}$=3.3x10^{-4} s^{-1} is the equilibrium rate where viscoelastic effects are negligible, see Appendix C. Results are shown in Figure 53 to Figure 55 where the active failure mode is the one predicting the lowest actuation area expansion.

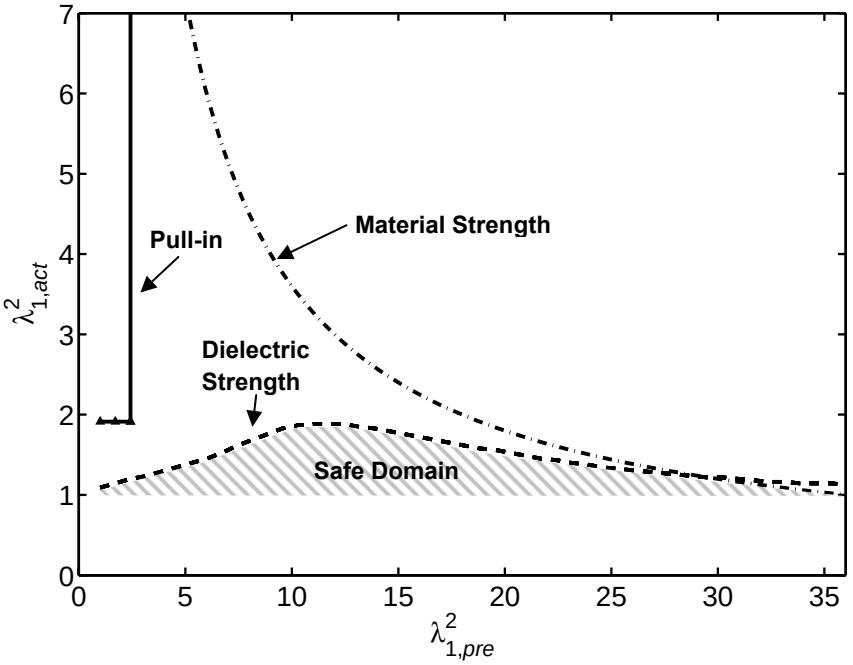

Figure 53: Calculated actuation area expansion at failure as a function of area pre-stretch at very high stretch rates ($\dot{\lambda}_{UNI}$ =1.8 s^{-1}).

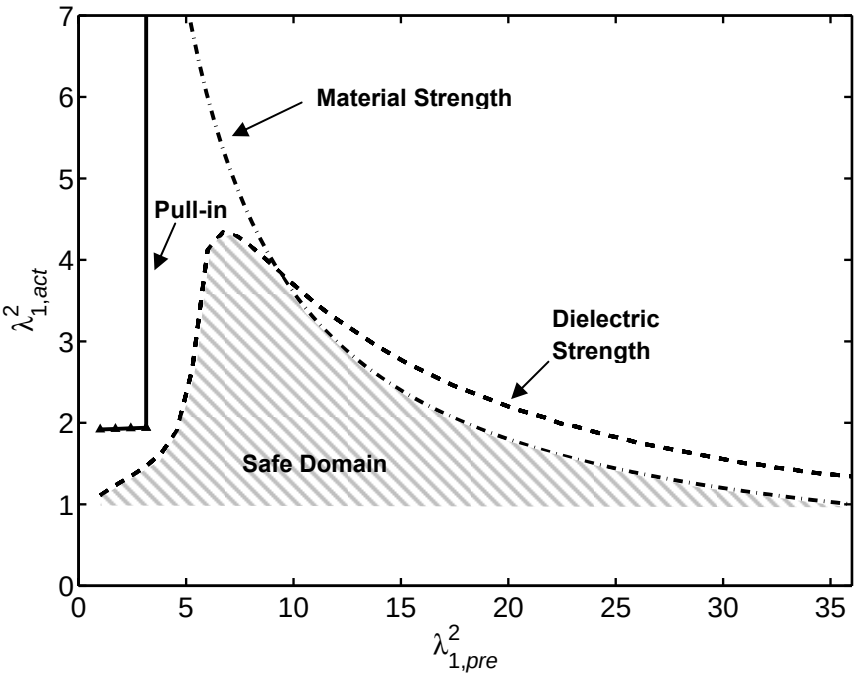

Figure 54: Calculated actuation area expansion at failure as a function of area pre-stretch at high stretch rates ($\dot{\lambda}_{UNI}$ =0.094 s^{-1}).

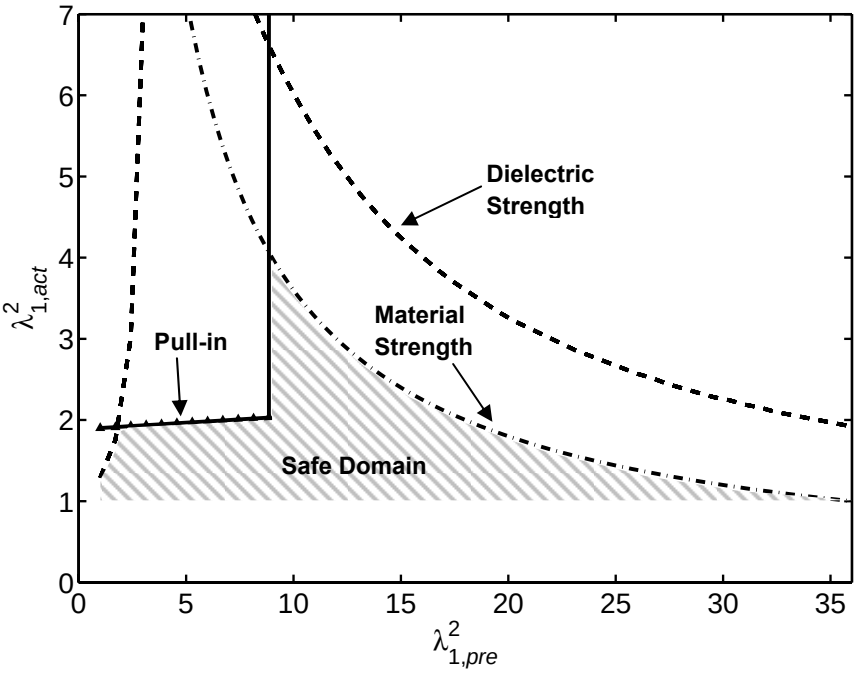

Figure 55: Calculated actuation area expansion at failure as a function of area pre-stretch at low stretch rates ($\dot{\lambda}_{UNI}$ =3.3x10^{-4} s^{-1}).

For very high stretch rates, the analysis predicts that DE failure is dominated by dielectric strength, see Figure 53. Material strength failure is only present at pre-stretches above 30. Pull-in failure predictions give finite values only for low pre-stretches of about 3. After this, pull-in failure disappears and is not relevant. At these stretch rates, a maximum extension of about 2 is reached for a pre-stretch of about 11.

At high stretch rates, the analysis predicts that DE failure is caused by two modes, see Figure 54. The dielectric strength mode dominates failure for pre-stretches of 1 to 10. For pre-stretches above 10, failure is dominated by the material strength. Comparing the dielectric strength failure predictions at high and very high stretch rates show that viscoelasticity limits extension of DE actuators as stretch rate increases. At $\dot{\lambda}_{UNI}$=0.094 s^{-1} (Figure 54) the maximum expansion is about 4 while at $\dot{\lambda}_{UNI}$=1.8 s^{-1} (Figure 53) it is reduced to about 2. As stretch rate increases, the film's viscous impedance increases and thus requires higher voltages to achieve similar expansion. Hence, the material's dielectric strength limit is reached sooner.

For low stretch rates, the analysis predicts that DE failure is caused by all three modes, see Figure 55. Pull-in failure dominates the low pre-stretch range and material strength failure dominates the high pre-stretch range; the transition occurs at pre-stretches of about 10. Dielectric strength failure is only a factor at very low pre-stretches that are not of practical use. Pull-in failure limits maximum area expansion to a relatively constant value of about 1.9. This value is not very far from the linear (Hookean) model predictions discussed in the introduction, giving a limit of 1.6 [37,57,74]. This is likely because at low rates, the equilibrium stress/stretch curve is almost linear (see Figure 100 of Appendix C).

The differences between low- and high- stretch rate failure predictions show the fundamental role of viscoelasticity on actuator failure. Viscoelasticity significantly

affects the amount of viscous impedance at high stretch rates, see Appendix C. These viscous forces "stiffen" the film and protect it from pull-in failures, leaving place for dielectric strength failures. In contrast, low stretch rates generate less viscous impedance and pull-in failures dominate.

4.3 Experiments

Laboratory experiments were performed to validate the models and failure mode criteria. Experimental data was obtained at low ($\dot{\lambda}_{UNI}$=3.3x10^{-4} s^{-1}) and at high ($\dot{\lambda}_{UNI}$=0.094 s^{-1}) stretch rates. Priority was set on high stretch rates where actuation rates are matters of seconds rather than hours. Such time scales are representative of most practical robotics and mechatronics applications.

4.3.1 Data Acquisition

At high stretch rates, the electrode boundary is constantly moving and its dimensions at failure are difficult to measure. Optical methods are cumbersome and do not detect any film out-of-plane deformation (wrinkling) that might occur at high actuation stretches. Hence, a method was developed to measure the area expansion at failure.

In this method, the polymer film is stretched to given values and then sandwiched between a set of rigid electrodes. A voltage is then applied and gradually increased until arcing occurs across the material (dielectric breakdown). In this way the material's breakdown voltage as function of stretch state can be determined. The rigid electrodes maintain the constant stretch state of the material. In contrast, if voltage is applied with compliant electrodes, its stretch state will change. The stretch states at breakdown can be determined from the calibration obtained with the rigid electrodes that gives the

breakdown voltage vs. stretch states. The difference in stretch states between the rigid and compliant cases is the actuation stretch.

At low stretch rates, electrode expansion is slow enough to enable continuous measurement. Electrode extension and stretch were thus measured directly.

The electrodes must be applied in an accurate and repeatable way. Hence the expanding electrodes applied to the film were squares instead of circles because they can be easily created by intersecting two lines, one on each side of the film. The difference in shapes should not be significant in the measured maximum area expansion.

In all tests, a sample of VHB 4905/4910 was pre-stretched in two perpendicular planar directions as described in Appendix B. Pre-stretch conditions included both symmetric, $\lambda_{1,pre} = \lambda_{2,pre}$, and highly asymmetrical cases, $\lambda_{1,pre} \neq \lambda_{2,pre}$. Rigid and compliant electrodes were placed in the middle of large pre-stretched films and the breakdown voltage was measured. A conducting water based gel was used for the 10x10mm compliant electrodes. An aluminum foil was used for rigid electrodes. It adheres well to the film and prevents deformation. Voltage was applied to the electrodes and increased with a Matsusada U3A-10P DC-DC voltage converter until failure was observed. The voltage application rate matched the uniaxial test stretch rates.

4.3.2 Experimental Results

Figure 56 shows the experimental voltage as a function of area pre-stretch for rigid and compliant electrodes at high stretch rate. The compliant electrodes curve was obtained from 28 points. The rigid electrode curve was obtained from 45 points and is compared with data extrapolated from Kofod et al. [33]. The comparison shows good agreement except at $\lambda_{1,pre}^2$=1.0, which is off by a factor of two due to an error in the presentation of the paper (Verified by private communication with Kofod on 4/11/2003).

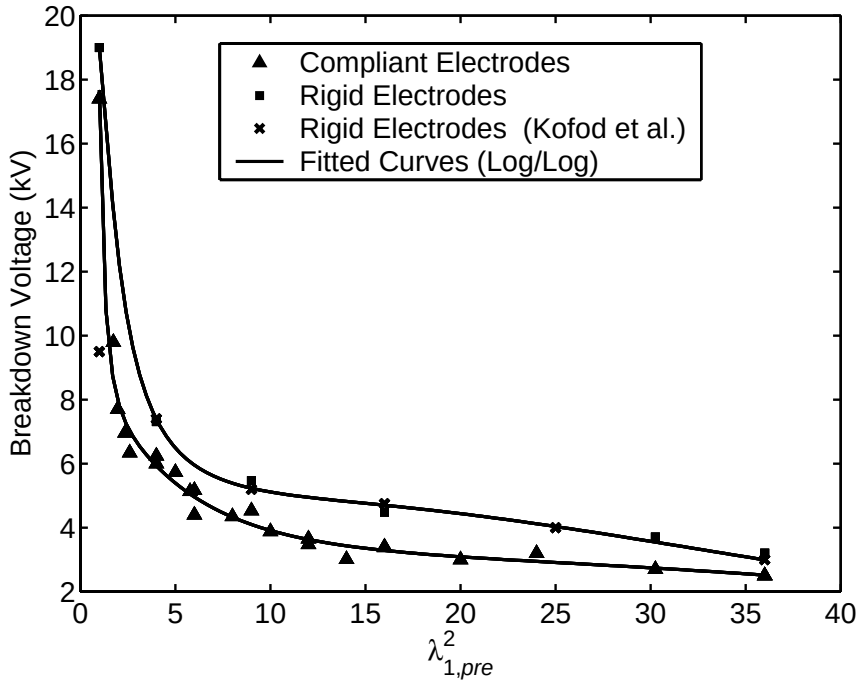

Figure 56: Experimental breakdown voltages for rigid and compliant electrodes measured at high stretch rate ($\dot{\lambda}_{UNI}$ =0.094 s^{-1}).

The fact that equibiaxial pre-stretches have a secondary effect on failure is demonstrated with the compliant electrode curve of Figure 56. The compliant electrode data contains both highly asymmetric pre-stretch combinations such as $\lambda_{1,pre}$x$\lambda_{2,pre}$ = 11x0.525 as well as symmetric combinations like $\lambda_{1,pre}$x$\lambda_{2,pre}$ = 6x6. However, there is no significant difference that can be attributed to pre-stretch symmetry (or lack of it) leading to the conclusion that failure depends principally on area expansion.

The experimental actuation area expansion to failure is plotted vs. pre-stretch area expansion at high stretch rates is shown in Figure 57 with error boundaries of ± 30% representing an estimate of experimental data scatter range. The mean curve of Figure 57 appears smooth because it is obtained from the two data curve-fits of Figure 56. The experimental curve of Figure 57 appears lower than best values reported in literature [60]. The experimental curve may represent a conservative average of DE performance, assuming the reported values in the literature were obtained at similar stretch rates.

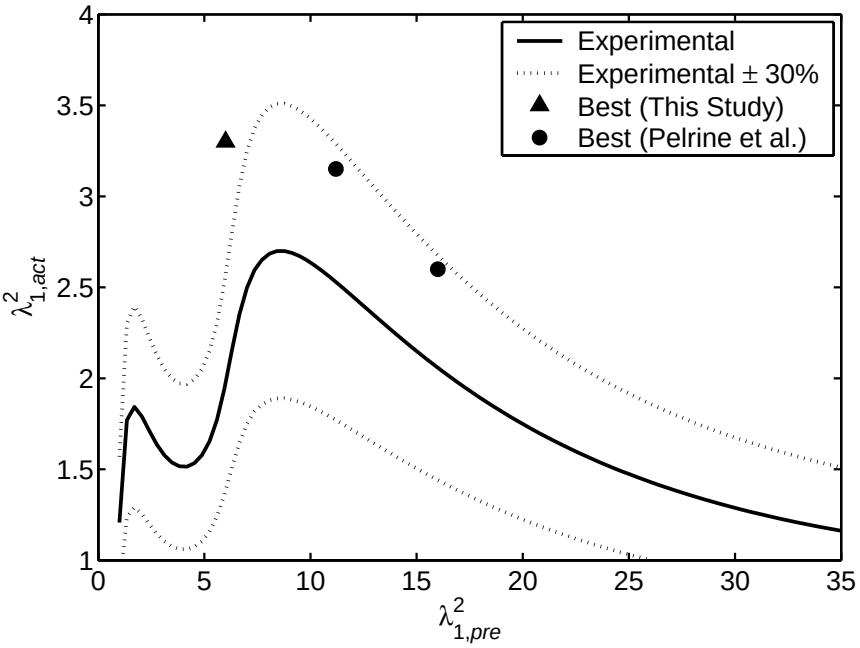

Figure 57: Experimental ultimate actuation area expansion vs. pre-stretch area expansion at high stretch rate ($\dot{\lambda}_{UNI}$ =0.094 s^{-1}).

Experimental data for low stretch rates was obtained for three different pre-stretches. Each case was repeated four times and the average values are presented in Table 4.

Figure 57 and Table 4 show that experimental actuation area expansion shows an optimum value around pre-stretches of 10 for both high and low stretch rates.

Table 4: Experimental actuation area expansion at failure for low stretch rate, $\dot{\lambda}_{UNI}$ =3.3x10^{-4} s^{-1}

$\lambda^2_{1,pre}$	$\lambda^2_{1,act}$	$\min(\lambda^2_{1,act})$	$\max(\lambda^2_{1,act})$	Observed Failure Mode
5	1.77	1.60	1.92	Pull-in
10	4.29	3.50	4.60	Dielectric or Material
16	2.86	2.25	3.36	Dielectric or Material

4.4 Model Validation

The failure predictions are first validated for ideal actuators. The predictions are then extended to diamond actuators where the effect of an external load is considered.

4.4.1 Ideal Actuators

In Figure 58, the model predictions at high stretch rates ($\dot{\lambda}_{UNI}$=0.094 s^{-1}) are compared against experimental data. The experimental curve is bounded by the failure criteria. Low pre-stretches failures are bounded by mixed pull-in and dielectric strength effects, medium pre-stretches by dielectric strength, and finally, large pre-stretch by material strength. The model and experimental curves both show an optimum pre-stretch at about 10. In the pre-stretch range of 5 to 15, the model over-predicts the maximum actuation area expansion (4.25 vs. 2.7). This discrepancy at high actuation stretches is principally attributed to the simplicity of the membrane assumption used for the passive region and its associated boundary condition, see Appendix E.

At low stretch rates ($\dot{\lambda}_{UNI}$=3.3x10^{-4} s^{-1}), the model agrees well with experimental data, see Figure 59. On the figure, the vertical lines across experimental points represent data scatter. As pre-stretch increases beyond a certain threshold, of about $\lambda_{1,pre}^2$=9, pull-in failure disappear, allowing very large actuation area expansions, up to 4.29 at $\lambda_{1,pre}^2$=10.

The experimental comparisons at low and high stretch rates suggest the model and failure criteria to be valid. Experimental data show that, for an optimum pre-stretch of $\lambda_{1,pre}^2$=10, low stretch rates yield higher extensions. However, this conclusion only stands for ideal actuators (no external loads) and is thus of no practical use.

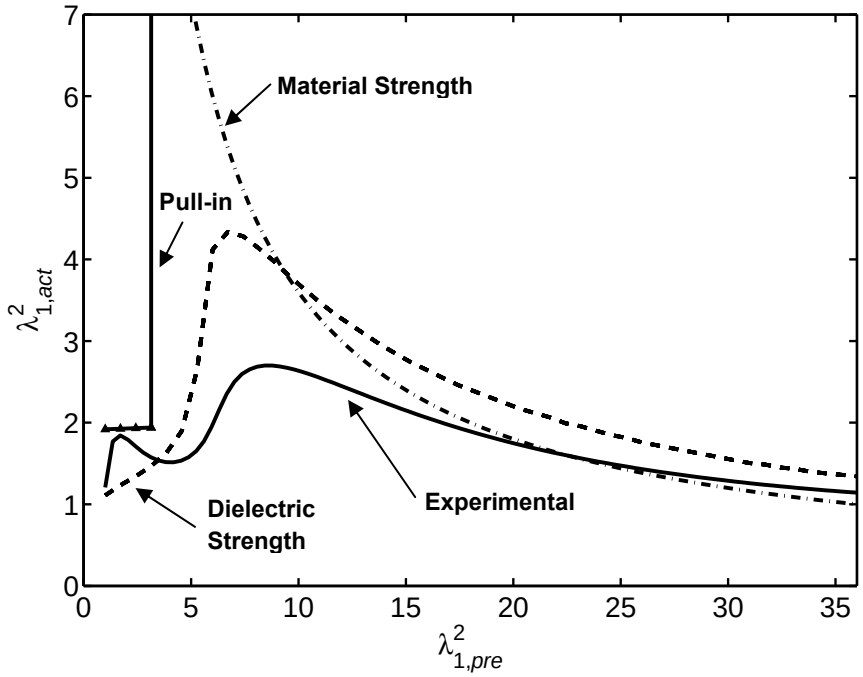

Figure 58: Failure analytical predictions for high stretch rate ($\dot{\lambda}_{UNI}$ =0.094 s^{-1}) compared with experimental values.

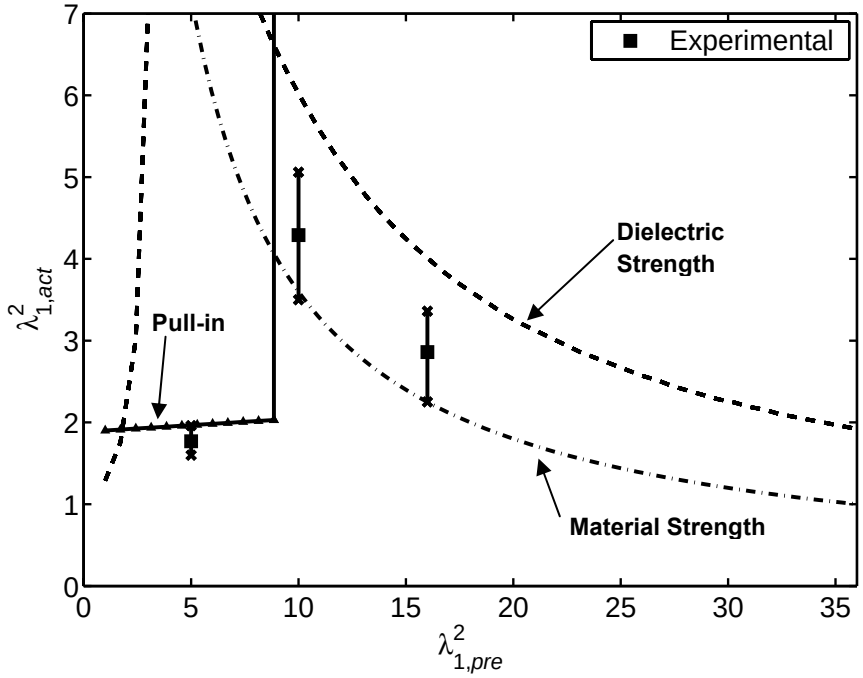

Figure 59: Failure analytical predictions for low stretch rate ($\dot{\lambda}_{UNI}$ =3.3x10^{-4} s^{-1}) compared with experimental values.

4.4.2 Diamond Actuators with External Load

The dependence of failure on stretch rates is extended to diamond actuators to study the effect of external loads on failure. These loads translate into lower film planar stresses (lower stresses meaning more compressive stresses). The external load is incorporated in the ideal actuator model by adding a loading stress typical of diamond actuators to the active region's boundary condition, see Eq. (E.12) of Appendix E, and computing new failure predictions.

To validate these new predictions, ten 107 mm diamond-shaped actuators were manufactured (see Figure 9 on page 30). Film pre-stretches of $\lambda_{1,pre}$x$\lambda_{2,pre}$ = 5x2.2 were used for a total pre-stretched area expansion ratio of 11. The actuators were pulled by the velocity controlled apparatus described in Section 3.2.1 with an applied voltage of 10 kV up to linear actuation strains of 150% (or equivalently, area expansions of 2.28). The samples were first pulled at high stretch rate and none of them failed. The same samples were then pulled for a second time at low stretch rate and it was observed that all 10 failed. Cumulative damage is considered negligible over only 2 cycles. The average linear strain at failure was 30% (or equivalently, an area expansion of 1.28) with a lowest value of 6% (or equivalently, an area expansion of 1.05). All failures showed the characteristic pull-in pattern of Figure 51.

The modified analytical model predictions are compared with the experimental data of the 10 diamond actuators in Figure 60 and Figure 61 for high and low stretch rates. The predictions corroborate well with the diamond actuator data showing severe pull-in limitations at low stretch rates. Based on these results, practical actuators appear to be severely limited by pull-in failure compared to ideal actuators due to external loads.

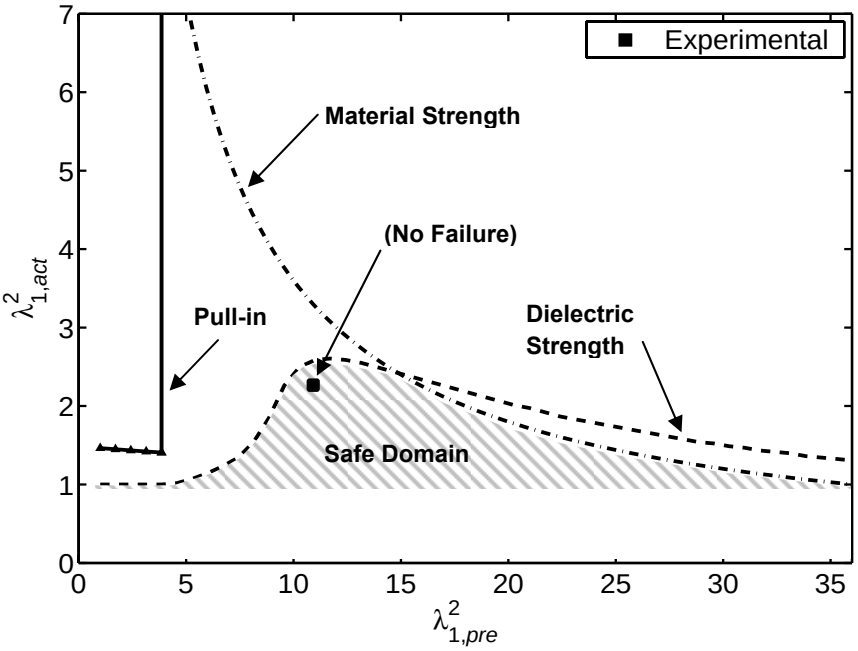

Figure 60: Failure analytical predictions for high stretch rate ($\dot{\lambda}_{UNI}$ =0.094 s^{-1}) with loading stress compared with experimental values of 10 diamond actuators.

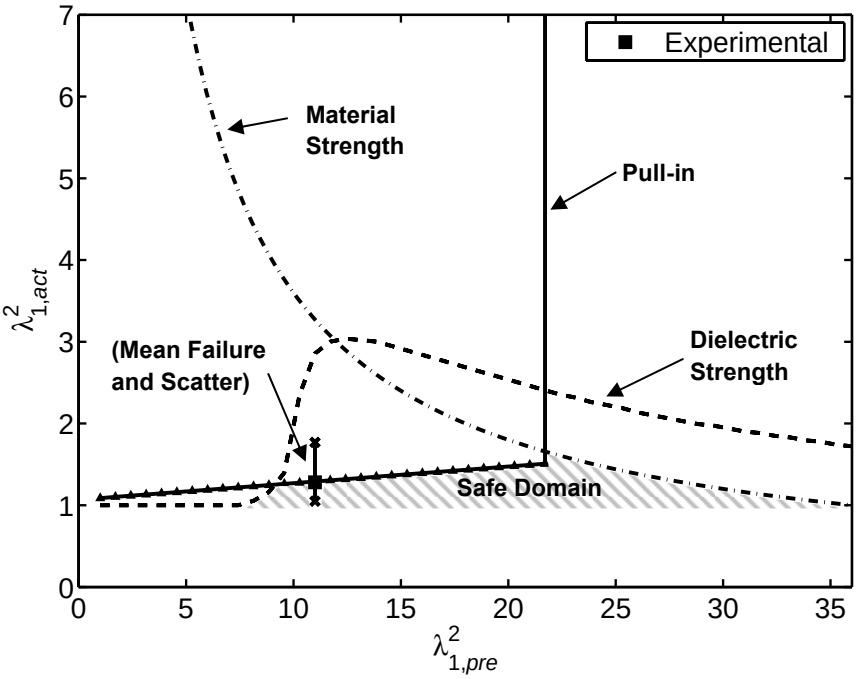

Figure 61: Failure analytical predictions for low stretch rate ($\dot{\lambda}_{UNI}$ =3.3x10^{-4} s^{-1}) with loading stress compared with experimental values of 10 diamond actuators.

As mentioned in Section 4.2.3, the difference in failure modes with stretch rates is attributed to internal viscous forces that help to prevent pull-in failure when operating at high stretch rates. This mechanism has a significant impact on practical actuator performance as possible linear extensions increase from 30% to 150% when used at high stretch rates, a five fold variation.

It can be concluded that, the severe pull-in limitation of practical DE actuators using VHB 4905/4910 and operating at low stretch rate, makes them unpractical for slow continuous operation. A solution to this is binary robotics using bistable actuators such as developed in Chapter 6.

4.5 Chapter Summary

Models of DE elastomer actuation were developed using a continuum mechanics framework for hyper-elastic materials. Rate dependent effects were captured by specifying different material properties for different stretch rates. Three large-scale failure criteria were established: material strength, dielectric strength and pull-in. These criteria were used in conjunction with the actuation models to predict ultimate area expansion of an ideal actuator configuration at three different stretch rates. The predictions were corroborated experimentally. However, care should always be taken when extrapolating these data to other actuator designs with different working conditions.

The answer to the question of whether or not VHB 4905/4910 actuators can be used reliably is: yes, if and only if they operate at high stretch rates. More specifically, this study leads to the following practical design guidelines and performance boundaries defined for DE actuators made with VHB 4905/4910 (or other similar materials):

1. DE actuators have failure modes and performance bounds that depend strongly on stretch rate. Dielectric strength failure is the dominant mode

of failure under high stretch rates. In contrast, pull-in instability is the performance limiter at low stretch rates.

2. For DE actuators operating at high stretch rates under load, a pre-stretch area expansion between 10 and 15 should be used to maximize actuation expansion. Actuation area expansions of up to 2.5 are possible (see Figure 60), giving diamond actuator linear extensions of 150%.
3. For DE actuators operating at low stretch rates under load, actuation area expansion is limited to about 1.28 regardless of the pre-stretch (see Figure 61), giving diamond actuator linear extensions of 30%.

Moreover, the study of DE actuator failure modes shows the properties of the ideal film material:

- Properly tuned stress/stretch behavior, just enough to prevent pull-in;
- Little or no viscoelastic effects (unless viscous impedance prevents pull-in failure, like VHB 4905/4910);
- Highest possible dielectric strength to prevent voltage breakdown failures;
- Highest possible extensions to prevent material failure;
- Highest dielectric constant to maximize Maxwell pressure;
- Lowest level of defects and contaminants to insure consistency.

CHAPTER

5

THE DESIGN OF DIELECTRIC ELASTOMER ACTUATORS

5.1 Introduction

The results of the performance and reliability studies presented in Chapters 3 and 4 provided models of DE actuators and allowed the question of how to design reliable, high performance DE actuators to be addressed by presenting new design tools that reflects the true physics of DE actuators.

5.2 Technical Benchmark: DE Actuators vs. Voice Coils

First, DE actuators are benchmarked against well-known voice coils actuators. Voice coils are nothing but linear versions of DC motors and the comparison can therefore safely be extended to DC motors operating without gearbox. The comparison is done between the 107 mm diamond actuator described in Table 1 on page 33 and a state-of-the-art commercially available DC voice coil.[1] The comparison is conducted on various performance metrics as well as on the basic physical mechanisms of each technology.

[1] BEI Kimco Magnetic division, part number LA15-26-000A, see: http://www.beikimco.com/

5.2.1 Performance Metrics

Strains: Linear strains of 150% are possible with DE actuators and up to 200% have been demonstrated [79]. Voice coils are fundamentally limited to values bellow 100% where the male and female sliding parts separate. The reference voice coil used here has a strain of 48%.

Velocity: Maximum velocities of DE actuators (for the size tested) are three orders of magnitude lower than voice coils velocities: 2-4 mm/s vs. 5000 mm/s.

Force-to-weight: DE actuators exhibit high forces relative to their active film weight, up to 500:1. When accounting for the weight of a complete 3 layers 107 mm actuator such as presented in Table 1, this number goes down to about 20:1. The reference voice coil has a similar force-to-weight of 13:1.

Specific work output: Specific work output on a film basis is about 0.1 J/g and drops to 0.003 J/g when based on a complete 3 layers 107 mm actuator. The voice coil has a similar value of 0.0064 J/g.

Power density: The power per unit film mass of DE actuators is 0.01 W/g. This value is reduced to 0.0001 W/g when based on a complete 3 layers 107 mm actuator. Such values are three orders of magnitude lower than the 0.16 W/g of voice coils.

Efficiency: DE actuator leak considerable electrical charge, leading to peak efficiencies of about 12% compared to 80% for voice coils.

In brief, DE actuators have higher linear strains than voice coils based motion systems and are much cheaper to use. Both actuators can provide similar force and work output for a given mass. Voice coils can operate 1000X faster, leading to much higher power capabilities.

5.2.2 Physical Mechanisms

The comparison with voice coils is extended to fundamental transducer mechanisms by comparing steady state energy flows, see Figure 62. From an effort/flow perspective, DE actuators are transformers while voice coils are gyrators [8], since:

- Application of a voltage to a DE actuator yields a force: $V \rightarrow F$, effort→effort.
- Application of a current to a voice coil yields a force: $i \rightarrow F$, flow→effort.

Both transducers yield their maximum effort at zero velocity and see their effort reduced with speed, since:

- As the velocity of a voice coil increases, the back electromotive voltage increase, $\dot{y} \rightarrow V_{EMF}$, to reduce the output force.
- As the velocity of a DE actuator increases, the viscous forces within the film increase, $\dot{y} \rightarrow F_{VIS}$, to reduce the actuator's force.

From a thermodynamic perspective, the two transducers are quite different: voice coils show small energy accumulation and small energy losses while, in contrast, DE actuators accumulate energy and show dominant leakage-driven energy losses.

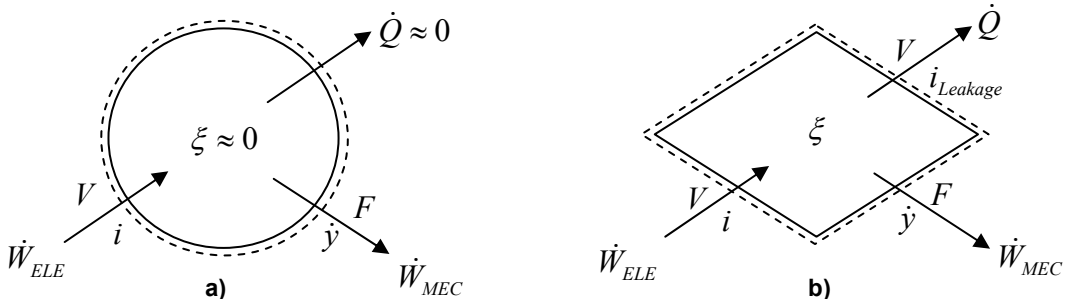

Figure 62: Steady state transducer systems: (a) voice coil, (b) DE actuator.

5.3 Design Trade-Off

An important issue of DE actuator design is the trade-offs between reliability and performance. Moreover, performance metrics must often be balanced between themselves (force, power, work output, efficiency). DE actuator reliability/performance information is summarized on the two design maps shown in Figure 63(a) and (b). In order to make this information more general for its possible use on other actuator designs, the maps are presented in terms of size-independent actuator stretch and stretch rate given by:

$$\lambda = \frac{y}{y_0}$$
$$\dot{\lambda} = \frac{\dot{y}}{y_0} \tag{5.1}$$

where, in the case of diamond actuator, the dimension y refers to the diamond minor axis length. It should be noted that the maps of Figure 63 are valid for DE actuators similar to the diamond actuators described in Chapter 2 and extrapolation to other designs should be done with care.

Figure 63(a) shows the usable design domain bounded by: viscoelasticity, dielectric strength and pull-in failures. According to Figure 61, pull-in limits the extension to very small stretches of about 1.3 at low velocities. From Figure 60, dielectric strength failure of loaded actuators operating at high stretch rate occurs at stretches of about 2.8. Figure 63(a) shows a frontier between regions of good and bad efficiencies arbitrarily based on a threshold of 1%. As shown in Chapter 3, the poor efficiency region is caused by current leakage through the film. Figure 63(b) shows performance metric peaks along with a typical design point for diamond actuators. This

particular point is selected for its good balance between all metrics. Peak force and power are constant across the stretch range as demonstrated in Chapter 3 (see Figure 28 and Figure 29 on pages 58 and 59).

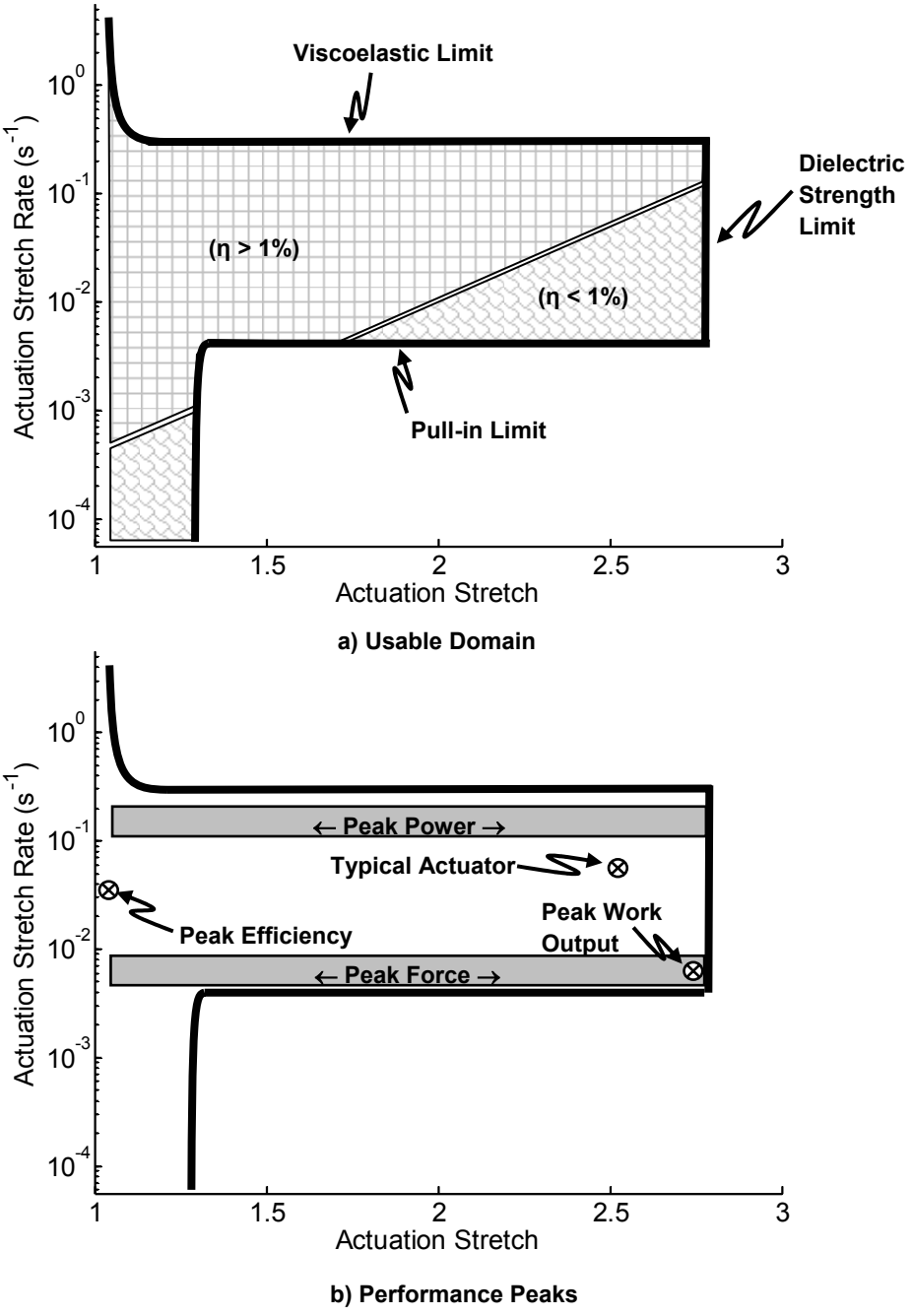

Figure 63: DE actuator design domain map.

The most important performance and reliability trade-offs occur with the peak force/work output:

1. Figure 63(b) shows peak force/work output to lie on the pull-in failure boundary. Peak force is obtained at low speed where viscoelastic forces are low. However, those same viscous forces also protect the film from pull-in failure. Unfortunately, pull-in is not a well defined failure mode and its boundary location is likely to be highly variable. A safety margin should be kept in selecting working conditions in the pull-in neighborhood. Peak force/work output cannot be obtained without sacrificing reliability.
2. Figure 63(a) and (b) show peak force/work output to be in the low efficiency domain. Peak force/work output cannot be obtained with good efficiency.
3. Figure 63(b) shows peak force/work output to be quite far from peak power. High forces are obtained at the smallest velocities whereas high powers occur at substantial velocities where significant mechanical energy is converted per unit time. Peak force/work output contradicts high power.
4. Peak force/work output occurs at very small velocities which are simply not practical for most applications.

In summary, selecting a good set of working conditions for DE actuators imply major trade-offs principally governed by viscoelasticity and current leakage.

5.4 Performance Scaling Laws

A fundamental design problem of any technology is to predict how performance changes with size, especially when many modern applications require small devices size. This section develops basic scaling laws for diamond shaped actuators in terms of film thickness, u, diamond side length, l, and number of layers, n, (see Figure 15 on page 39). The scaling laws are developed between two actuator configurations labeled by the subscripts A and B. The scaling laws are then verified on the two diamond actuators described in Chapter 2.

5.4.1 Stretch

In Appendix A it is shown that the film stretches depend only on the diamond angle, a size invariant quantity. Actuator stretch, λ, is equal to the film stretch in the y direction and is thus size invariant:

$$\frac{\lambda_B}{\lambda_A} = 1 \tag{5.2}$$

The same can be said about the strains from the definition: $\varepsilon = \lambda - 1$:

$$\frac{\varepsilon_B}{\varepsilon_A} = 1 \tag{5.3}$$

5.4.2 Stretch Rate and Velocity

Dividing an actuator's output stretch rate, $\dot{\lambda}$, as defined by Eq. (5.1) by itself between two configurations leads to:

$$\frac{\dot{\lambda}_B}{\dot{\lambda}_A} = \frac{\dot{y}_B}{\dot{y}_A}\frac{y_{0A}}{y_{0B}} \tag{5.4}$$

The initial output position, y_0, is proportional to actuator side length, l, and Eq. (5.4) is written as:

$$\frac{\dot{\lambda}_B}{\dot{\lambda}_A} = \frac{\dot{y}_B}{\dot{y}_A}\frac{l_A}{l_B} \tag{5.5}$$

In Chapter 3 it was shown how viscous forces govern actuator behavior. Viscous forces depend primarily on stretch rate, not on absolute velocity. Actuator stretch rate should therefore be matched to assure similarity at all scales: $\dot{\lambda}_A = \dot{\lambda}_B$. Equation (5.5) then leads to the result that, for constant stretch rates, velocity must vary with size:

$$\frac{\dot{y}_B}{\dot{y}_A} = \frac{l_B}{l_A} \tag{5.6}$$

Equation (5.6) shows that, as size goes down, $l_B << l_A$, velocity goes down, $\dot{y}_B << \dot{y}_A$. Hence, at small scales, velocity is reduced proportionally to size, making high speed/small scale applications impractical.

5.4.3 Force

A force scaling law is developed from the total actuator force given in terms of components contribution in Eq. (3.4). This equation is modified to include the contribution of the restoring force, F_R, of the elastic bands (see Figure 9):

$$F = F_S + F_I + F_F + F_R + F_M \tag{5.7}$$

To a first order approximation, the restoring force is assumed to perfectly balance the frames and film forces: $F_R = -\left(F_S + F_I + F_F\right)$. Equation (5.7) therefore reduces to:

$$F = F_M \tag{5.8}$$

The Maxwell force is readily given by Eq. (3.13) on page 69. This equation is substituted for the Maxwell pressure of Eq. (1.1) on page 19 and rewritten by lumping the size-invariant terms together $f(\varepsilon, \varepsilon_0, \theta)$:

$$F = F_M = \frac{l}{u} V^2 f(\varepsilon, \varepsilon_0, \theta) \tag{5.9}$$

Equation (5.9), when divided by itself between two configurations, leads to a basic actuator force scaling law:

$$\frac{F_B}{F_A} = \left(\frac{V_B}{V_A}\right)^2 \left(\frac{l_B}{l_A}\right)\left(\frac{u_A}{u_B}\right) \tag{5.10}$$

Force scaling must account for the number of active elastomer layers, n, which linearly multiplies actuator force: $F_{n\,\text{layers}} = nF_{1\,\text{layer}}$. Equation (5.10) therefore becomes:

$$\frac{F_B}{F_A} = \left(\frac{V_B}{V_A}\right)^2 \left(\frac{l_B}{l_A}\right)\left(\frac{u_A}{u_B}\right)\left(\frac{n_B}{n_A}\right) \tag{5.11}$$

Equation (5.11) is incomplete because it does not consider the active failure mode at high stretch rates: dielectric strength (Chapter 4). Thus, the voltages in Eq. (5.11) are written as fractions, χ, of the dielectric strength, $E_{\max}$: $V = u(\chi E_{\max})$:

$$\frac{F_B}{F_A} = \left(\frac{u_B \chi_B E_{\max}}{u_A \chi_A E_{\max}}\right)^2 \left(\frac{l_B}{l_A}\right)\left(\frac{u_A}{u_B}\right)\left(\frac{n_B}{n_A}\right) \tag{5.12}$$

Assuming identical dielectric strengths and loading fractions at all scales, Eq. (5.12) finally becomes:

$$\frac{F_B}{F_A} = \left(\frac{l_B}{l_A}\right)\left(\frac{u_B}{u_A}\right)\left(\frac{n_B}{n_A}\right) \tag{5.13}$$

The force per unit film mass, $f_f = \frac{F}{n\upsilon\rho}$ with υ the film volume and ρ the film density, scales by:

$$\frac{f_{f,B}}{f_{f,A}} = \left(\frac{l_A}{l_B}\right) \tag{5.14}$$

Thus it can be concluded that:

- everything else being constant, reducing the actuator planar dimensions, l, by 2 will reduce the force by a factor of 2.
- everything else being constant, reducing the actuator planar dimensions, l, and the film thickness, t, by 2 will reduce the force by a factor of 4.
- everything else being constant, reducing the actuator planar dimensions, l, by 2 will increase the force per unit film mass by a factor of 2.

5.4.4 Work Output

The work cycle experiments of Section 3.2.2 showed that DE actuators have a relatively constant force difference across their stroke when operated at constant stretch

rate. In first approximation, the work output is thus simply the product of actuator output force by the stroke:

$$W = Fs \tag{5.15}$$

Dividing Eq. (5.15) by itself between two configurations and using the fact that the stroke is proportional to actuator side length, l, gives an actuator work output scaling law:

$$\frac{W_B}{W_A} = \left(\frac{l_B}{l_A}\right)^2 \left(\frac{u_B}{u_A}\right)\left(\frac{n_B}{n_A}\right) \tag{5.16}$$

The specific work output per unit film mass, $w_f = \frac{W}{n\upsilon\rho}$ with υ the film volume and ρ the film density, scales by:

$$\frac{w_{f,B}}{w_{f,A}} = 1 \tag{5.17}$$

Thus it can be concluded that:

- everything else being constant, reducing the actuator planar dimensions, l, by 2 will reduce the work output by 4.
- everything else being constant, reducing the actuator planar dimensions, l, and the film thickness, u, by 2 will reduce the work output by 8.
- the specific work output per unit film mass of diamond shaped DE actuators is constant.

5.4.5 Verification

The scaling laws developed above were tested on the two diamond actuators of Chapter 2. These actuators intentionally represent a scaled-down case by a factor of two, from a 107 mm actuator (configuration A) to a 54 mm actuator (configuration B), see Figure 64. The force output was kept constant by doubling the number of layers. The relevant geometric ratios between the two designs are:

$$\frac{l_B}{l_A} = 0.5 \qquad \frac{u_B}{u_A} = 1 \qquad \frac{n_B}{n_A} = 2 \tag{5.18}$$

The ratios of Eq. (5.18) were inserted in the scaling rules defined above and the predicted performance ratios are compared with the measured values of Table 1 and Table 2 on page 33. The comparison depend highly on the measured forces but to first order, the force levels of the two actuators are about the same and thus, the results of Table 5 suggest the scaling rules to be valid.

In summary, for basic scaling purposes, the scaling laws developed here should give proper order-of-magnitude estimates. More work is needed to completely assess the question of downsizing DE actuators at very small scales (i.e. MEMS size).

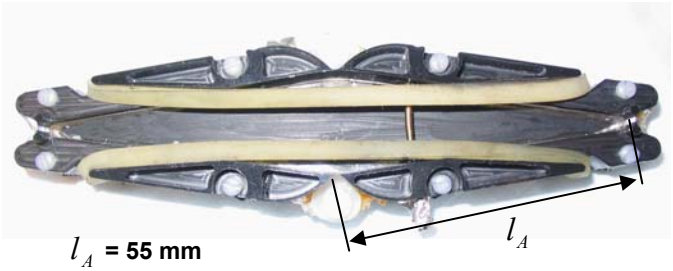

l_A = 55 mm
u_A = 1.5 mm
n_A = 3 layers

a) 107 mm Actuator

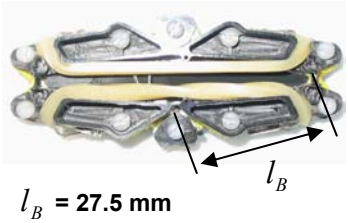

l_B = 27.5 mm
u_B = 1.5 mm
n_B = 6 layers

b) 54 mm Actuator

Figure 64: Diamond actuator scaling: 107 mm vs. 54 mm

Table 5: Scaling laws verification.

Scaling Laws	Eqs.#	Predictions	Measurements
$\frac{\lambda_B}{\lambda_A}$	(5.2)	1	1
$\frac{\dot{y}_B}{\dot{y}_A}$	(5.6)	0.5	0.5
$\frac{F_B}{F_A}$	(5.13)	1	0.91
$\frac{f_{f,B}}{f_{f,A}}$	(5.14)	2	1.77
$\frac{W_B}{W_A}$	(5.16)	0.5	0.45
$\frac{w_{f,B}}{w_{f,A}}$	(5.17)	1	0.88

5.5 Design Optimization

The two diamond actuators described in Chapter 2 have poor mass-specific performance characteristics compared to film-based values. For example, the specific work output of complete diamond actuators is about 0.003 J/g when the specific work output per unit film mass is 33 times higher at 0.1 J/g. Such characteristics can be improved by optimizing actuator designs quality. This section develops a quantitative metric of design quality.

The proposed metric is the ratio of the active mass to the total mass and is called structural efficiency:

$$\eta_s = \frac{m_f}{m_t} \tag{5.20}$$

The structural efficiency links film-based performance metrics to actuator-based ones. For example, the specific work output w is the product of the structural efficiency and the specific work output per unit film mass w_f:

$$w = \eta_s w_f \tag{5.20}$$

The specific work output per unit film mass, w_f, is particularly convenient for design optimization because it is constant for a given actuator geometry, pre-stretch and actuation stretch, see Eq. (5.17).

The structural efficiency of diamond actuators can be written as:

$$\eta_s = \frac{\overline{m}_f}{\overline{m}_f + \overline{m}_s + \overline{m}_i + \overline{m}_e + \overline{m}_h} \tag{5.21}$$

where the denominator is the sum of the component masses on a per-layer basis including the film, structural frames, interstitial frames, elastic bands and hardware. As a first approximation, the per-layer components masses ($\overline{m}_f, \overline{m}_s, \overline{m}_i, \overline{m}_e, \overline{m}_h$) do not vary significantly with the number of layers making the structural efficiency a constant for a given structure design.

From the data of Table 1 and Table 2 on page 33, the specific work output per unit film mass of diamond actuators operating at stretches of 2.5 is about 0.1 J/g. The structural efficiency of current diamond actuators is about 2.4%. A hypothetical actuator system made only from active polymer film and elastic bands (i.e. no frames, and thus, no dead mass) gives a structural efficiency of 12%. Such a low value indicates that the elastic bands are quite heavy relative to the polymer films. The effect of structural

efficiency on specific work output of current diamond actuators is illustrated on Figure 65.

In summary, the structural efficiency indicates the level of structural optimization of DE actuators. Actual designs, with their structural efficiency of 2.4%, could be improved by reducing the frames' mass and revising the restoring force system to incorporate higher energy storage materials. Structural efficiencies of about 10-20% seem possible.

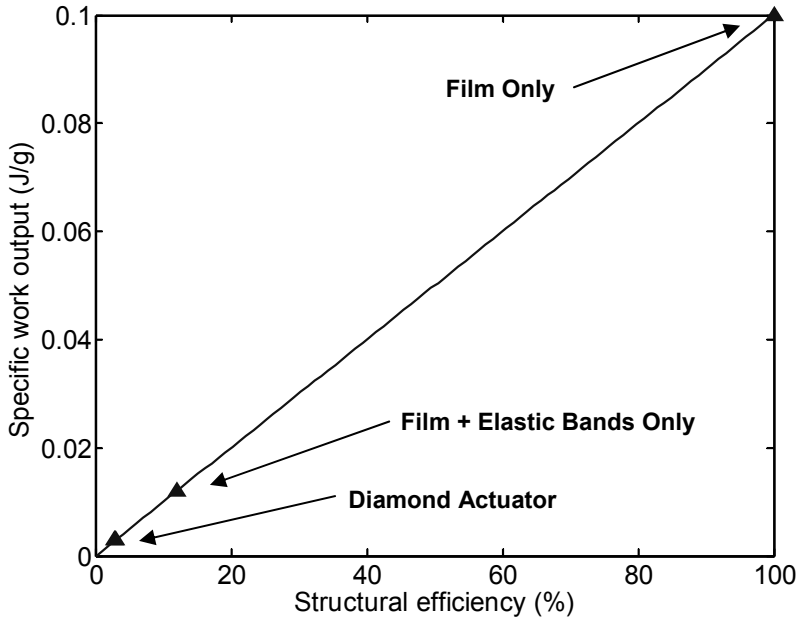

Figure 65: Effect of structural efficiency on specific work output.

5.6 Film Thickness Selection

DE actuators can use many thin layers or few thick ones to yield the same active film mass. Ideal film thickness depends on application and this section presents guidelines to help the selection process.

5.6.1 Advantages of Thin Films

1) The electromechanical coupling of DE actuation, Eq. (1.1), dictates that thin films use lower voltages. Lower voltages may be preferred for safety reasons when human interaction is involved, and to prevent current losses to the environment.

2) Thin films have lower pre-stretch forces, so the bonding area with the interstitial frames can be made smaller, potentially resulting in mass savings.

5.6.2 Advantages of Thick Films

1) For same active film mass, thick films use less active layers and are thus less sensitive to manufacturing defects. Consider a probabilistic event, G, consisting of manufacturing a defect-free active layer. This event is assumed independent from one layer to the next and its probability is $P(G)$. The probability of assembling a multi-layer actuator containing only defect-free layers is $\{P(G)\}^n$, where n is the number of layers. The number of layers has thus a strong impact on multi-layer actuator reliability, giving a net advantage to thick films over thin films.

2) Thick films are more efficient because they have lower current leakage than thin films under equal electric fields. This characteristic is a direct consequence of the diffusive current leakage described in Section 3.4.1. According to this model, thin films have a shorter diffusion length which significantly increases diffusive leakage.

To prove this, two films of different thickness were mounted on a 107 mm diamond actuator and expanded under equal electric fields. If current leakage was solely caused by pure classical conduction, both films would leak identical currents under an equal electric field:

$$i = \frac{EA}{\varphi} \tag{5.22}$$

where E is the electric field, A is the film area and φ is the material resistivity. Experimental data is shown in Figure 66 and shows clearly that thinner films consume more current. For example, at a stroke of s=14 mm, the current consumption of thin films is about 5 times higher than for thick films. The experimental demonstration that, under identical electric fields, thin films consume more current prove the existence of a diffusive-like leakage mechanism such as described in Section 3.4.1.

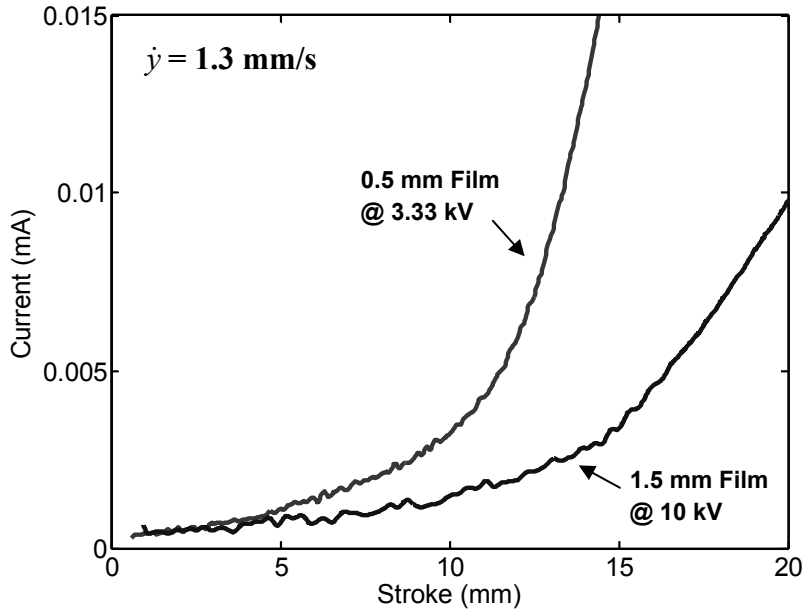

Figure 66: Effect of film thickness on current consumption.

The current consumption difference has a strong impact on efficiency. It can easily be shown that under constant electric field and output force, the electrical power consumption of an actuator regardless of its number of layers is proportional to its current. Hence, at a stroke of s=14 mm, the power consumption is also 5 times higher, and the efficiency is expected to be 5 times lower.

In summary, thin films use lower voltages and smaller, lighter frames. Thick films are less sensitive to manufacturing defects and are more efficient.

5.7 Film Edge Design

The principal failure mode encountered in practice is film edge cracking. This local failure mode is characterized by surface cracks forming at the film boundary with the interstitial frames as shown in the microscope photograph of Figure 67.

These cracks do not form immediately after actuator fabrication. They typically appear 1 week after the manufacturing date or after many cycles (1000+ cycles). The formation and propagation of these cracks is highly variable and is closely linked to actuator manufacturing details.

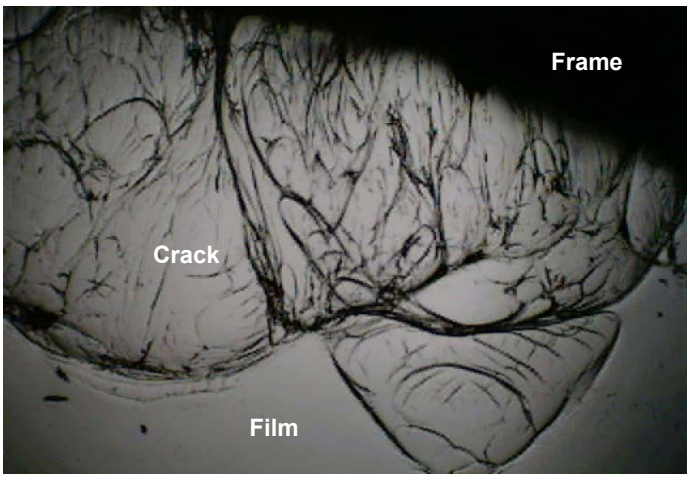

Figure 67: Film edge crack photograph (4X).

Figure 68 shows a diagram of the cracking problem along with the relevant design parameters. Cracks form at the inside frame corner and propagate toward the film center. When they reach the electrodes, the film thickness is locally reduced and voltage breakdown occurs.

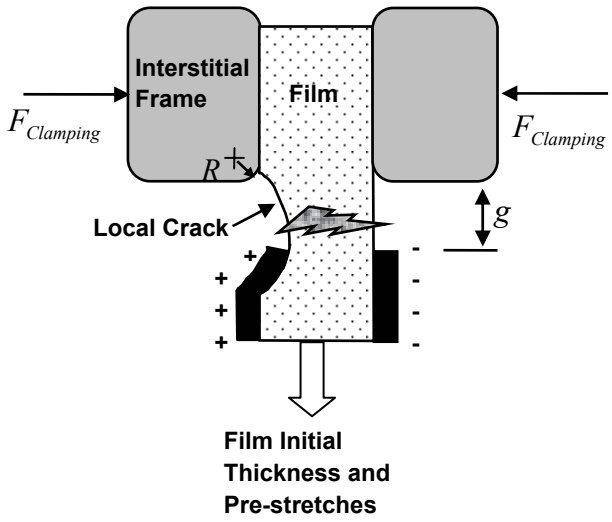

Figure 68: Film edge cracking mechanism.

The best design parameter values found in this thesis are given in Table 6 and explained below:

1. The film thickness and pre-stretches define the force that must be supported by the bond. The design strategy consists of using the thickest film that can be affixed to the frames with a minimum pre-stretch area expansion of 10 to insure reliable operation (see Chapter 4). The best combination found is a 1.5 mm thick film pre-stretched to 5x2.2 giving a pre-stretch area expansion of 11. Higher pre-stretch area expansions or film thickness yielded excessive cracking.
2. The interstitial frames use living hinges and must therefore be flexible and adhere well to the film. The best material (yet) found for these parts is nylon 6/6. Experiments were conducted with other thermoplastics, such as acetal, polyethylene, polypropylene, but these materials showed poor bonding strength. The surface should be as smooth as possible and cleaned with alcohol before bonding.

3. The clamping force, $F_{Clamping}$, exerted on the film should be maximized until the film flows out of the frame.
4. A small radius, R, should be added to the inside frame edge in contact with the film to relieve the local stress concentration.
5. One of the most important features is the small gap, g, between the electrode edge and the frame edge, see Figure 68. This gap decouples the mechanical stress concentration from the electric field. In this way, small cracks can be tolerated because they are not directly under the electrode and thus do not cause instant dielectric strength failure.

Table 6: Best film bonding interface parameters.

Parameters	Values
Film initial thickness and pre-stretches	U=1.5 mm
	$\lambda_{1,pre}$ x $\lambda_{2,pre}$ =5x2.2
Interstitial frame surface	Nylon 6/6, smoothest finish, ethanol washed
$F_{Clamping}$	Max. allowed
R	0.5 mm
g	1 mm

5.8 Chapter Summary

The design of DE actuators is a complex problem. The diamond actuator concept was presented along with its performance characteristics. Compared to voice coils, these actuators can be described as: high displacement, medium force, low velocity, low power, low efficiency. A set of design tools for DE actuators design were presented including performance numbers, design trade-off maps, scaling rules, a design optimization metric, film thickness selection guidelines and film edge design guidelines. The design experience of DE actuators is still limited and more work is needed to master all its subtleties.

CHAPTER

6

INTEGRATION TO BINARY ROBOTIC SYSTEMS

6.1 Introduction

Chapter 4 showed that fast, intermittent actuation is essential for reliable DE operation. Chapter 3 also supported this point by showing that DE actuators are inefficient at low velocities since they waste energy through leakage. This chapter now addresses the problem of using DE actuators in binary robotic systems while employing fast, intermittent actuation. The idea of using DE actuators in conjunction with bistable structures is explored. Two design concepts are presented along with an application example to intra-MRI manipulation.

6.2 Problem Definition

Two possible strategies are discussed for providing intermittent actuation: segmented actuation and bistable actuation. Segmented actuation employs a very large number of individual actuators, or cells, where each cell is alternatively actuated at high frequencies [18]. When a cell has been actuated for a long period of time, it is turned off to prevent failure.

The segmented actuation strategy is elegant theoretically but requires a very large number of independent actuator cells to work properly. For example, typical segmented binary devices could use ~10 multi-layered actuators, with ~100 layers each, requiring the control of 10x100=1000 individual layers. Such large numbers would lead to serious

practical problems related to wiring and switching. Interesting progress has been made at the control and hardware levels, but much more needs to be done before DE actuators can be used with this strategy [18,63]. Segmented actuation also requires constant power input to maintain extended states which, in the case of DE actuators, leads to low efficiency due to current leakage (see Chapter 3).

Bistable actuation consists of coupling DE actuators to bistable structures. Actuators are used to switch the states of bistable mechanism while applying an external load. In contrast with segmented actuation, bistable actuation is much easier to implement. Bistable mechanisms and structures are well known and existing devices using them already surround us (i.e. light switches and retractable ball point pens) [31,47]. Bistable binary devices do not require as many independent actuators, 10's to 100's being typical numbers [26,43,65]. Also, bistable actuation does not require a constant power input to maintain an activated state. Therefore, bistable actuation is the most practical solution to implement DE actuators in binary robotics.

6.3 Bistable Actuation Concepts

Two bistable actuator concepts using the diamond actuators developed in Chapter 5 are proposed: the flip-flop and the mini-might. Both are described in detail in the following sections.

6.3.1 Flip-Flop

The flip-flop strategy is the simplest possible way to achieve bistable actuation [80]. It consists of two actuators that toggle a bistable member, see Figure 69. The flip-flop strategy was conceptualized around the 107 mm diamond actuators of Chapter 2 and a solid model view is shown in Figure 70. The design of the buckling beams bistable

element was done by Matt Santer of Cambridge University, England[1] [65,68]. The final design consists of four High Density Polyethylene (HDPE) buckling members, each having a rectangular cross-section of depth 6.35 mm and thickness 2.3 mm, a distance between hinges of 60.6 mm and an initial curvature of 0.015 mm^{-1}.

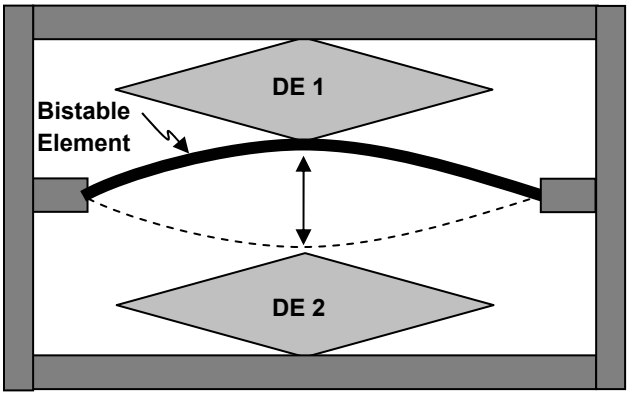

Figure 69: Flip-flop bistable mechanism.

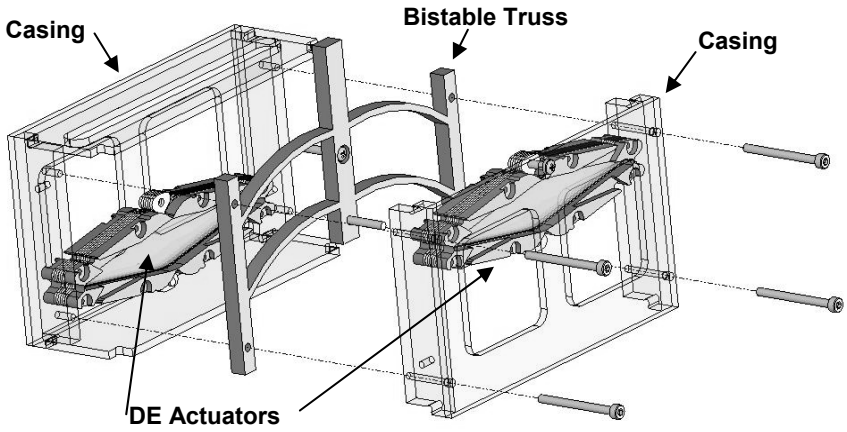

Figure 70: Flip-flop bistable actuator concept.

A prototype of the flip-flop bistable actuator is shown in Figure 71. Typical force/stroke profiles of the bistable truss with and without actuation are shown in Figure 72. The force spikes in Figure 72 at about 6 mm are due to friction in the mechanism.

[1] Under a joint research project sponsored by the Cambridge-MIT Institute.

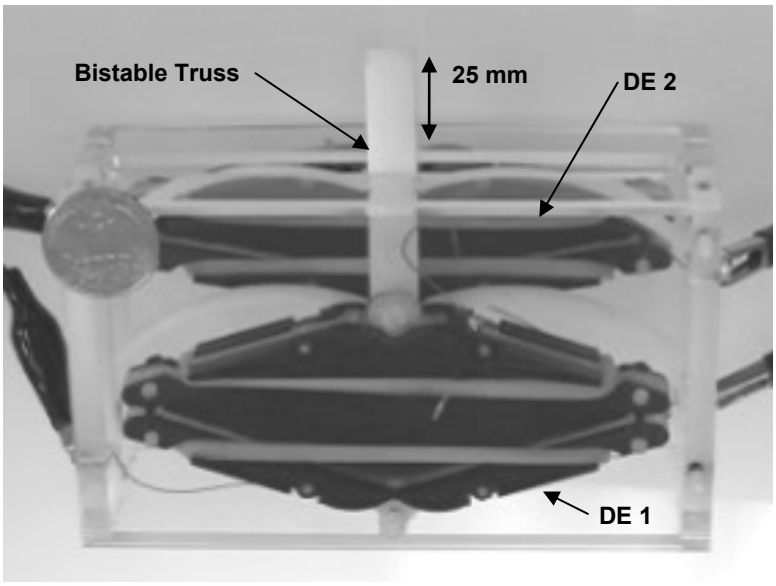

Figure 71: Flip-flop bistable actuator prototype.

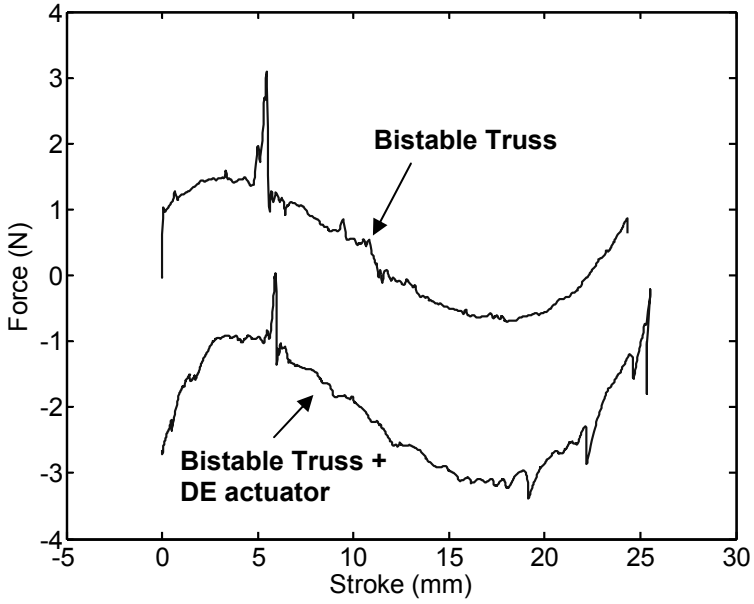

Figure 72: Flip-flop bistable actuator force profiles.

In Figure 72, the unstable point occurs at about 12 mm where the bistable truss force is zero. In the 0-12 mm range, the bistable truss pushes against the DE actuator while between the 12-24 mm range the bistable truss pushes with the DE actuator. As a consequence, the output force of the system varies from -1N to -3N or symmetrically

from +1N to +3N if tested in the other direction. The maximum external force that can be switched from one state to the next is thus ± 1N. 1N is about half the DE actuator average force of 2.1 N, (see Table 1 on page 33). This behavior is fundamental to bistable actuation where DE actuators must overcome two loads: the bistable truss load and the external load.

The specifications of the flip-flop prototype are summarized in Table 7. The prototype shows output strain of 30% despite the extra parts and volume needed for bistable action.

Table 7 shows that the main problem of this prototype is its heavy mass, leading to poor force-to-weight ratio and specific work output. With a force-to-weight ratio of 0.46 this prototype is not capable of supporting its own weight. It would therefore not be useful for binary robotics where many actuators must be integrated into a self-supporting structure. Nevertheless, the flip-flop prototype could still be used for applications not requiring self-supporting actuators, such as for example automotive door lock mechanisms.

Table 7: Flip-flop bistable actuator specifications.

Performance Metrics (@ 1.6 mm/s)	Values
Displacement	25 mm
Strain (based on 81mm length)	30%
Force (min/max)	1 – 3 N
Mass	220 grams
Force-to-weight	0.46
Specific work output	1.14×10^{-4} J/g
Switching time	~5 s
Size (closed)	135×81×48 mm

6.3.2 Mini-Might

The mini-might was developed with two objectives: (A) reduce the size of the flip-flop prototype by half while keeping the same output force, and (B) increase the force-to-weight ratio above 1.0. The mini-might uses a novel bi-stability approach that uses a single DE actuator. A compliant ratcheting mechanism is introduced between the bistable element and the DE actuator. The resulting system is much more compact and reduces system mass and wiring significantly. The major drawback of the mini-might is the added complexity of the compliant ratcheting mechanism.

The components of the mini-might are illustrated in Figure 73. The mini-might uses the 54 mm diamond actuator discussed in Chapter 2. Eight other parts complete the assembly: a backplate fitted with a pair of flexures at each end that connects with the 54 mm actuator structural frame; a compliant truss screwed to the backplate; a pair of compliant hooks press-fitted to the compliant truss; and finally, a pair of pins press fitted into the DE actuator structural frame.

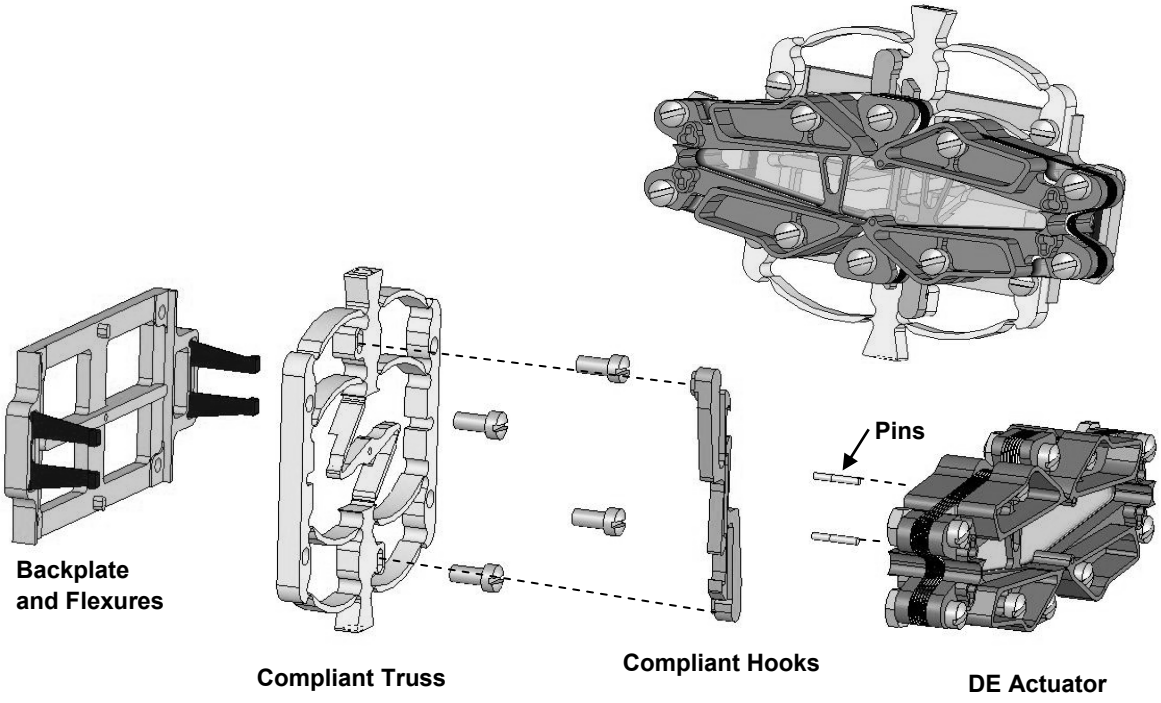

Figure 73: Mini-might concept, assembled and exploded views.

Outside dimensions of the mini-might system in the closed and opened states are shown in Figure 74. The figure shows the system's output points where the mini-might can be attached to an external system. The distance between these points changes from 35 to 47 mm between the closed and opened positions.

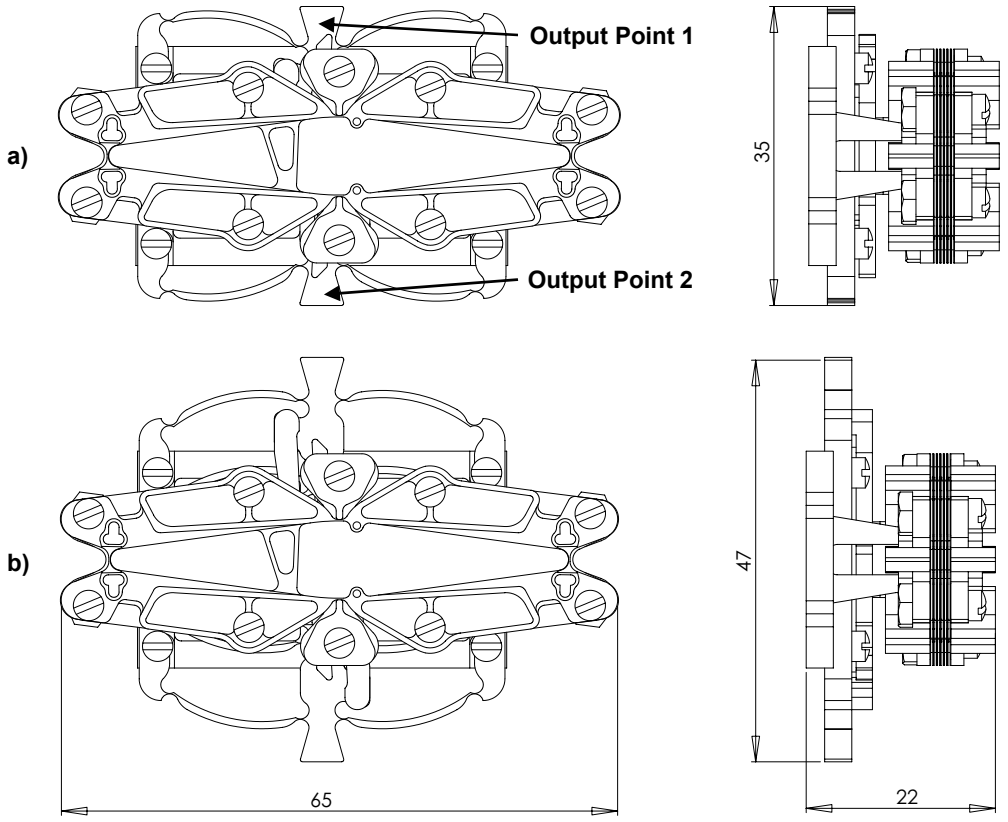

Figure 74: Mini-might dimensions in millimeters: (a) closed, (b) opened.

The key idea of the mini-might concept is that each time the actuator is fired, a different set of compliant hooks engages the actuator to alternatively open and close it. The principal component of the mini-might is its compliant truss, which contains one bistable truss for each output point, the two being connected by a compliant Watts linkage, see Figure 75. The Watts linkage insures that the motion of the two bistable elements is symmetric so that the system possesses only two states (instead of four).

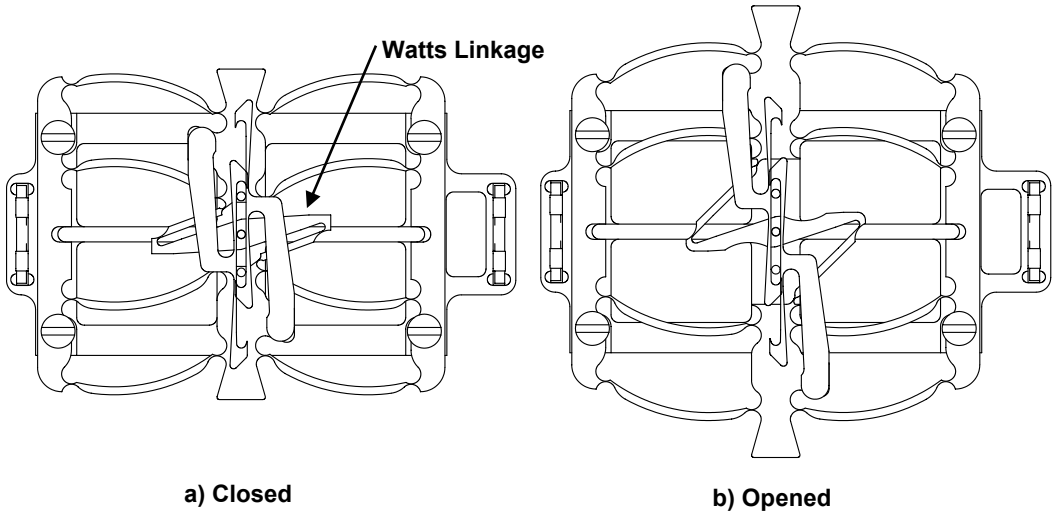

Figure 75: Mini-might mechanism details.

The bistable trusses were scaled down from the flip-flop unit and adapted from HDPE to acetal (Delrin), a polymer much less sensitive to creep. The final design consists of four buckling members, each having a rectangular cross-section of depth 3.18 mm and thickness 0.84 mm, a distance between hinges of 14.3 mm and a uniform initial curvature of 0.058 mm^{-1}.

The motion of the DE actuator pins, compliant hooks and system output points is illustrated schematically in Figure 76. The opening sequence of Figure 76 is as follows:

1. At the beginning of the cycle, the two output points are stable in the closed configuration. The DE actuator is closed.
2. Voltage is applied and the DE actuator opens, engaging the pins in the compliant hooks and moving the output points outward. At mid-stroke, the compliant hooks meet and the unengaged ones are deviated to the side. The system is at the unstable point.
3. Beyond the unstable position, the bistable truss force adds to the actuator force and the motion continues easily to the opened state.

4. Voltage is removed, the opened state is self-maintained and the DE actuator contracts back to its original position. The system is ready for the next cycle but this time the compliant hooks position is such that they will close the compliant truss, see Figure 75(b) and Figure 76.

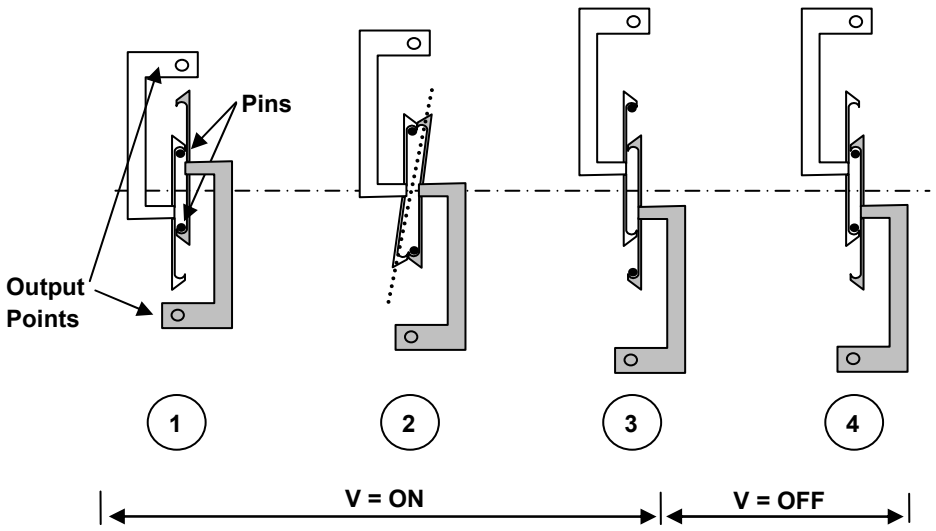

Figure 76: Mini-might opening sequence.

A prototype of the mini-might bistable actuator is shown in Figure 77. The 22 grams prototype is shown lifting a small DC motor of 25 grams over a vertical distance of 8 mm. This particular prototype is also equipped with compliant levers at each output point to illustrate how the force/stroke characteristics can be modified to match any desired requirements.

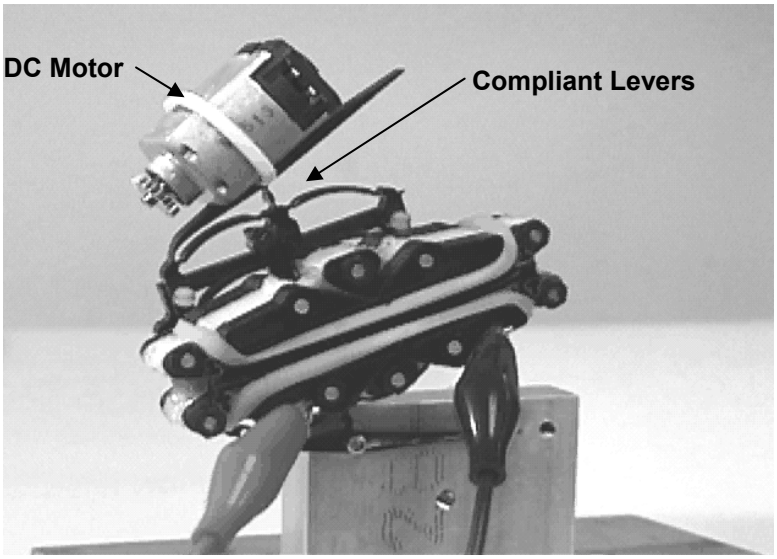

Figure 77: Mini-might bistable actuator prototype.

Typical force/stroke profiles of the compliant truss with and without actuation are shown in Figure 78. The curves are similar to the flip-flop curves of Figure 72, except that the stroke is reduced by 50%. The figure shows the small force perturbation caused by the deviation of the compliant hooks. Similarly to the flip-flop prototype, the lowest actuator output force is about ±1N.

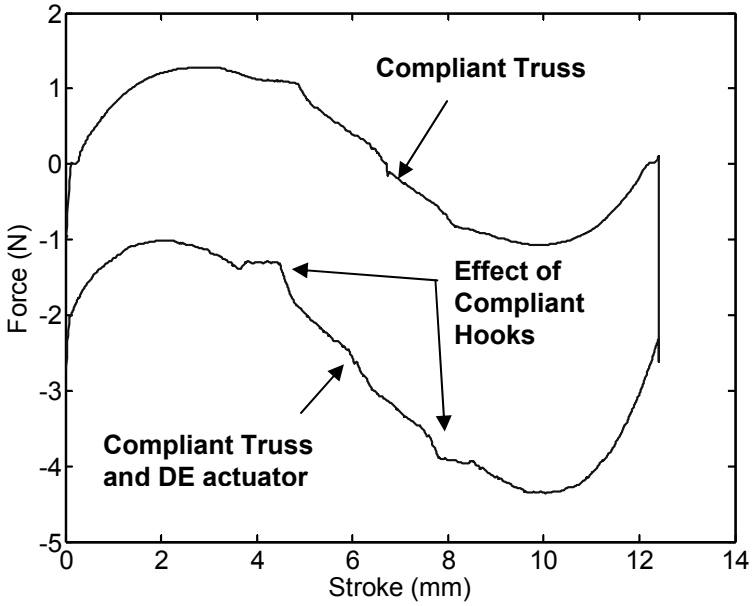

Figure 78: Mini-might bistable actuator force profiles.

The general specifications of the mini-might bistable actuator prototype are summarized in Table 8. Interestingly, the strain and force performance are nearly identical to the larger flip-flop prototype. The major differences with the flip-flop are the mass and volume, which are reduced by factors of 13 and 9 respectively. It should be noted that a scaled down flip-flop actuator would lead to mass and volume reduction factors of only 8 and 6. The mini-might is therefore 40% lighter and 33% smaller than a comparable flip-flop unit.

The mini-might's low mass gives better force-to-weight ratio and specific work output numbers compared to the flip-flop. However, these numbers are still relatively low and experience suggests that improvements of an order of magnitude would be necessary. The DE actuator represents 66% of the mini-might's mass and is the key component to improve.

Table 8: Mini-might bistable actuator specifications.

Performance Metrics (@ 0.8 mm/s)	Values
Displacement	13 mm
Strain (based on 35 mm length)	35%
Force (min/max)	1 – 3.5 N
Mass	16.4 grams
Force-to-weight	6
Specific work output	0.0015 J/g
Switching time	~5 s
Size (closed)	65×35×22 mm

6.4 Application to MRI Manipulation

The goal of this section is to illustrate the capabilities of bistable DE actuators on a typical binary robotics problem. This exercise will also reveal the questions that still need to be addressed. Another application example of DE actuators to binary robotics is given in Appendix F proposing a new planetary exploration mission concept using DE powered ball-robots.

The application considered here is the intra-MRI remote insertion of needles for transperinal biopsies and Brachytherapies of prostate cancer treatments. Current Brachytherapy treatments consists of injecting seeds of radioactive isotopes called Iodine^{125} in a tumorous prostate as shown in Figure 79. Needle insertion must be done with visualization tools like ultrasound and preferably MRI (due to better image quality) to guide the seeds on the tumorous regions. The radioactive seeds are manually injected one by one by using a perforated guide-plate as shown in Figure 80.

Robotics and mechatronics devices can help improve current MRI treatments, and especially Brachytherapies, by replacing manual operations, thereby decreasing treatment time, increasing accuracy and reducing costs. Robotics applications for intra-MRI interventions are not limited to cancer treatments. For example, MRI guided interventions on the endovascular system show great promises [4].

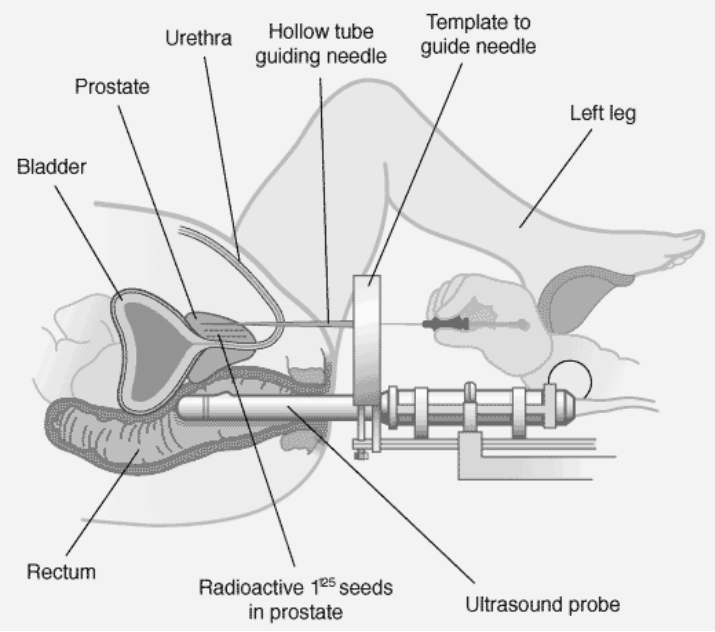

Figure 79: Transperinal Brachytherapy schematic[2].

[2] The Association of the British Pharmaceutical Industry. http://www.abpi.org.uk/

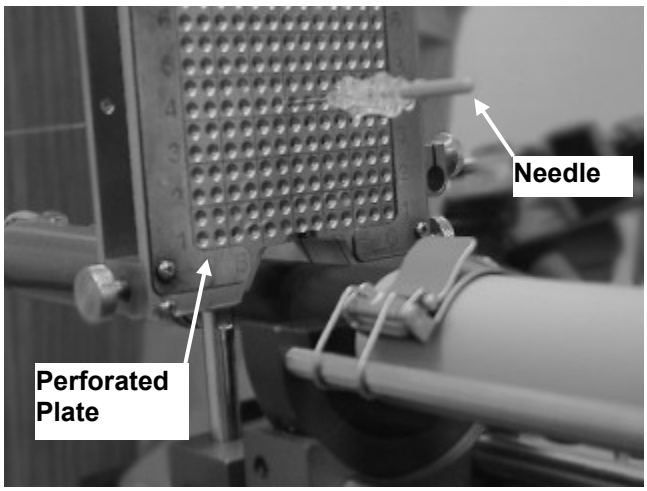

Figure 80: Perforated guide-plate for manual Brachytherapy[3].

The challenge of designing robotic systems for MRI manipulation is to operate without disturbing the high magnetic fields essential to imaging. Most classical robotic strategies cannot be used. Ferromagnetic materials like steel responds to magnetic fields. DC motors contain magnets and uses large currents that ruin image quality. One strategy is to use pneumatic or hydraulic systems where fluid lines allow the remote use of conventional pumps and flow control devices [78]. Ultrasound motors can be used with conventional robot architectures [29,41,52]. Such alternative systems are complex, expensive, cumbersome and prone to failure. These problems can potentially be alleviated by new paradigms like DE actuator based binary robotics. Moreover, DE actuation is MRI-compatible [79,80]. The low speeds of MRI manipulation matches well with the characteristics of DE actuators identified in Chapter 3.

6.4.1 System Requirements

The workspace requirements for MRI guided prostate needle insertion are shown in Figure 81. The schematic on the right shows the motion required for complete automated insertion. Referring to Figure 81, the manipulator concept developed in this

[3] Mechatronics in Medicine Laboratory, London, UK. http://www.imperial.ac.uk/mechatronicsinmedicine/

thesis is limited to the two planar directions of 80x80mm and the two angular orientation angles of ±15°. The resolution is set to 2mm and 2°, a significant improvement compared to the ~ 5mm and no angle of manual perforated guide-plates such as shown in Figure 80. The force requirements are to withstand a 10 N force in any direction at the needle tip. The available space is limited to the space between the legs of the patient as shown in Figure 81.

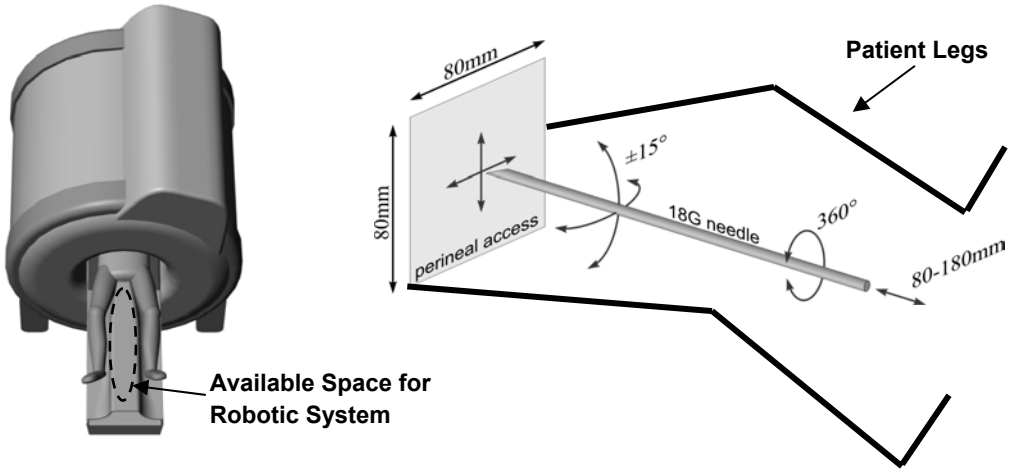

Figure 81: Workspace for needle insertion in transperinal prostate cancer treatment. (Courtesy of Daniel Katcher, Brigham and Women Hospital).

6.4.2 Proposed Design

The selected strategy is to develop a binary snake robot using the mini-might bistable actuators of Section 6.3.2. Snake motion has the advantage of naturally matching the smooth bends of the long needles used in those treatments. For simplicity reasons, the binary snake example developed here uses a kinematically constrained architecture, see Section 1.2.1.

Snake-like robots are well known in the field of robotics [27,50,54] and more specifically of binary robotics [15,82]. Here the snake kinematical architecture is based on the crane truss structure. This geometry was studied for binary robotics by Tyge

Schioler of Cambridge University, England[4]. The crane structure was selected because of its high strength-to-mass ratio and its potentially regular workspace distribution [69,70]. A basic un-actuated bistable crane structure was constructed by Schioler and is shown in Figure 82.

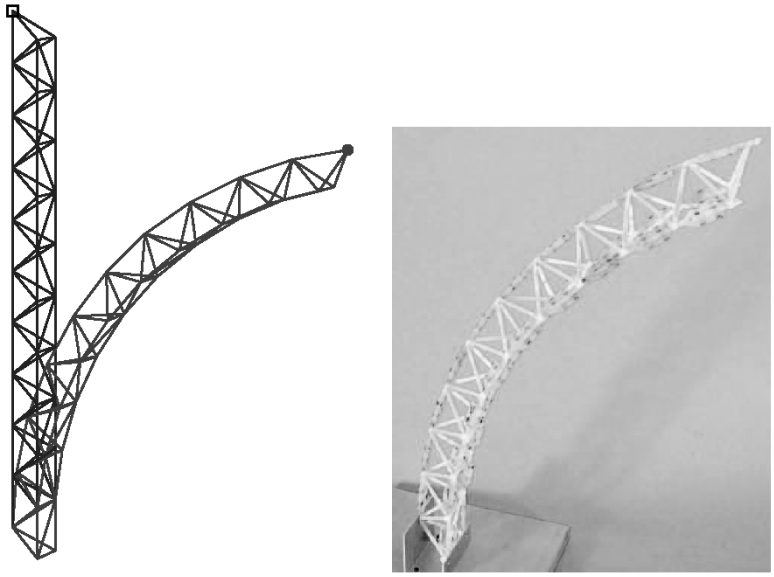

Figure 82: 30 DOF binary crane structure [70].

The crane structure was adapted to use the mini-might bistable actuators and the resulting snake-like binary robot is shown on Figure 83. The figure shows the snake robot positioned horizontally. The concept uses 24 identical actuators. The total system volume is 600x300x300 mm and fits easily between the patient's legs.

The major drawback of the snake concept is its cantilevered shape resulting in poor resistance to perturbation forces at the needle tip. A 10 N perturbation combined with gravity loading of a ~1.0 kg system would require a bistable actuator force at the snake base of about 100 N. Actual force capabilities are about 1 N, clearly too low to handle such loads. The number of active layers per actuator needs to increase drastically.

[4] Under a joint research project sponsored by the Cambridge-MIT Institute.

Another drawback of the snake concept is the large number of joints resulting in a complex assembly.

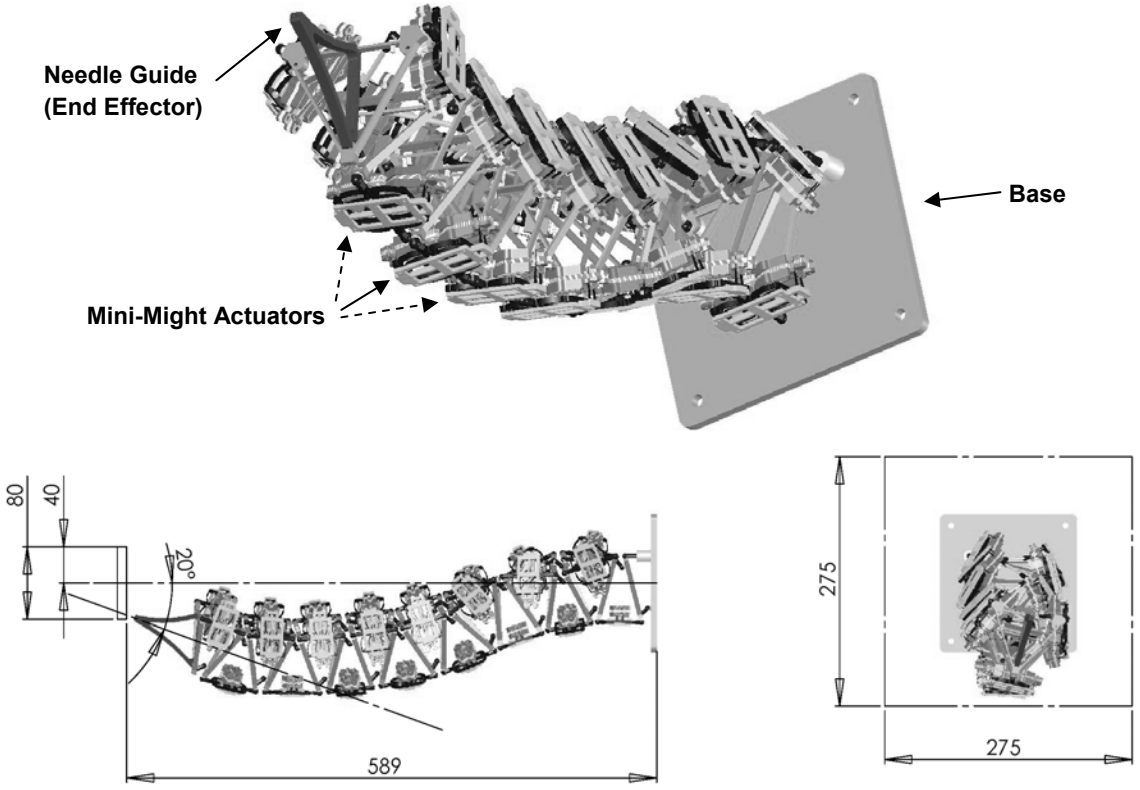

Figure 83: 24 DOF snake-like MRI manipulator concept (in millimeters).

The snake manipulator has 24 DOF giving 2^{24}=1.6x10^7 discrete positions which is assumed reasonable to cover the 3.6x10^5 positions of the workspace of Figure 81.

The manipulator workspace is evaluated by using homogenous transformations [73]. The workspace is illustrated by 1x10^5 randomly selected states in Figure 84, Figure 85 and Figure 86 showing respectively the end effector's x, y, z position, θ_x angle, and θ_y angle. The figures also show black squares representing the target zones. The points outside these regions are not specifically used for this MRI application. This inefficient situation is necessary to allow the manipulator to reach ±15^o even on the edge of the 80x80 mm grid as shown by the posture of Figure 83.

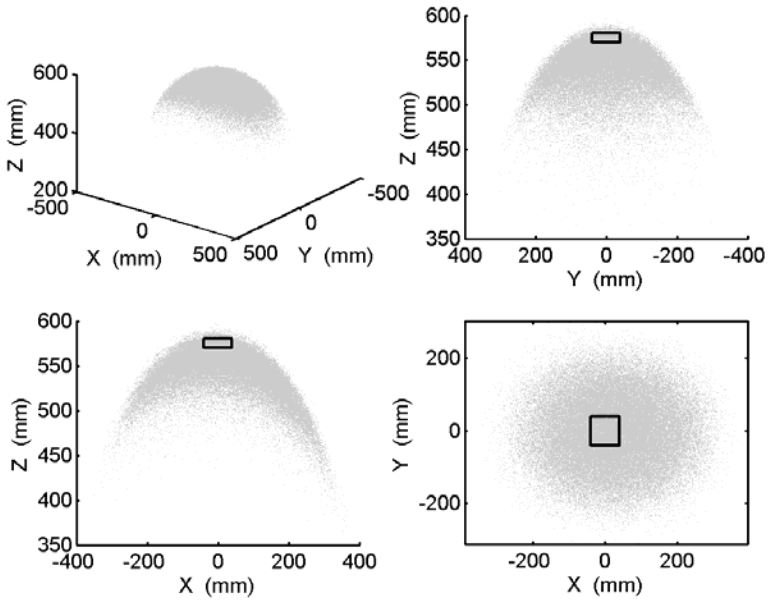

Figure 84: End effector's x, y, z position of the snake-like MRI manipulator.

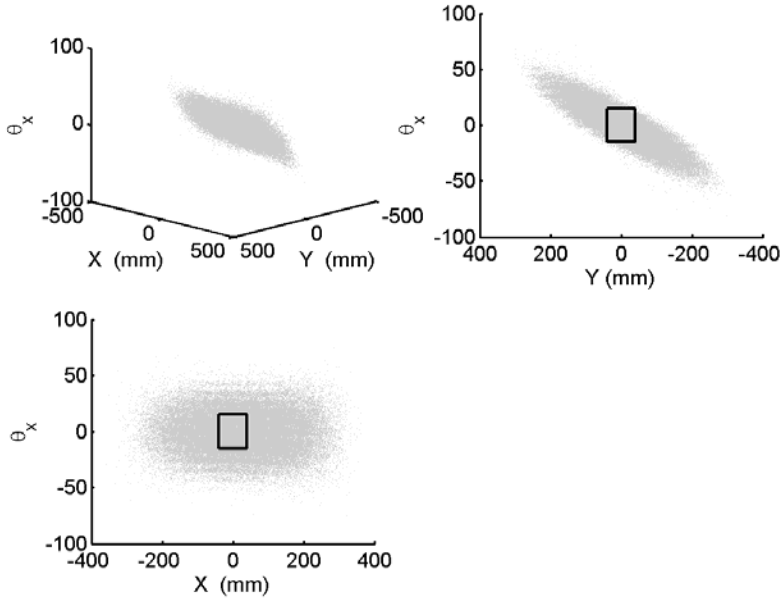

Figure 85: End effector's θ_x angle of the snake-like MRI manipulator.

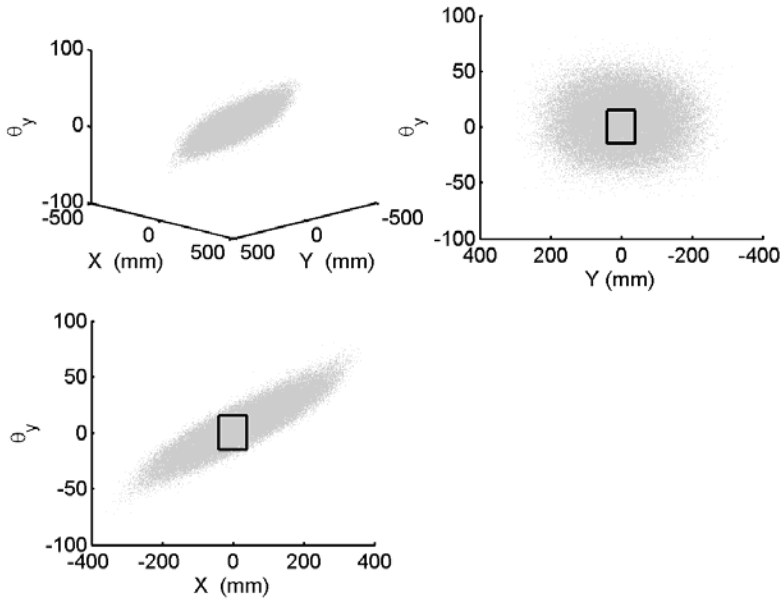

Figure 86: End effector's θ_y angle of the snake-like MRI manipulator.

6.4.3 7 DOF Prototype

A simplified binary-snake manipulator was constructed and is shown in Figure 87. This prototype showed how bistable DE actuators could eventually be used for binary robotics. As shown on Figure 88, the prototype exhibit large angular displacements of -35^o and +20^o at the tip. Such large displacements are a consequence of the large strains of DE actuators. The prototype weighs 173 grams and contains 7 DOF, each capable of forces of about 1N. This represents a net improvement compared to the first flip-flop prototype of Figure 71 that weighs 220 grams and contains only one DOF.

The design, fabrication, and operation of this prototype pointed out problems that still need to be addressed before binary devices become widely available. Those are:

1. The prototype has a very low stiffness. This is principally attributed to the low actuator forces resulting in poor contacts between the bistable trusses and their stops.

2. DE actuator forces are clearly too low for most manipulation tasks. This problem is not restricted to diamond actuators because the best spring roll actuators only show blocked forces (no speed) of 15 N [55]. In similar conditions, the 107 mm diamond actuators show 2 N per layer. Higher forces can be achieved by developing actuator designs and manufacturing processes that handle significantly more layers, on the order of 50 to 100.
3. DE actuators are too heavy for their forces, making binary systems highly sensitive to gravitational loading. New actuator designs improving structural efficiency (see Section 5.5) must be developed.
4. Actuator designs and manufacturing must be improved to increase actuator life by eliminating edge cracking (see Section 5.7) and increasing individual layer reliability.

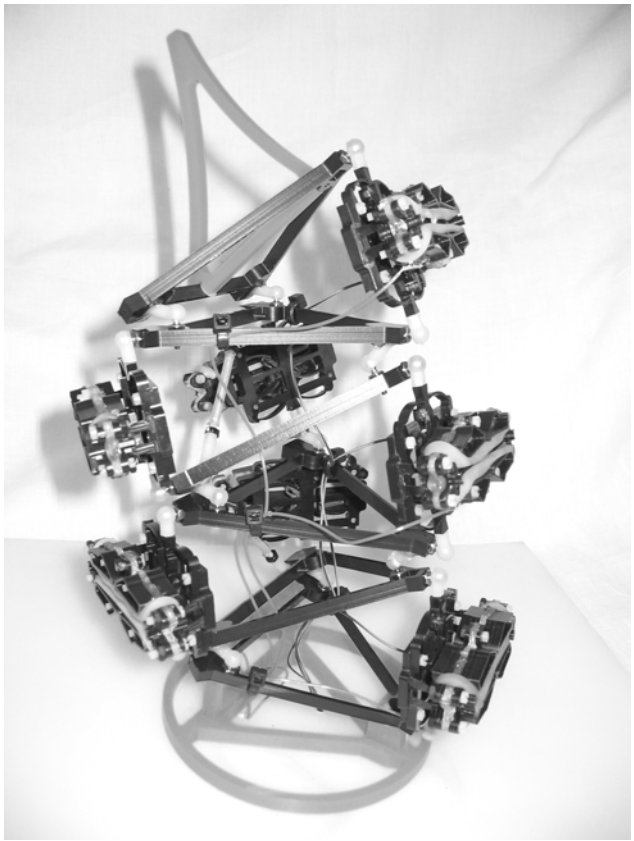

Figure 87: 7 DOF MRI manipulator prototype.

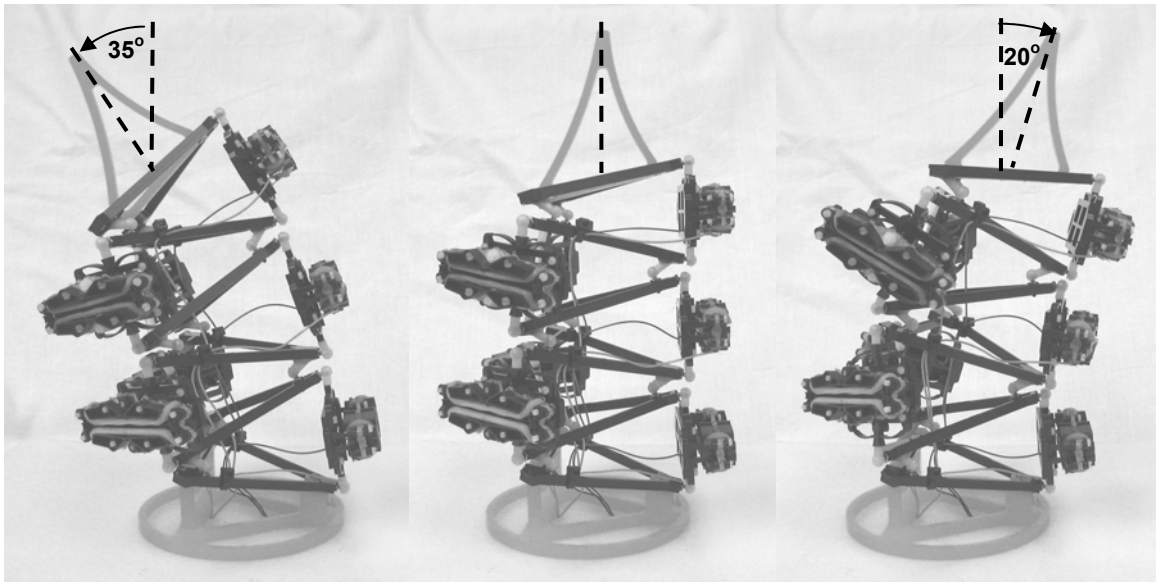

Figure 88: Range of motion of the 7 DOF MRI manipulator prototype.

6.5 Chapter Summary

This chapter coupled DE actuators to bistable structures to provide intermittent motion for binary robotic systems. Two configurations were presented: the flip-flop and the mini-might. These concepts are at opposite ends of the simplicity-performance axis. The flip-flop is simple and heavy while the mini-might is 40% lighter but complex.

An application example to MRI needle insertion was provided and a simple snake robot prototype was built. Bistable DE actuation was shown to be a valid approach to binary robotics, providing simple and low cost actuation to low power applications. However, the design of DE actuators needs to be improved in terms of actuator mass specific performance, actuator force output and shelf life.

CHAPTER

7

CONCLUSIONS

7.1 Contributions of this Thesis

This thesis developed fundamental models and design tools required to use DE actuators for binary robotics and mechatronics. The key contribution of this work is the result that DE actuators constructed from VHB 4905/4910 polymer or other highly viscoelastic materials must be used intermittently to be reliable. This result drastically changes the understanding of DE actuators and paves the way to bistable actuation.

Chapter 1 presented the motivation for this thesis. The progress of future robotic applications, like binary robotics, requires new high-performance actuators that are lightweight and low cost. DE actuation showed good potential but its progress was blocked by failures problems as well as unknown performance mechanisms.

Chapter 2 showed solution approaches that are common throughout this thesis. In particular, the diamond actuator concept used in most experiments of this thesis was presented. The continuum mechanics framework necessary to analyze DE actuators was also presented.

Chapter 3 presented a detailed experimental characterization of DE actuator performance. Observations showed that DE actuators develop good forces and strains at very low speeds. Their viscous nature drastically reduces their output force as speed increases, limiting DE actuator to low speed, low power applications. Current leakage allows significant amount of charge to dissipate, resulting in low efficiencies. The

viscoelasticity and current leakage mechanisms were investigated analytically. A detailed actuator mechanical model based on the Bergstrom-Boyce elastomer model was developed and showed good agreement with experimental results over three orders of magnitude of velocities and stretches of up to 5.0. A preliminary thermodynamic analysis of DE actuators identified diffusive current leakage as the dominant loss mechanism.

Chapter 4 addressed the most important road block of DE actuators: their poor reliability. Analytical models of a very simple DE expanding dot system were created including three postulated failure modes: material strength, dielectric strength and pull-in. The models were used to predict the maximum actuator expansion for a given film pre-stretch and stretch rate. The predictions were verified experimentally. At low speeds, pull-in dominates and at high speeds, dielectric strength dominates. Pull-in severely limits performance, making fast, intermittent action the only practical way to achieve reliable DE actuation.

Chapter 5 addressed the question of how to design DE actuators for reliable high performance application. DE Actuator design tools were presented in the form of: technical benchmark with voice coils, design trade-offs maps, scaling rules, a design optimization metric, film thickness selection guidelines and film edge design guidelines.

Finally, Chapter 6 showed how DE actuators can be integrated to binary robotic systems. The chapter explored the strategy of coupling DE actuators to bistable mechanisms to provide intermittent motion, an essential requirement for DE reliability. Two concepts were presented: the flip-flop is simple but heavy while the mini-might is lightweight but complex. An application example to MRI manipulation in the form of a binary snake robot was presented. It was shown that bistable DE actuation is a viable approach to binary robotics, but substantial improvements in actuator development are needed to make it practical for most applications.

7.2 Suggestions for Future Work

This thesis provided the essential science required to design reliable and high performance DE actuators for binary robotics. Four different suggestions for future work are made below.

First, DE actuator design and manufacturing must be significantly improved in the particular topics of mass specific performance, actuator force and shelf life. Those problems are not fundamental limitations of DE actuation and can be improved respectively by increasing DE actuator structural efficiency, increasing the number of active layers and optimizing the interstitial frames to eliminate edge cracking.

Second, developing proper elastomer materials for DE actuation presents a great opportunity to significantly improve their performance characteristics. The best known material to date is the VHB 4905/4910 adhesive from 3M, but it is not optimal. Ideal material properties have been proposed in Chapter 4.

Third, this thesis points out clearly that viscoelastic DE actuators are fundamentally low power devices (like most deformation based actuation technologies such as SMA, ionic polymers and piezoelectric materials). It will be essential at some point to develop radically different actuation technologies dedicated for high power binary robotics.

Fourth, the architectural question of how to place binary actuators together in order to achieve a given motion is still not well answered. Over-constrained systems should be investigated further. With such systems, actuator placement could be governed by structural stress lines, like animal bones and muscles.

REFERENCES

1 3M, "VHB Double Coated Acrylic Foam Tapes and Adhesives Transfer Tapes," 3M™ VHB.pdf, Technical Data, 2001.

2 Anand, L., "A Constitutive Model for Compressible Elastomeric Solids," *Computational Mechanics*, Vol. 18, pp. 339-355, 1996.

3 Anderson V. and R. Horn, "Tensor Arm Manipulator Design," ASME, 67-DE-57, 1967.

4 Bartels, L.W. and C.J.G. Bakker, "Endovascular interventional magnetic resonance imaging," Physics in Medicine and Biology, Vol. 48, No. 14, pp. R37-R64, 2003.

5 Bazergui, A., T. Bui-Quoc, A. Biron, G. McIntyre, and C. Laberge, *Resistance des materiaux*, 2nd Ed., Montréal: Éditions de l'École Polytechnique de Montréal, 1993.

6 Bergström, J. and M. Boyce, "Constitutive Modeling of the Large Strain Time-Dependant Behavior of Elastomers," *Journal of Mechanics and Physics of Solids*, Vol. 46, No. 5, pp. 931-954, 1998.

7 Bergström J. and M. Boyce, "Large Strain Time-Dependant Behavior of Filled Elastomers," *Mechanics of Materials*, Vol. 32, pp. 627-644, 2000.

8 Brown, F.B., *Engineering System Dynamics*, New York: Marcel Dekker, 2001.

9 Cameron, C., R. Underhill, M. Rawji, and J. Szabo, "Conductive Filler – Elastomer Composites for Maxwell Stress Actuator Applications," *Smart Structures and Materials 2004: Electroactive Polymer Actuators and Devices*, Yoseph Bar-Cohen, Editor, Proceedings of SPIE, San Diego, CA, Vol. 5385, pp. 51-59, 2004.

10 Carpi, F., P. Chiarelli, A. Mazzoldi, and D. De Rossi, "Electromechanical Characterization of Dielectric Elastomer Planar Actuators: Comparative Evaluation of Different Electrode Materials and Different Counterloads," *Materials Science and Engineering*, Vol. A 107, pp. 85-95, 2003.

11 Carpi, F., A. Mazzoldi, and D. De Rossi, "High-Strain Dielectric Elastomer for Actuation," *Smart Structures and Materials 2003: Electroactive Polymer Actuators and Devices*, Yoseph Bar-Cohen, Editor, Proceedings of SPIE, San Diego, CA, Vol. 5051, pp. 419-422, 2003.

12 Carpi, F., A. Migliore, and D. De Rossi, "A New Contractile Linear Actuator Made of Dielectric Elastomers," *Smart Structures and Materials 2005: Electroactive Polymer Actuators and Devices*, Yoseph Bar-Cohen, Editor, Proceedings of SPIE, San Diego, CA, Vol. 5759, pp. 64-74, 2005.

13 Carpi, F. and D. De Rossi, "Dielectric Elastomer Cylindrical Actuators: Electromechanical Modeling and Experimental Evaluation," *Materials Science and Engineering*, Vol. C 24, pp. 555-562, 2004.

14 Chirikjian, G. and J. Burdick, "Hyper-Redundant Robotic Mechanisms and Their Applications," *IEEE/RSJ International Workshop on Intelligent Robots and Systems IROS 91*, Osaka, Japan, pp. 185-190, 1991.

15 Chirikjian, G., J. Burdick, "Design and Experiments with a 30 DOF Robot," *Proceedings - IEEE International Conference on Robotics and Automation*, Atlanta, GA, Vol. 3, pp. 113-119, 1993.

16 Chirikjian, G., J. Burdick, "The Kinematics of Hyper-Redundant Robot Locomotion," *IEEE Transactions on Robotics and Automation*, Nagoya, Japan, Vol. 11, No. 6, pp. 781-793, 1995.

17 Chirikjian, G., "A Binary Paradigm for Robotic Manipulators," *Proceedings - IEEE International Conference on Robotics and Automation*, San Diego, CA, Vol. 4, pp. 3063-3069, 1994.

18 Cho, K.J., B. Selden, and H. Asada, "Segmented Binary Control of Multi-Axis SMA Array Actuators," *Smart Structures and Materials 2005: Modeling, Signal Processing, and Control*, Ralph C. Smith, Editor, Proceedings of SPIE, San Diego, CA, Vol. 5757, pp. 314-322, 2005.

19 Choi, H., K. Jung, N.H. Chuc, M. Jung, I. Koo, J. Koo, J. Lee, J. Lee, J. Nam, M. Cho, and Y. Lee, "Effects of Prestrain on Behavior of Dielectric Elastomer Actuator," *Smart Structures and Materials 2005: Electroactive Polymer Actuators and Devices*, Yoseph Bar-Cohen, Editor, Proceedings of SPIE, San Diego, CA, Vol. 5759, pp. 283-291, 2005.

20 Drozdov, A.D. and A. Dorfmann, "The nonlinear viscoelastic response of carbon black-filled natural rubbers," *International Journal of Solids and Structures,* Vol. 39, pp. 5699-5717, 2002.

21 Dubowsky, S., K. Iagnemma, S. Liberatore, D. Lambeth, J.S. Plante, and P. Boston, "A Concept Mission: Microbots for Large-Scale Planetary Surface and Subsurface Exploration," *Proceedings of the 2005 Space Technology and Applications International Forum (STAIF),* Albuquerque, NM, February 2005.

22 Erdman, A.G. and G.N. Sandor, *Mechanism Design Analysis and Synthesis, Volume I*, 3rd ed., Upper Saddle River, New Jersey: Prentice Hall, 1997.

23 Gardner, C., J. Jerome, and R. Eisenberg, "Electrodiffusion Model of Rectangular Current Pulses in Ionic Channels of Cellular Membranes," *Journal of Applied Mathematics*, Vol. 61, No. 3, pp. 792-802, 2000.

24 Goulbourne, N., M. Frecker, E. Mockensturm, and A. Snyder, "Modeling of a Dielectric Elastomer Diaphragm for a Prosthetic Blood Pump," *Smart Structures and Materials 2003: Electroactive Polymer Actuators and Devices*, Yoseph Bar-Cohen, Editor, Proceedings of SPIE, San Diego, CA, Vol. 5051, pp. 319-331, 2003.

25 Goulbourne, N., M. Frecker, and E. Mockensturm, "Electro-Elastic Modeling of a Dielectric Elastomer Diaphragm for a Prosthetic Blood Pump," *Smart Structures and Materials 2004: Electroactive Polymer Actuators and Devices*, Yoseph Bar-Cohen, Editor, Proceedings of SPIE, San Diego, CA, Vol. 5385, pp. 122-133, 2004.

26 Hafez, M., M. Lichter, and S. Dubowsky, "Optimized Binary Modular Reconfigurable Robotic Devices," *IEEE/ASME Transactions on Mechatronics*, Vol. 8, No. 1, pp. 18-26, March 2003.

27 Hannan, M.W. and I.D. Waker, "The Elephant Trunk Manipulator, Design and Implementation," *Proceedings of the IEEE/ASME International Conference on Advanced Intelligent Mechatronics Proceedings*, Como, Italy, Vol. 1, pp. 14-19, 2001.

28 Hanson, D. and V. White, "Converging the Capabilities of EAP Artifical Muscles and the Requirements of Bio-Inspired Robotics," *Smart Structures and Materials 2004: Electroactive Polymer Actuators and Devices*, Yoseph Bar-Cohen, Editor, Proceedings of SPIE, San Diego, CA, Vol. 5385, pp. 29-40, 2004.

29 Hata, N., F. Ohara, R. Hashimoto, M. Hashizume, and T. Dohi, "Needle Guiding Robot with Five-Bar Linkage for MR-Guided Thermotherapy of Liver Tumor," *Lecture Notes in Computer Science - Medical Image Computing and Computer-Assisted Intervention - MICCAI 2004 - 7th International Conference Proceedings*, Vol. 3217, pp. 161-168 2004.

30 Holzapfel, G.A., *Nonlinear Solid Mechanics*, Chichester, UK: John Wiley & Sons, 2000.

31 Jensen, B.D. and L.L. Howell, "Bistable Configurations of Compliant Mechanisms Modeled Using Four Links and Translational Joints," *Journal of Mechanical Design*, Vol. 126, pp. 657-666, July 2004.

32 Kofod G., "Dielectric Elastomer Actuators," Ph.D. Thesis, Department of Chemistry, The Technical University of Denmark, Denmark, September 2001.

33 Kofod G., R. Kornbluh, R. Pelrine, and P. Sommer-Larsen, "Actuation Response of Polyacrylate Dielectric Elastomers," *Smart Structures and Materials 2001: Electroactive Polymer Actuators and Devices*, Yoseph Bar-Cohen, Editor, Proceedings of SPIE, San Diego, CA, Vol. 4329, pp. 141-147, 2001.

34 Kornbluh R., R. Pelrine, Q. Pei, R. Heydt, S. Stanford, S. Oh, and J. Eckerle, "Electroelastomers: Applications of Dielectric Elastomer Transducers for Actuation, Generation and Smart Structures," *Smart Structures and Materials 2002: Electroactive Polymer Actuators and Devices*, Yoseph Bar-Cohen, Editor, Proceedings of SPIE, San Diego, CA, Vol. 4695, pp. 254-270, 2002.

35 Kornbluh R., R. Pelrine, Q. Pei, S. Oh, and J. Joseph, "Ultrahigh Strain Response of Field-Actuated Elastomeric Polymers," *Smart Structures and Materials 2000: Electroactive Polymer Actuators and Devices*, Yoseph Bar-Cohen, Editor, Proceedings of SPIE, San Diego, CA, Vol. 3987, pp. 51-64, 2000.

36 Kornbluh R., R. Pelrine, H. Prahlad, and R. Heydt, "Electroactive Polymers: An Emerging Technology for MEMS," *MEMS/MOEMS Components and Their Applications 2004*, Siegfried W. Janson, Editor, Proceedings of SPIE, San Jose, CA, Vol. 5344, pp. 13-27, 2004.

37 Kornbluh R., R. Pelrine, J. Joseph, R. Heydt, Q. Pei, and S. Chiba, "High-Field Electrostriction of Elastomeric Polymer Dielectrics for Actuation," *Smart Structures and Materials: Electro-Active Polymer Actuators and Devices*, Proceedings of SPIE, Newport Beach, CA, Vol. 3669, pp. 149-161, 1999.

38 Kornbluh R ., R. Pelrine, and J. Joseph, "Elastomeric Dielectric Artificial Muscle Actuators for Small Robots," *Proceedings of the Materials Research Society Symposium*, Vol. 600, pp. 119-130, 1995.

39 Ladeggard Larsen, A., P. Sommer-Larsen, and O. Hassager, "How to Tune Rubber Elasticity," *Smart Structures and Materials 2004: Electroactive Polymer Actuators and Devices*, Yoseph Bar-Cohen, Editor, Proceedings of SPIE, San Diego, CA, Vol. 5385, pp. 108-117, 2004.

40 Larsen, P., G. Kofod, M. Benslimane, P. Gravesen, and M.H. Shridhar, "Performance of Dielectric Elastomer Actuators and Materials," *Smart Structures and Materials 2002: Electroactive Polymer Actuators and Devices*, Yoseph Bar-Cohen, Editor, Proceedings of SPIE, San Diego, CA, Vol. 4695, pp. 158-166. 2002.

41 Larson, B.T., A.G. Erdman, N.V. Tsekos, E. Yacoub, P.V. Tsekos, and I.G. Koutlas, "Design of an MRI-Compatible Robotic Stereotactic Device for Minimally Invasive Interventions in the Breast," *Journal of Biomechanical Engineering*, Vol. 126, No. 4, pp. 458-465, August, 2004.

42 Lichter, M.D., V.A. Sujan, and S. Dubowsky, "Computational Issues in the Planning and Kinematics of Binary Robots," *Proceedings - IEEE International Conference on Robotics and Automation*, Washington, DC, Vol. 1, pp. 341-346, 2002.

43 Lichter, M.D., V.A. Sujan, and S. Dubowsky, "Experimental Demonstrations of a New Design Paradigm in Space Robotics," *Proceedings of the Seventh International Symposium on Experimental Robotics (ISER 00)*, Honolulu, HI, December 2000.

44 Lichter M., "Concept Development for Lightweight Binary-Actuated Robotic Devices with Applications to Space Systems," M.S. Thesis, Department of Mechanical Engineering, Massachusetts Institute of Technology, Cambridge, MA, 2001.

45 Lees, D. and G. Chirikjian, "A Combinatorial Approach to Trajectory Planning for Binary Manipulators," *Proceedings - IEEE International Conference on Robotics and Automation*, Minneapolis, MN, Vol. 2, pp. 1012-1017, 1996.

46 Ma, W. and L.E. Cross, "An Experimental Investigation of Electromechanical Response in a Dielectric Acrylic Elastomer," *Applied Physics - Materials Science & Processing*, Vol. A 78, pp. 1201-1204, 2004.

47 Masters, N.D. and L.L. Howell, "A Three Degree-of-Freedom Model for Self-Retracting Fully Compliant Bistable Micromechanisms," *Journal of Mechanical Design*, Vol. 127, pp. 739-744, July 2005.

48 McMeeking, R. and C. Landis, "Electrostatic Forces and Stored Energy for Deformable Dielectric Materials," *Journal of Applied Mechanics*, Vol. 72, No. 4, pp. 581-590, July 2005.

49 Meijer, K., M. Rosenthal and R.J. Full, "Muscle-Like Actuators? A Comparison Between Three Electroactive Polymers," *Smart Structures and Materials 2001: Electroactive Polymer Actuators and Devices*, Yoseph Bar-Cohen, Editor, Proceedings of SPIE, San Diego, CA, Vol. 4329, pp. 7-15, 2001.

50 Mizuuchi, I., S. Yoshida, M. Inaba, and H. Inoue, "The Development and Control of a Flexible-Spine for a Human-Form Robot," *Advanced Robotics*, Vol. 17, No. 2, pp. 179-196, 2003.

51 Murkherjee, S. and S. Murlidhar, "Massively Parallel Binary Manipulators," *Journal of Mechanical Design*, Vol. 123, No. 1, pp. 68-123, March 2001.

52 Naganou, H., H. Iseki, and K. Masamune, "MRI Compatible Modular Designed Robot for Interventional Navigation - Prototype Development and Evaluation," *Lecture Notes in Computer Science - Medical Image Computing and Computer-Assisted Intervention - MICCAI 2004 - 7th International Conference Proceedings*, Vol. 3217, pp. 1069-1070, 2004.

53 Ogden, R.W., *Non-Linear Elastic Deformations*, New York: Dover Publications, 1984.

54 Paljug, E., T. Ohm, and S. Hayati, "The JPL Serpentine Robot: a 12 DOF System for Inspection," *Proceedings - IEEE International Conference on Robotics and Automation*, Nagoya, Japan, Vol. 3, pp. 3143-3148, 1995.

55 Pei, Q., R. Pelrine, M. Rosenthal, S. Stanford, H. Prahlad, and R. Kornbluh, "Recent Progress on ElectroElastomer Artificial Muscles and their Application for Biomimetic Robots," *Smart Structures and Materials 2004: Electroactive Polymer Actuators and Devices*, Yoseph Bar-Cohen, Editor, Proceedings of SPIE, San Diego, CA, Vol. 5385, pp. 41-50, 2004.

56 Pei, Q., M. Rosenthal, R. Pelrine, S. Stanford, and R. Kornbluh, "Multifunctional Electroelastomer Roll Actuators and Their Application for Biomimetic Walking Robots," *Smart Structures and Materials 2003: Electroactive Polymer Actuators and Devices*, Yoseph Bar-Cohen, Editor, Proceedings of SPIE, San Diego, CA, Vol. 5051, pp. 41-50, 2003.

57 Pelrine R., R. Kornbluh, and J. Joseph, "Electrostriction of Polymer Dielectrics with Compliant Electrodes as Means of Actuations," *Sensor and Actuators A: Physical*, Vol. 64, pp. 77-85, 1998.

58 Pelrine R., R. Kornbluh, J. Joseph, and S. Chiba, "Electrostriction of Polymer Films for Microactuators," *Proceedings - IEEE Tenth Annual International Workshop on Micro Electro Mechanical Systems*, Nagoya, Japan, pp. 238-243, 1997.

59 Pelrine R., R. Kornbluh, J. Joseph, R. Heydt, Q. Pei, and S. Chiba, "High-Field Deformation of Elastomeric Dielectrics for Actuators," *Materials Science & Engineering C, Biomimetic and Supramolecular Systems*, Vol. 11, No. 2, pp. 89-100, 2000.

60 Pelrine R., R. Kornbluh, Q. Pei, and J. Joseph, "High Speed Electrically Actuated Elastomers with Stretch Greater Than 100%," *Science*, Vol. 287, No. 5454, pp. 836-839, 2000.

61 Pelrine R., R. Kornbluh, Q. Pei, S. Stanford, S. Oh, and J. Eckerle, "Dielectric Elastomer Artificial Muscle Actuators: Toward Biomimetic Motion," *Smart Structures and Materials 2002: Electroactive Polymer Actuators and Devices*, Yoseph Bar-Cohen, Editor, Proceedings of SPIE, San Diego, CA,Vol. 4695, pp. 126-137, 2002.

62 Pelrine R., P. Sommer-Larsen, R. Kornbluh, R. Heydt, G. Kofod, Q. Pei, and P. Gravesen, "Applications of Dielectric Elastomer Actuators," *Smart Structures and Materials 2001: Electroactive Polymer Actuators and Devices*, Yoseph Bar-Cohen, Editor, Proceedings of SPIE, Newport Beach, CA, Vol. 4329, pp. 335-349, 2001.

63 Perichon Lacour, S., R. Pelrine, S. Wagner, and H. Prahlad, "Photoconductive High-Voltage Switches of Thin-Film Amorphous Silicon for EAP actuators," *Smart Structures and Materials 2003: Electroactive Polymer Actuators and Devices*, Yoseph Bar-Cohen, Editor, Proceedings of SPIE, San Diego, CA, Vol. 5051, pp. 412-418, 2003.

64 Pieper, D.L., "The Kinematics of Manipulators under Computer Control," PhD Thesis, Stanford University, 1968.

65 Plante, J.S., M. Santer, S. Pellegrino, and S. Dubowsky, "Compliant Bistable Dielectric Elastomer Actuators for binary Mechatronic Systems", *Proceedings of IDECT/CIE 2005: ASME Mechanism and Robotics Conference*, Long Beach, CA, 2005.

66 Ritchie, P.D., *Physics of Plastics*, Princeton, N.J: Van Nostrand, 1965.

67 Roth B., J. Rastegar, and V. Scheinman, "On the Design of Computer Controlled Manipulators," *First CISM-IFTMM Symposium on Theory and Practice of Robots and Manipulators*, pp. 93-113, 1973.

68 Santer, M. "The Design of Multistable Structures", M.J. Santer, Doctoral Thesis (submitted), Department of Mechanical Engineering, Cambridge University, England, 2005.

69 Schioler, T. "Multi-stable Structural Elements" Doctoral Thesis, Department of Mechanical Engineering, Cambridge University, England, 2005.

70 Schioler, T. and S. Pellegrino, "Multi-Configuration Space Frames," *45th AIAA/ASME/ASCE/AHS/ASC Structures, Structural Dynamics, and Materials Conference, AIAA, 2004-1529*, Palm Springs, CA, Vol. 1, pp. 271-280, 2004.

71 Schlaak, H.F., M. Jungmann, M. Matysek, and P. Lotz, "Novel Multilayer Electrostatic Solid-State Actuators with Elastic Dielectric," *Smart Structures and Materials 2005: Electroactive Polymer Actuators and Devices*, Yoseph Bar-Cohen, Editor, Proceedings of SPIE, San Diego, CA, Vol. 5759, pp. 121-133, 2005.

72 Slocum A., *Precision Machine Design*, Dearborn, MI: Society of Manufacturing Engineers, 1992.

73 Spong, M. and M. Vidyasagar, *Robot Dynamics and Control*, NewYork: John Wiley & Sons, 1989.

74 Sommer-Larsen P., J. Hooker, G. Kofod, K. West, M. Benslimane, and P. Gravesen, "Response of Dielectric Elastomer Actuators," *Smart Structures and Materials 2001: Electroactive Polymer Actuators and Devices*, Yoseph Bar-Cohen, Editor, Proceedings of SPIE, Newport Beach, CA, Vol. 4329, p157-163, 2001.

75 Sommer-Larsen, P. and A. Ladeggard Larsen, "Materials for Dielectric Elastomer Actuators," *Smart Structures and Materials 2004: Electroactive Polymer Actuators and Devices*, Yoseph Bar-Cohen, Editor, Proceedings of SPIE, San Diego, CA, Vol. 5385, pp. 68-77, 2004.

76 Sujan, V., M. Lichter, and S. Dubowsky, "Lightweight Hyper-Redundant Binary Elements for Planetary Exploration Robots," *Proceedings of the IEEE/ASME International Conference on Advanced Intelligent Mechatronics Proceedings*, Como, Italy, Vol. 2, pp. 1273-1278, 2001.

77 Szabo, J., J. Hiltz, C. Cameron, R. Underhill, J. Massey, B. White, and J. Leidner, "Elastomeric Composites with High Dielectric Constant for use in Maxwell Stress Actuators," *Smart Structures and Materials 2003: Electroactive Polymer Actuators and Devices*, Yoseph Bar-Cohen, Editor, Proceedings of SPIE, San Diego, CA, Vol. 5051, pp. 180-190, 2003.

78 Taillant, E., J.C. Avila-Vilchis, C. Allegrini, I. Bricault, and P. Cinquin, "CT and MR Compatible Light Puncture Robot: Architectural Design and First Experiments," *Lecture Notes in Computer Science - Medical Image Computing and Computer-Assisted Intervention - MICCAI 2004 - 7th International Conference Proceedings*, Vol. 3217, pp. 145-152, 2004.

79 Vogan, J., A. Wingert, M. Hafez, J.S. Plante, S. Dubowsky, D. Kacher, and F. Jolesz, "Manipulation in MRI Devices Using Electrostrictive Polymer Actuators: with an Application to Reconfigurable Imaging Coils," *2004 IEEE International Conference on Robotics and Automation*, New Orleans, Louisiana, Vol. 2004, No. 3, pp. 2498-2504, 2004.

80 Vogan J., "Development of Dielectric Elastomer Actuators for MRI Devices," M.S. Thesis, Department of Mechanical Engineering, Massachusetts Institute of Technology, Cambridge, MA, 2004.

81 Whithead, S., *Dielectric Breakdown of Solids*, Oxford University Press, 1953.

82 Wingert, A., M.D. Lichter, and S. Dubowsky, "On the Kinematics of Parallel Mechanisms with Bistable Polymer Actuators," *Proceedings of the 8th International Symposium on Advances in Robot Kinematics*, Barcelona, Spain, June 2002.

83 Wingert, A., M.D. Lichter, S. Dubowsky, and M. Hafez, "Hyper-Redundant Robot Manipulators Actuated by Optimized Binary Dielectric Polymers," *Smart Structures and Materials 2002: Electroactive Polymer Actuators and Devices*, Yoseph Bar-Cohen, Editor, Proceedings of SPIE, San Diego, CA, Vol. 4695, pp. 415-423, 2002.

84 Wingert A., "Development of a Polymer-Actuated Binary Manipulator", M.S. Thesis, Department of Mechanical Engineering, Massachusetts Institute of Technology, Cambridge, MA, 2002.

85 Wissler, M. and E. Mazza, "Modeling of a Pre-Strained Circular Actuator Made of Dielectric Elastomers," *Sensors and Actuators*, Vol. 120, pp. 184-192, 2005.

86 Yang, W.H. and W.W. Feng, "On Axisymmetrical Deformations of Nonlinear Membranes," *Journal of Applied Mechanics*, Vol. 37, No. 4, pp.1002-1011, 1970.

87 Yang, E., M. Frecker, and E. Morckensturm, "Viscoelastic Model of Dielectric Elastomer Membranes," *Smart Structures and Materials 2005: Electroactive Polymer Actuators and Devices*, Yoseph Bar-Cohen, Editor, Proceedings of SPIE, San Diego, CA, Vol. 5759, pp. 82-93, 2005.

88 Yang, P. and K.J. Waldron, "Massively Parrallel Actuation," *Proceedings of the IEEE/ASME International Conference on Advanced Intelligent Mechatronics*, Como, Italy, Vol. 2, pp. 868-873, 2001.

89 Zhang, X., M. Wissler, B. Jaehne, R. Broennimann, and G. Kovacs, "Effects of Crosslinking, Prestrain and Dielectric filler on the Electromechanical Response of a New Silicone and Comparison with Acrylic Elastomer," *Smart Structures and Materials 2004: Electroactive Polymer Actuators and Devices*, Yoseph Bar-Cohen, Editor, Proceedings of SPIE, San Diego, CA, Vol. 5385, pp. 78-86, 2004.

APPENDIX

A

DETAILS OF THE DIAMOND ACTUATOR

A.1 Introduction

This Appendix presents details of the manufacturing and assembly processes of diamond actuators.

A.2 Parts Fabrication

Figure 89 to Figure 93 show the details of the structural and interstitial frames of the 107 and 54 mm actuators developed in this thesis. Those parts are manufactured from numerical processes using CAD files and do not require detailed engineering drawings. Accordingly, the drawings only give outside dimensions and critical features. All dimensions are in millimeters.

The structural frames are fabricated by CNC milling using 0.79 and 1.59 mm end mills (1/32" and 1/16"). The interstitial frames are cut using laser cutting.

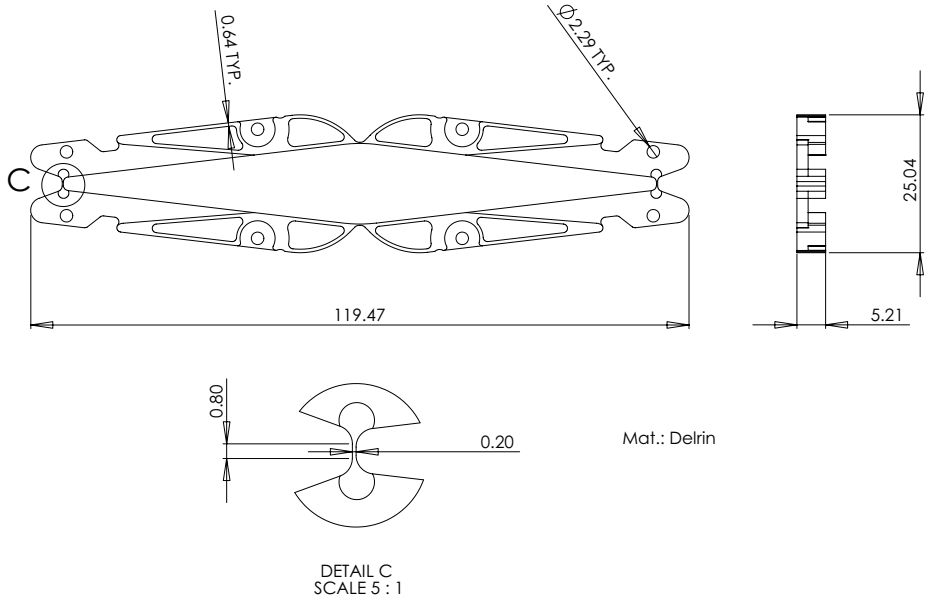

Figure 89: Engineering drawing, structural frame, 107 mm actuator.

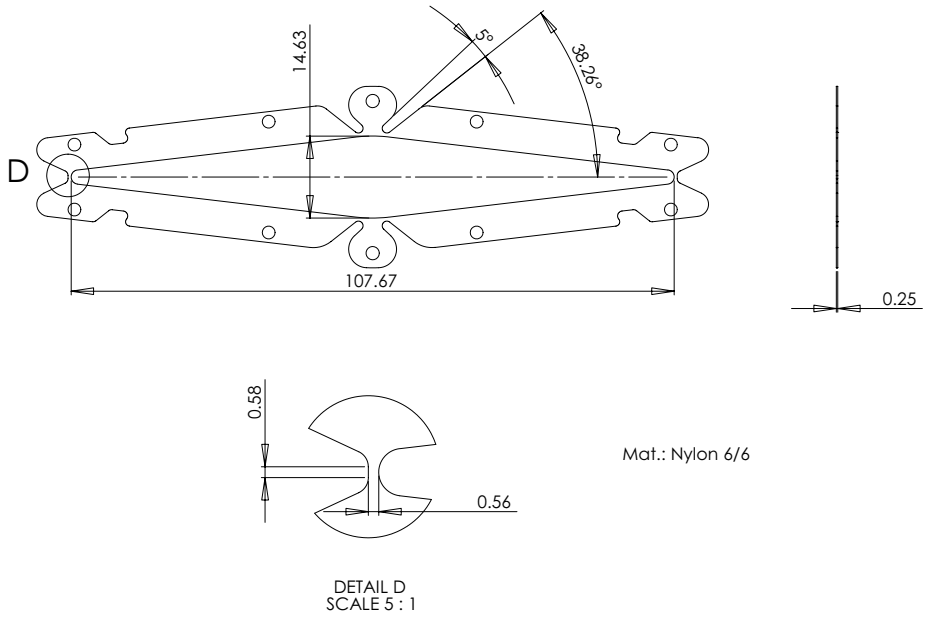

Figure 90: Engineering drawing, interstitial frame, 107 mm actuator.

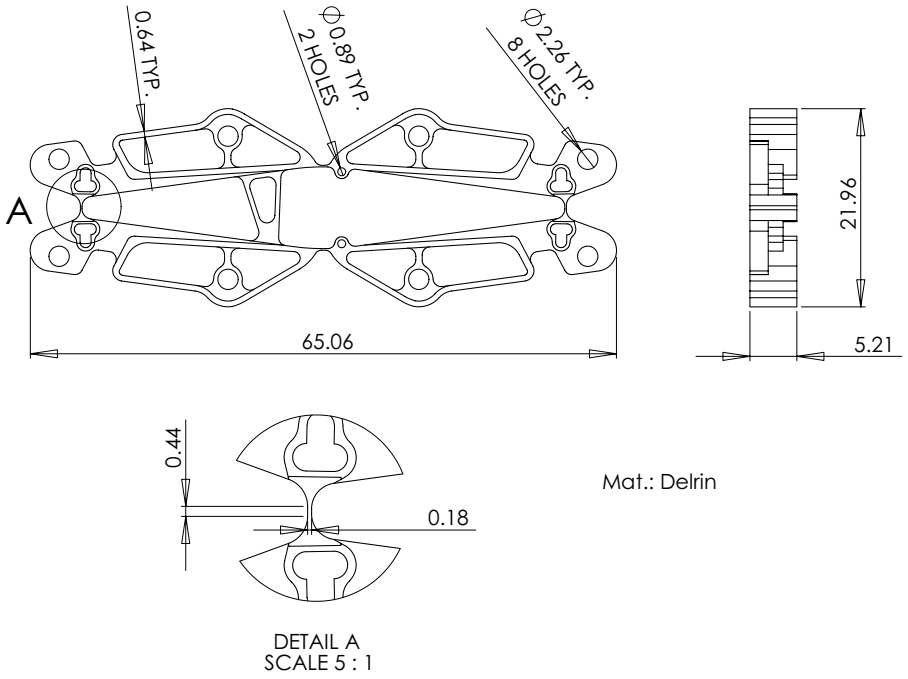

Figure 91: Engineering drawing, structural frame, 54 mm actuator.

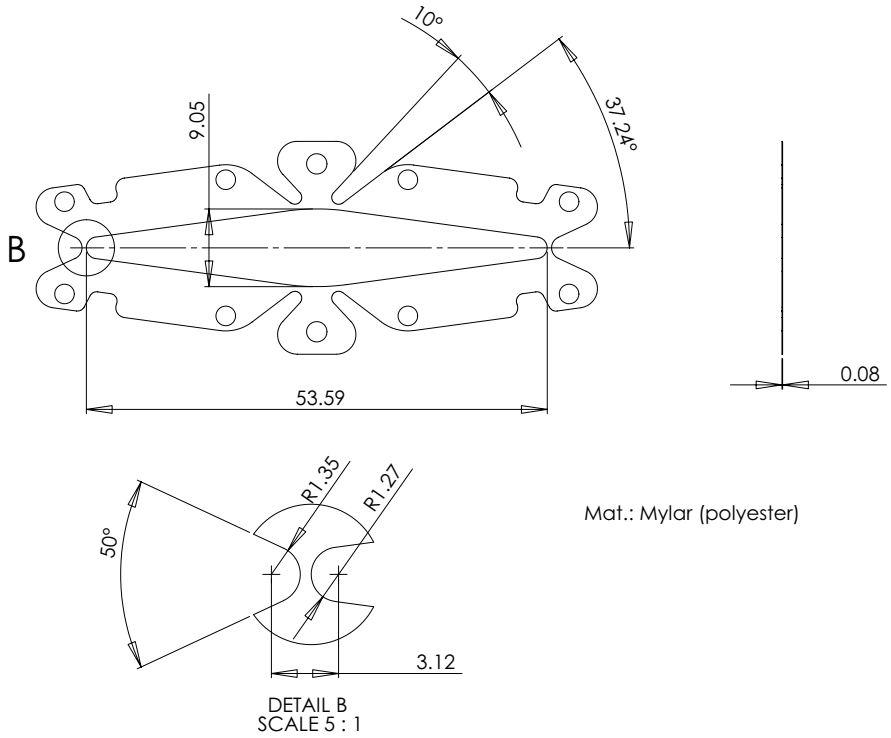

Figure 92: Engineering drawing, interstitial frame, 54 mm actuator.

A.3 Assembly Process

Multi-layer diamond actuators are assembled as follow:

1. A piece of 3M's VHB 4905/4910 industrial adhesive polymer film is pre-stretched per the procedure described in Appendix B. Actuators developed in this thesis use 1.5 mm thick films manufactured by laminating three layers of 0.5 mm thick VHB 4905 films. The films are pre-stretched to $\lambda_{1,pre} x \lambda_{2,pre} = 5x2.2$. This combination corresponds to a pre-stretch area expansion of 11 which maximizes actuator extension capabilities according to Figure 60 on page 99.
2. The film is then sandwiched between a pair of interstitial frames. To decrease manufacturing times and ease assembly, the interstitial frames are grouped in arrays of 6 parts as shown on Figure 93. The alignment between the interstitial frames during bonding is performed with the assembly jig shown on Figure 94. Pressure must be applied all across the bonding area to remove air bubbles. The sub-assembly must relax for at least 12 hours to let the bond strength increase over time since full strength is reached in 72 hrs [1].

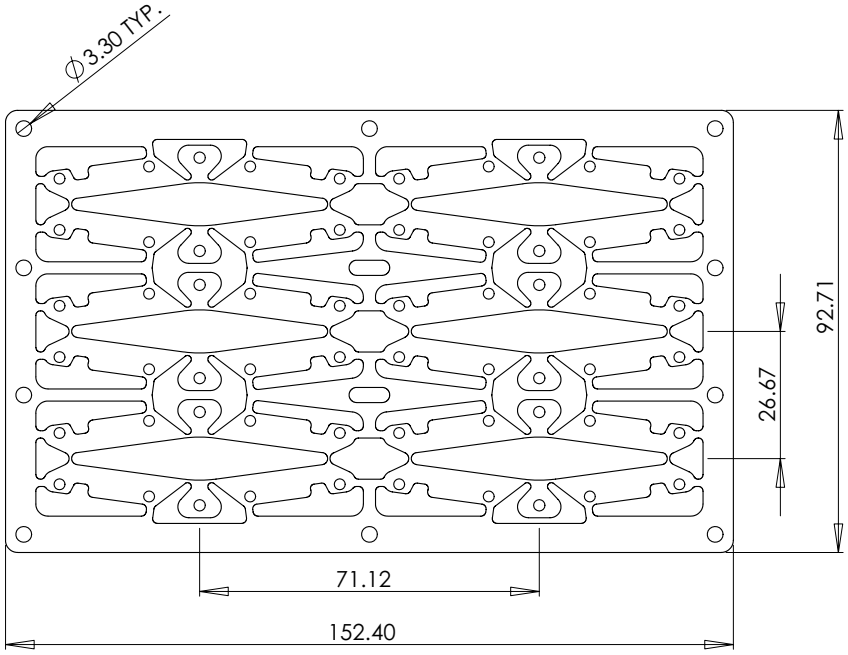

Figure 93: Engineering drawing, interstitial frame array, 54 mm actuator.

Figure 94: Interstitial frames assembly jig.

3. 3M's 1099 elastomer glue is cast into the frame hinges to insure proper film holding, see Figure 95. The glue is let to dry for at least 4 hours.

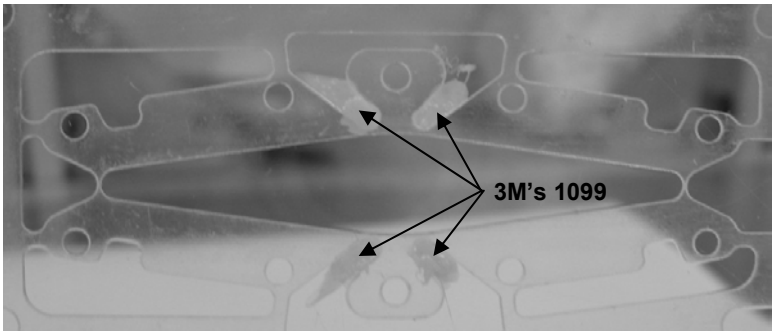

Figure 95: Adhesive in interstitial frame hinges.

4. Electrodes are hand brushed with a paste-like mixture of ethyl alcohol and carbon power. Leads made from aluminized adhesive tape are stuck to the interstitial frames to feed the electrodes.

Steps 1 to 4 are repeated as needed and the layers are sandwiched between a pair of structural frames. The system is completed with proper fasteners and elastic bands.

APPENDIX

B

POLYMER FILM STRETCHING

B.1 Introduction

This Appendix provides details of the film pre-stretching technique. Pre-stretching is a crucial step to any DE experimental work and should be done with care.

B.2 Procedure

The experimental film stretching setup is shown on Figure 96. A two axis stretching apparatus is operated inside a clean bench to insure a dust free environment. Pre-stretching is executed in two steps. The film sample is first clamped across one axis and the initial dimensions, L and W, are measured such as in Figure 97(a). Next, the length is increased to the desired stretch in the first direction:

$$l = L\lambda_{1,pre} \tag{B.1}$$

After obtaining the configuration shown in Figure 97(b), the free edges are clamped with the second set of clamps, see Figure 97(c). The free width of the sample, w_a, and the clamped width, w_b, are measured. To account for the amount of clamped material, the initial length in the secondary axis is linearly scaled:

$$W' = \frac{w_b}{w_a} W \tag{B.2}$$

By expanding the clamped edges, the film is then brought to its final stretched configuration as shown on Figure 97(d) where the final width is obtained from the second direction stretch:

$$w = \lambda_{2,pre} W' \tag{B.3}$$

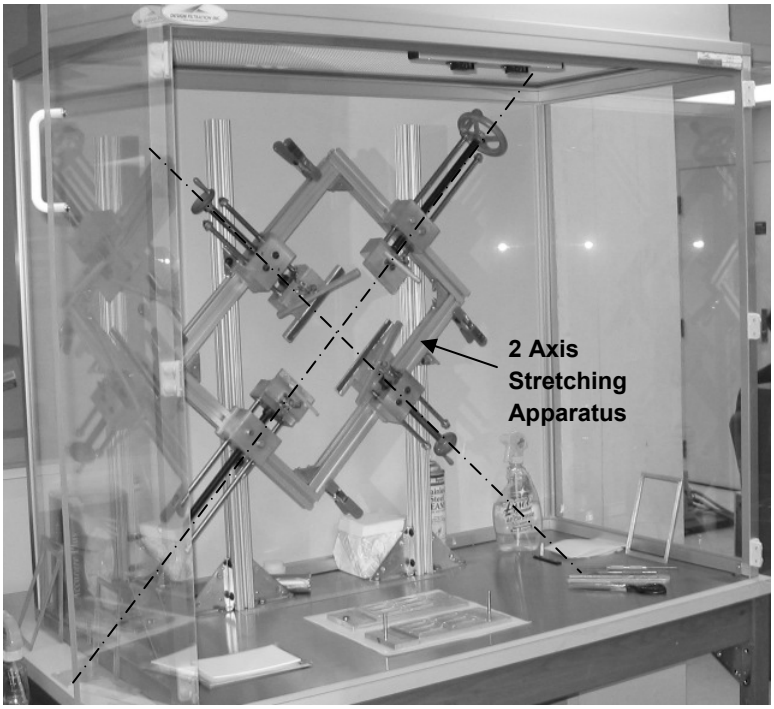

Figure 96: Experimental film stretching setup.

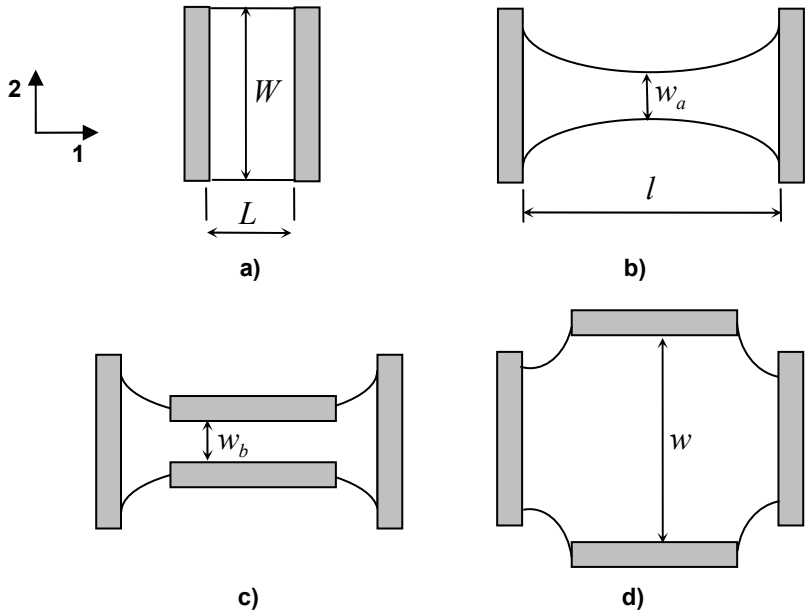

Figure 97: Film stretching sequence.

B.3 Validation

Stretching elastomer films to large values causes film slippage problems. Therefore, to verify that the final stretches are valid, the resulting thickness was measured and compared with the thickness calculated by the constant volume assumption. Multiple elastomer samples were stretched and their final thicknesses were measured with a Mitutoyo torque limited micrometer (model # 293-761-30). The measurements are plotted against predictions from the constant volume assumption in Figure 98. The scattering of midrange data is attributed to slight film slippage from under the clamps, which results in higher measured thickness. The data scattering disappears for high pre-stretch because film slippage becomes small in comparison with the total film area. In general, experimental data match the constant volume curve well. Therefore, the stretching technique is considered adequate for the scope of this work.

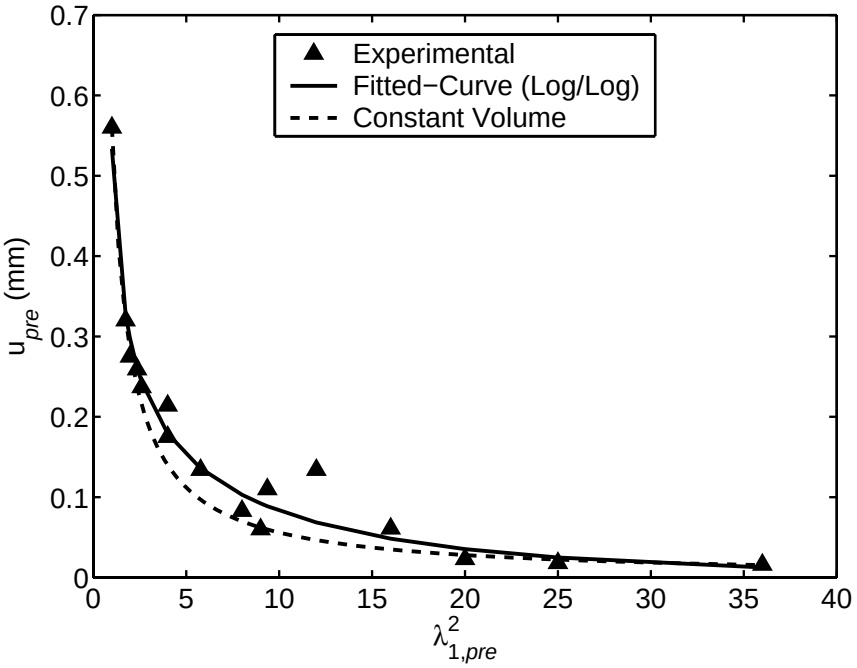

Figure 98: Experimental vs. constant volume film thickness.

APPENDIX

C

OGDEN PARAMETERS

C.1 Introduction

This Appendix describes how Ogden model parameters are derived from uniaxial tensile tests.

C.2 Uniaxial Stress Formulation

Consider a rectangular sample in uniaxial deformation along its first principal direction as shown on Figure 99. The principal stretches for an incompressible material like VHB 4905/4910 are given by:

$$\lambda_1 = \frac{l}{l_0}$$
$$\lambda_2 = \lambda_3 = \lambda_1^{-0.5} \tag{C.1}$$

where l_0 and l are the sample lengths in the reference and deformed configurations.

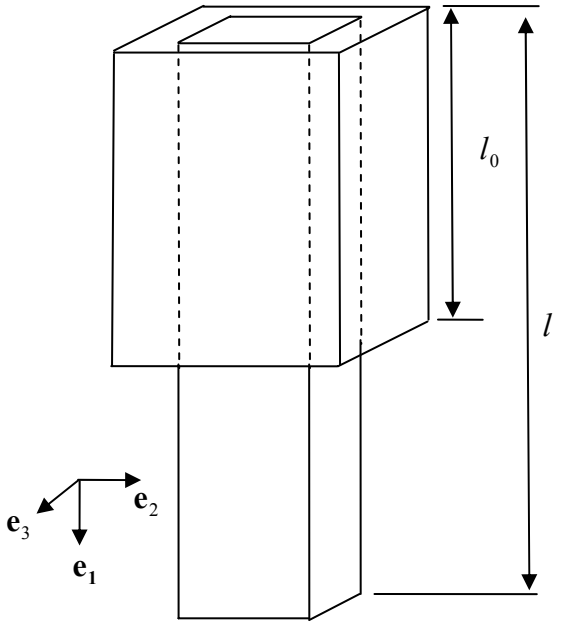

Figure 99: Uniaxial deformation of a rectangular sample.

The corresponding engineering stresses as given by a second order Ogden model such as Eq. (2.19) on page 44 are:

$$\begin{aligned} S_1 &= \mu_1 \lambda_1^{(\alpha_1 - 1)} + \mu_2 \lambda_1^{(\alpha_2 - 1)} - \mu_1 \lambda_1^{-(1+0.5\alpha_1)} - \mu_2 \lambda_1^{-(1+0.5\alpha_2)} \\ S_2 &= S_3 = 0 \end{aligned} \tag{C.2}$$

The Ogden parameters $\alpha_1, \alpha_2, \mu_1, \mu_2$ are obtained by curve fitting experimental data from a uniaxial test onto the S_1 stress of Eq. (C.2).

C.3 Experiment Data

The specimen's nominal clamped dimensions were arbitrarily set to 15 x 15 mm. Stresses and stretches were measured on the actuator dynamometer described in Section 3.2.1.

Uniaxial tests with different stretch rates were performed to investigate viscoelastic effects. Figure 100 shows filtered experimental data of the engineering stresses vs. stretches for four different stretch rates, $\dot{\lambda}_{UNI}$, ranging from $3.1\text{x}10^{-5}$ s^{-1} to 1.8 s^{-1}. The stretch rate $\dot{\lambda}_{UNI}=3.3\text{x}10^{-4}$ s^{-1}, (b), is interesting because it represents the equilibrium case where viscoelastic effects are negligibly small and the material response is mostly elastic (independent of stretch rate). As shown by Figure 100, curves (a) and (b) are almost identical despite curve (a) having a stretch rate 10 times lower. The dashed curves superimposed on (b), (c) and (d) are curve-fitted Ogden models. The curve fits were done with the NonlinearRegress function in the Mathematica® Software. Table 9 summarizes the Ogden model parameters that are valid for stretches of up to 7.

Table 9: Ogden model parameters from uniaxial tests.

Ogden parameters	Low stretch rate $\dot{\lambda}_{UNI} = 3.3\text{x}10^{-4}$ s^{-1}	High stretch rate $\dot{\lambda}_{UNI} = 0.094$ s^{-1}	Very high stretch rate $\dot{\lambda}_{UNI} = 1.8$ s^{-1}
α_1	1.445	1.450	1.543
α_2	4.248	8.360	8.360
μ_1	43 560	112200	150579
μ_2	117.4	0.1045	0.3393

Under high stretch rates, significant viscous stresses are generated on the viscoelastic side of the rheologic model. These viscoelastic stresses add to the baseline elastic stresses and explain the viscous impedance observed on Figure 100. For example, compare the stresses of curve (b) to curve (c) at a stretch ratio of about 6. The stress of curve (b), the equilibrium case, is only 50% of the stress of curve (c). Thus, under high stretch rates, viscous stresses can account for more than half the total stress.

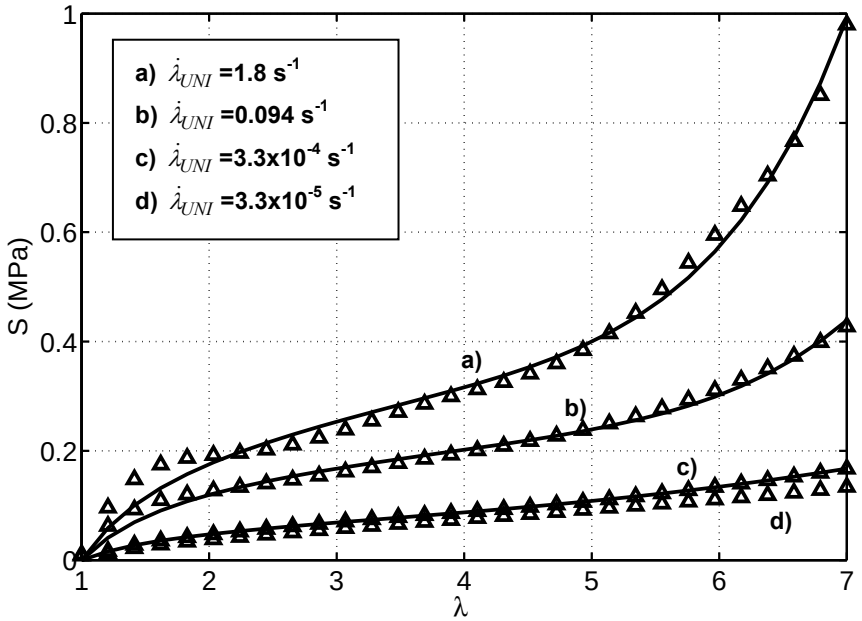

Figure 100: Experimental stress/stretch curves for uniaxial extension of VHB 4905/4910 at different stretch rates. The solid curves superposed on (a), (b) and (c) are curve-fitted Ogden models.

APPENDIX

D

BERGSTROM-BOYCE PARAMETERS

D.1 Introduction

This Appendix presents the method used to define the Bergstrom-Boyce model parameters used in the analysis of diamond actuators in Chapter 3.

D.2 Network A

Network A is the only active network at very low stretch rates where viscous effects are negligibly small. Its Ogden's parameters are found from stress/stretch data obtained below the *equilibrium* stretch rate, the threshold value for viscous effects.[1]

In theory, Ogden parameters could be determined from uniaxial tests. However, this approach does not give good accuracy because uniaxial deformations are quite far from highly asymmetric biaxial stretching of the diamond actuators. Hence Ogden parameters for network A are defined by curve fitting an analytical model of the diamond actuator film over experimental data obtained bellow the equilibrium stretch rate.

The analytical model is obtained from the relation between the film planar stresses and the film force of Eq. (3.12) on page 68. The planar stresses in this equation

[1] See Appendix C for more details about the equilibrium stretch rate of VHB 4905/4910.

must be substituted for Ogden model based expressions. A first order Ogden model with $\sigma_3 = 0$ gives:

$$\begin{aligned}\sigma_1 &= \mu_1\left(\lambda_{1,tot}\right)^{\alpha_1} - \mu_1\left(\lambda_{3,tot}\right)^{\alpha_1} \\ \sigma_2 &= \mu_1\left(\lambda_{2,tot}\right)^{\alpha_1} - \mu_1\left(\lambda_{3,tot}\right)^{\alpha_1}\end{aligned} \tag{D.1}$$

Substituting further with Eqs. (2.9) to (2.13) and (3.17) gives:

$$F_F = Ul\Theta\left[\left(\mu_1\Psi^{\alpha_1} - \mu_1\Theta^{\alpha_1}\right)\cdot\cos\Phi - \left(\mu_1\Omega^{\alpha_1} - \mu_1\Theta^{\alpha_1}\right)\cdot\left(\frac{y}{2l}\right)\cdot\tan\Phi\right] \tag{D.2}$$

where the functional groups $\Theta, \Psi, \Phi, \Omega$ are:

$$\begin{aligned}\Theta &= \frac{\cos\theta_0 \sin\theta_0}{\lambda_{1,pre}\lambda_{2,pre}\left(\frac{y}{2l}\right)\cos\Phi} \\ \Psi &= \lambda_{2,pre}\left(\frac{y}{2l}\right)\frac{1}{\sin\theta_0} \\ \Phi &= \arcsin\left(\frac{y}{2l}\right) \\ \Omega &= \lambda_{1,pre}\frac{\cos\Phi}{\cos\theta_0}\end{aligned} \tag{D.3}$$

Equations (D.2) and (D.3) express the film force in terms of the diamond minor axis y: $F_F = f\left[\{y\},\{\mu_1,\alpha_1\},\{l, y_0, U, \lambda_{1,pre}, \lambda_{2,pre}\}\right]$. The parameters μ_1, α_1 are Ogden parameters and $l, y_0, U, \lambda_{1,pre}, \lambda_{2,pre}$ are actuator specifications.

The Ogden parameters were curve-fitted using nonlinear regression techniques, see Figure 101 on next page. The experimental force/displacement data was obtained

from a 107 mm diamond actuator described in Chapter 2. The force/displacement contributions of the structural and interstitial frames were subtracted from the test data to isolate the film force data. The actuator was deformed well below the equilibrium stretch rate to insure negligible viscous effects. The resulting Ogden parameters are μ_1=60 000 and α_1 =1.8.

D.3 Network B

The parameters of network B are more difficult to determine because its elastic and plastic parts are simultaneously active during film deformation and therefore can't be isolated. In such cases, parameters are estimated from first order calculations and educated guesses. The parameters used in this thesis are summarized in Table 10 on next page.

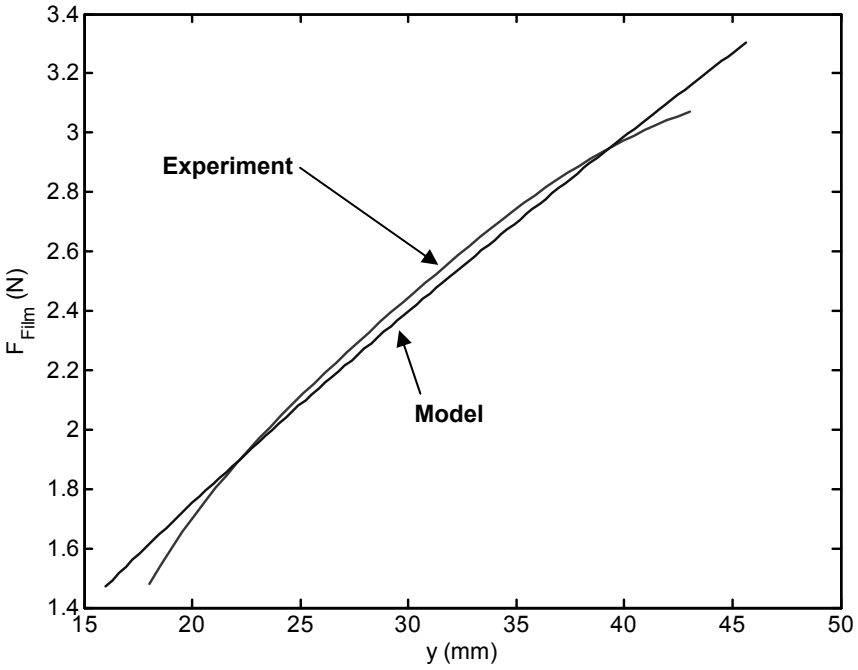

Figure 101: Bergstrom-Boyce network A parameters curve fit.

Table 10: Bergstrom-Boyce network B parameters.

Parameters		Values	Units
Elastic side: 2nd order Ogden model	μ_1	30000	Pa
	α_1	4	
	μ_2	1000	Pa
	α_2	6	
Plastic side: modified BB	$\hat{C}_1$	2500	$s^{-1} Pa^{-m}$
	C_2	6	
	C_3	1.4	
	m	0.9	

APPENDIX

E

IDEAL ACTUATOR PASSIVE REGION MODEL

E.1 Introduction

This Appendix describes a solid mechanics model of an ideal actuator's passive region. The passive region is modeled as an annular membrane with imposed inner and outer radial displacements. The mathematical treatment of general nonlinear axisymmetric membranes is well known. For more details the reader is referred to the literature [30,53,86].

E.2 Kinematical Description

Figure 102 shows a cross-section of the passive region with associated radial positions in the reference (stress free) and actuated configurations. The model does not explicitly use a pre-stretched configuration.

The geometrical boundary condition of continuity imposes the initial membrane radii, R_a and R_b. The inner radius, R_a, projected in the pre-stretched configuration must be equal to the active region's outer radius $R_a \lambda_{1,pre} = r_{pre}$ (see Figure 49 on page 84). Similarly, the outer radius, R_b, projected in the pre-stretched configuration must be equal to the rigid ring's radius $R_b \lambda_{1,pre} = r_{rig}$. These conditions lead to:

$$R_a = \frac{r_{pre}}{\lambda_{1,pre}}$$
$$R_b = \frac{r_{rig}}{\lambda_{1,pre}} \qquad \text{(E.1)}$$

All predictions in this thesis were made with r_{pre}=5.6 mm and r_{rig}=100 mm.

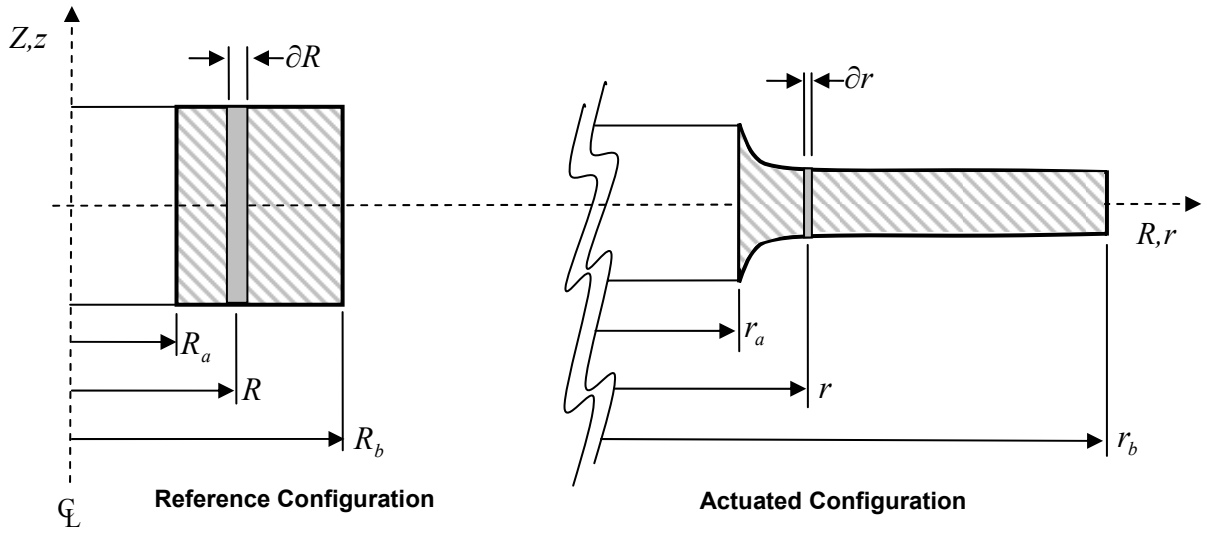

Figure 102: Deformation of the passive region model.

Using the stretch definition of Eq. (2.1) on page 35, the principal stretches in the 1,2,3 directions aligned with the r,θ,z and R,Θ,Z directions are [86]:

$$\lambda_1 = \frac{\partial r}{\partial R}$$
$$\lambda_2 = \frac{r}{R} \qquad \text{(E.2)}$$
$$\lambda_3 = \frac{1}{\lambda_1 \lambda_2}$$

where λ_3 is obtained from the incompressibility relation: $\lambda_1 \lambda_2 \lambda_3 = 1$.

E.3 Stress Balance

The principal stresses associated with the principal directions must satisfy Cauchy's equation of equilibrium, $\text{div}\boldsymbol{\sigma} = \mathbf{0}$, resolved in the actuated configuration [53]:

$$\frac{\partial \sigma_1}{\partial r} + \frac{1}{r}(\sigma_1 - \sigma_2) = 0 \tag{E.3}$$

Equations (E.2) and (E.3) are merged in two first order differential equations:

$$\begin{aligned} \frac{\partial \lambda_1}{\partial R} &= \frac{\lambda_1}{R\lambda_2} \cdot \frac{\sigma_2 - \sigma_1}{\dfrac{\partial \sigma_1}{\partial \lambda_1}} - \frac{\lambda_1 - \lambda_2}{R} \cdot \frac{\dfrac{\partial \sigma_1}{\partial \lambda_2}}{\dfrac{\partial \sigma_1}{\partial \lambda_1}} \\ \frac{\partial \lambda_2}{\partial R} &= \frac{\lambda_1 - \lambda_2}{R} \end{aligned} \tag{E.4}$$

where the Cauchy stresses are found from a second order Ogden model given by:

$$\begin{aligned} \sigma_1 &= \mu_1\left((\lambda_1)^{\alpha_1} - \frac{1}{(\lambda_1)^{\alpha_1}(\lambda_2)^{\alpha_1}}\right) + \mu_2\left((\lambda_1)^{\alpha_2} - \frac{1}{(\lambda_1)^{\alpha_2}(\lambda_2)^{\alpha_2}}\right) \\ \sigma_2 &= \mu_1\left((\lambda_2)^{\alpha_1} - \frac{1}{(\lambda_1)^{\alpha_1}(\lambda_2)^{\alpha_1}}\right) + \mu_2\left((\lambda_2)^{\alpha_2} - \frac{1}{(\lambda_1)^{\alpha_2}(\lambda_2)^{\alpha_2}}\right) \\ \sigma_3 &= 0 \end{aligned} \tag{E.5}$$

The pair of differential equations of Eq. (E.4) are solved numerically by transforming the boundary value problem into an initial condition problem [86]. In the transformed problem, the stretches are calculated iteratively from the inner radius R_a to the outer radius R_b until the calculated outer radius (in the actuated configuration)

converges to the rigid ring radius $r_b = r_{rig}$. The inner hoop stretch λ_2 is equal to the active region's value: $\lambda_2 = \lambda_{2,tot}$. The inner radial stretch λ_1 is unknown and is the iterated variable.

E.4 Solution Example

Consider a film pre-stretched to $\lambda_{1,pre} = 1.96$ and actuated to $\lambda_{1,act} = 2$. The calculated principal stretches and engineering stresses are shown respectively in Figure 103 and Figure 104. Compared to the pre-stretched configuration, Figure 103 shows that, near the inside radius, R_a, the polymer chains in the hoop direction are further extended $\lambda_1 > \lambda_{1,pre}$ while those in the radial direction are relaxed, $\lambda_2 < \lambda_{1,pre}$. Accordingly, Figure 104 shows that the hoop stresses increase while the radial stresses decrease. The stresses and stretches both converge back toward the pre-stretched values in the far field when $R \to R_b$.

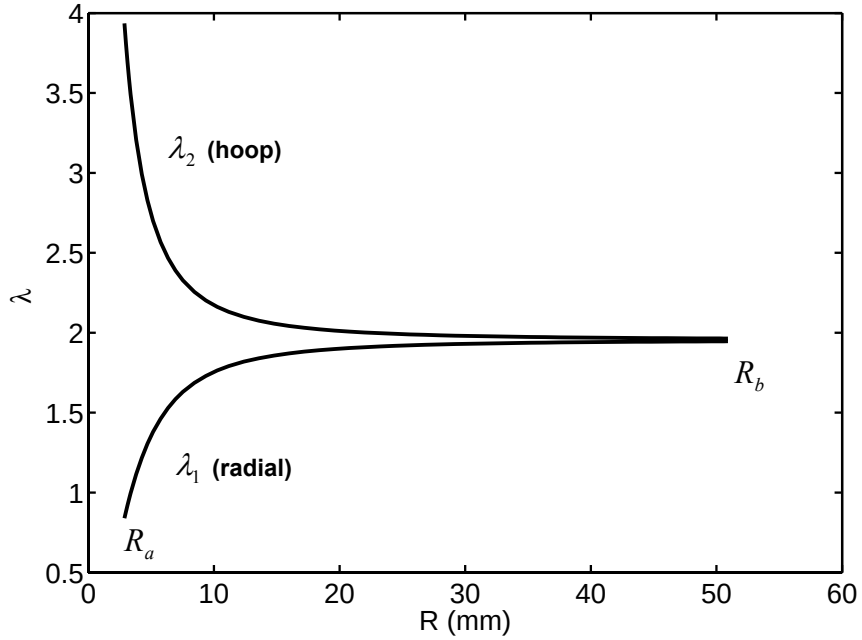

Figure 103: Example of stretch distribution in the passive region.

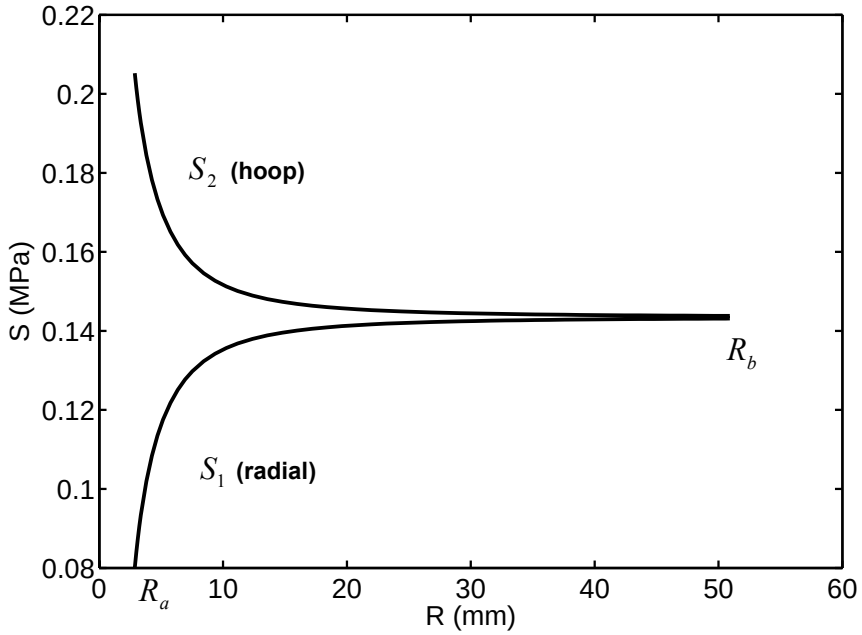

Figure 104: Example of engineering stress distribution in the passive region.

E.5 Boundary Condition

The model's interface between the active/passive regions is discontinuous. In such a case, Cauchy's stress balance imposes equal normal engineering stresses across the interface. Hence, in the discontinuous case, the active region's radial stress must equal the passive region inner radial stress $S_1(R_a)$:

$$S_{1,act}{}_{discontinuous} = S_1(R_a) \tag{E.6}$$

However, the true deformed shape is continuous. Compared to the discontinuous case, the continuous case implies extra material deformation to force the edges together and, thus, extra deformation energy. This extra energy must come from higher Maxwell pressures, and higher Maxwell pressures means *lower* (more compressive) radial stresses

in the active region. Consequently, the validity of Eq. (E.6) for large actuation stretches is not guaranteed.

A FE model of the passive region was developed to study the effect of the thickness discontinuity on the active region's planar stresses. The FE model was implemented in Adina® using axisymmetric 2D Solid elements and the Ogden material model parameters for high stretch rates ($\dot{\lambda}_{UNI}$=0.094 s^{-1}), see Appendix C. Both the discontinuous and continuous cases were run with pre-stretches of $\lambda_{1,pre}$ = 1.96 and actuation stretches of $\lambda_{1,act}$ = 1.05, 1.2, 2 and 3. The resulting shapes are shown in Figure 105 for $\lambda_{1,act}$ = 2.

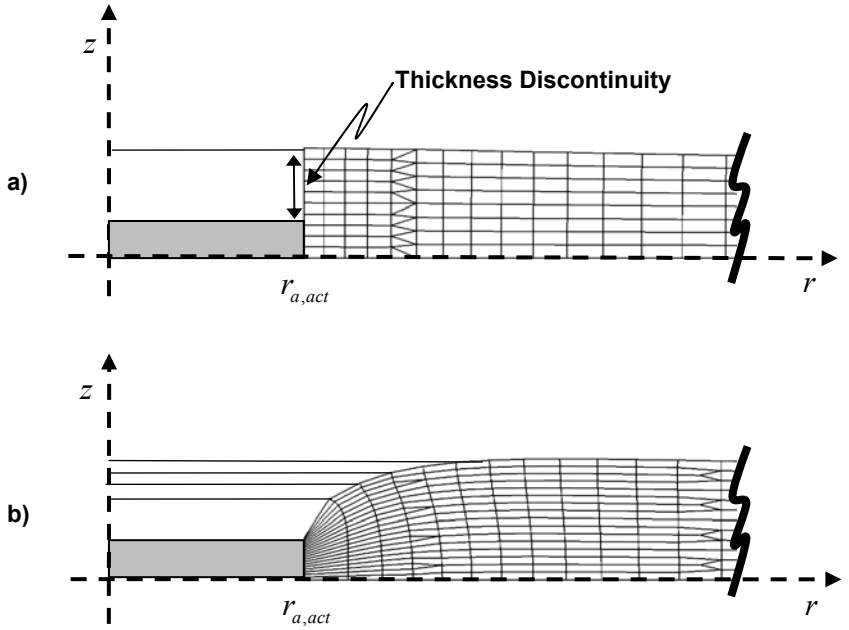

Figure 105: Passive region's deformed shape computed with Adina® when inner face is: (a) discontinuous, and (b), continuous (not to scale).

The engineering planar stresses in the active region given by the FE simulations and those from analytical model using two different boundary conditions are shown in Figure 106. Looking at the FE results only, the planar stresses decrease significantly faster in the Continuous-FE case compared to the Discontinuous-FE case because it

requires more deformation energy. The Continuous-FE case is set as the desired curve that should be obtained by the analytical boundary condition.

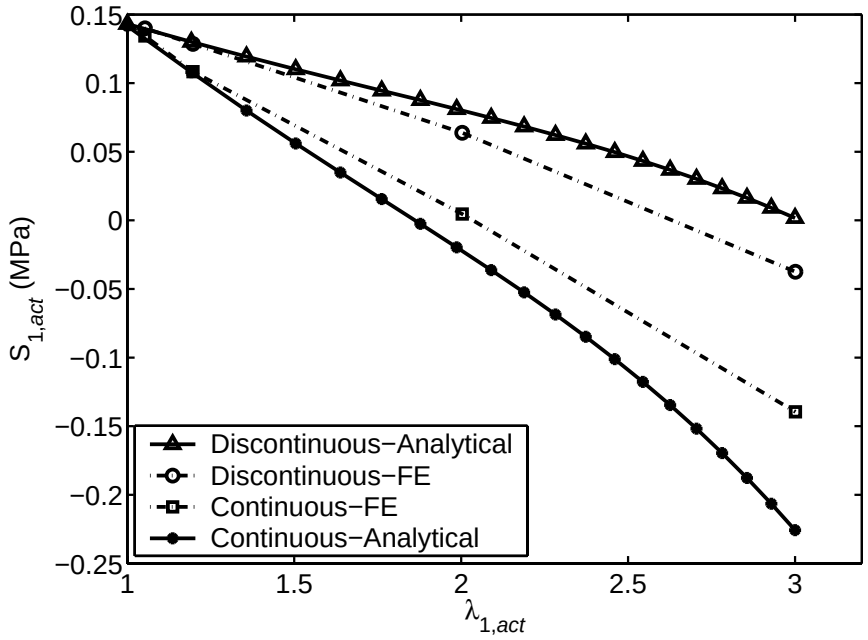

Figure 106: Planar stress in the active region vs. actuation stretch for analytical and FE models.

Now looking at the analytical results, Figure 106 shows that the Discontinuous-Analytical curve computed with Eq. (E.6) follows the Discontinuous-FE case reasonably well. This validates the membrane approximation.

The Continuous-Analytical curve of Figure 106 is computed with an empirical boundary condition adjusted to follow the Continuous-FE levels. This boundary condition is explained by Figure 107 that shows a linear schematic of the planar stresses vs. actuation stretch of Figure 106. For a given actuation stretch, the stress difference between the free and prescribed cases, ΔS_2, is assumed proportional to the stress difference between the free case and pre-stretch stress, ΔS_1:. The quasi-linearity of the results of Figure 106 suggests that the proportionality approximation is valid over significant actuation stretches.

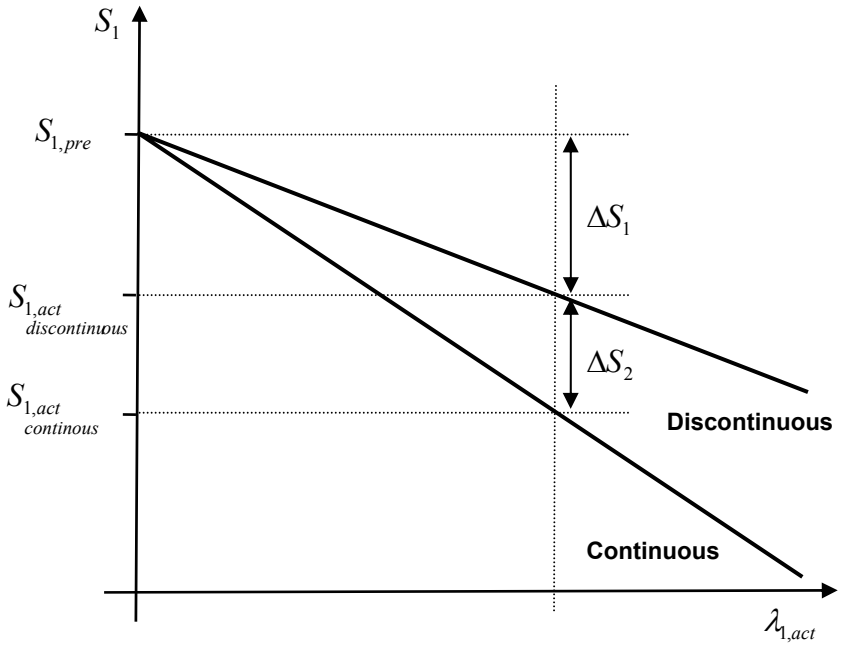

Figure 107: Schematic of the planar stress in the active region vs. actuation stretch.

The proportionality relationship $\Delta S_2 \propto \Delta S_1$ is written with the terms of Figure 107 as:

$$S_{1,act}{}_{discontinuous} - S_{1,act}{}_{continuous} = k\left(S_{1,pre} - S_{1,act}{}_{discontinuous} \right) \tag{E.7}$$

where k is the proportionality constant. Substituting $S_{1,act}{}_{discontinuous}$ by Eq. (E.6) and rearranging gives the empirical boundary condition used in the failure modes study:

$$S_{1,act}{}_{continuous} = S_1(R_a) - k\left(S_{1,pre} - S_1(R_a)\right) \tag{E.8}$$

The proportionality constant was found to be k=1.6 based on two criteria: (1) the predictions should follow the Continuous-FE levels of Figure 106 and (2) the predictions should give realistic actuation area expansion levels (see Figure 58 on page 97).

Finally, the boundary condition of Eq. (E.8) must be converted to a true stress by the Piola transformation (see Eq. (2.21) on page 45) to be compatible with the active region model:

$$\sigma_{1,act} = \left[S_1(R_a) - k\left(S_{1,pre} - S_1(R_a)\right)\right] \lambda_{1,tot} \tag{E.9}$$

E.6 Loading Stress

The boundary condition of Eq. (E.9) is modified to incorporate the effect of an external loading stress σ_{load} that simulates diamond actuators:

$$\sigma_{1,act} = \left[S_1(R_a) - k\left(S_{1,pre} - S_1(R_a)\right)\right] \lambda_{1,tot} - \sigma_{load} \tag{E.10}$$

A typical loading stress function is estimated from force measurements performed on diamond actuators such as schematized in Figure 15 on page39. The actuators consisted of a single 1.5mm thick film pre-stretched to $\left[\lambda_{1,pre}, \lambda_{2,pre}\right]$ = [5,2.2] and mounted to a l=55 mm diamond actuator frame operating between $\{u$=0.14 mm $, \theta$=9$^o\}$and $\{u$=0.06 mm, θ=24$^o\}$. Actuation area expansion is 2.28. Experimental measurements of Chapter 3 showed that, under constant voltage, the loading force of diamond actuators is approximately constant for a given stretch rate:

- F_{load} ~1.75 N at low stretch rates, $\dot{\lambda}_{UNI}$=3.3x10^{-4} s^{-1}, corresponding to a diamond actuator velocity of 0.006 mm/s (see Figure 40 on page 70).

- F_{load} ~0.875 N at high stretch rates, $\dot{\lambda}_{UNI}$ =0.094 s^{-1}, corresponding to a diamond actuator velocity of 2 mm/s (see Figure 43 on page 71).

The loading stress, σ_{load}, is related to the actuator loading force, F_{load}, in the same way that the Maxwell pressure, P, is related to the Maxwell force, F_M, in Eq. (3.13) on page 69. Hence the loading stress is given by:

$$\sigma_{load} = \frac{F_{load}}{lu\cos\theta(\tan^2\theta - 1)} \tag{E.11}$$

According to Eq. (E.11), the loading stress varies from $\sigma_{load} = 0.14F_{load}$ in the closed configuration to $\sigma_{load} = 0.42F_{load}$ in the opened configuration. The loading stress variation with area expansion is transposed linearly to ideal actuators by:

$$\sigma_{load} = \left[0.14 + 0.56\left(\lambda_{1,act} - 1\right)\right] F_{load} \tag{E.12}$$

where $\lambda_{1,act}$ is the radial actuation stretch. For example, a diamond actuator operating at an actuation area expansion of 2.28 corresponds to an ideal actuator operating at $\lambda_{1,act} = \sqrt{2.28} = 1.5$ which, when inserted into Eq. (E.12) yields the same stress of $\sigma_{load} = 0.42F_{load}$

APPENDIX

F

SPACE EXPLORATION MICROBOTS

F.1 Introduction

This Appendix presents an application of DE actuators to small hopping robots for space exploration called "Microbots" [21]. The following description focuses on the mobility system only. For more information the reader is referred to [21].

F.2 Mission Concept

The proposed mission concept for planetary exploration is based on the deployment of a large number of small spherical Microbots over vast areas of a planet's surface and subsurface, including structures such as caves and near-surface crevasses, see Figure 108. This would allow extremely large-scale in situ analysis of terrain composition and history. This approach represents an alternative to rover and lander-based planetary exploration, which is limited to studying small areas of a planet's surface at a small number of sites.

A large number (i.e. hundreds or thousands) of cm-scale, sub-kilogram microbots would be distributed over a planet's surface by an orbital craft and would employ hopping, bouncing and rolling as a locomotion mode to reach scientifically interesting artifacts in very rugged terrain. They would be powered by DE actuators and equipped

with miniaturized imagers, spectrometers, sampling devices, and chemical detection sensors to conduct in situ measurements of terrain and rock composition, structure, etc. Multiple Microbots would coordinate to share information and cooperatively analyze large portions of a planet's surface or subsurface.

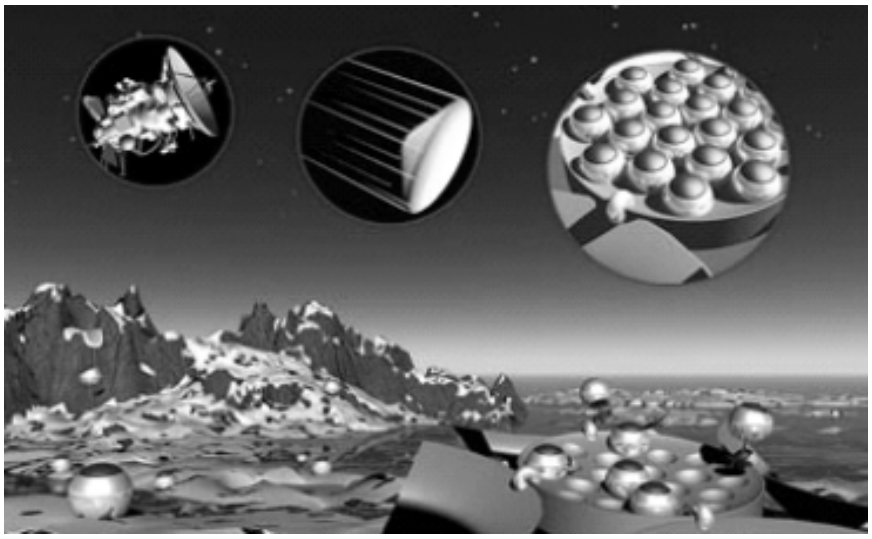

Figure 108: Microbots mission concept. Image rendering by Gus Frederick.

F.3 Microbots Mobility

Basic Microbots hopping mobility is provided by an asymmetric bistable mechanism activated by a DE actuator, see Figure 109 and Figure 110. The main actuator, at the center, is connected to a bistable mechanism not to maintain a state but to rapidly deliver hopping energy. The four outer smaller actuators orient the ball prior to jumping to change its directionality.

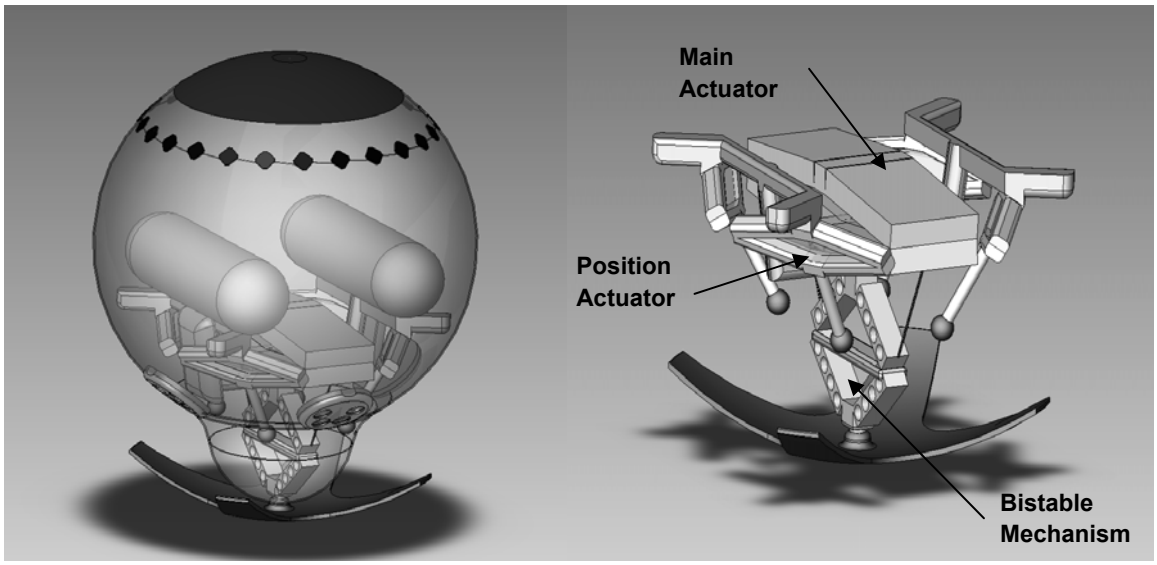

Figure 109: Microbots hopping mechanism.

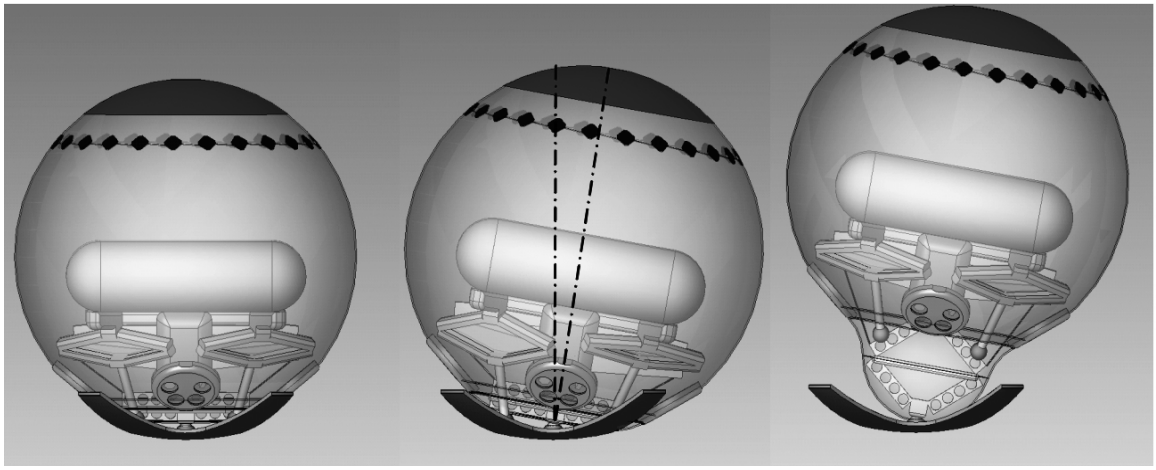

Figure 110: Changing the attitude of the Microbots using the directional hopping mechanism concept.

As seen in Chapter 3, one drawback of DE actuators is their relatively low power which is not compatible with the high energy release rates necessary for hopping motion. In this respect, a bistable mechanism was designed to store or charge DE actuator energy over time to later provide a quick release. A schematic of the system is illustrated on Figure 111 and a working prototype is shown on Figure 112. In the charging phase (between states 1 and 2), the diamond actuator extends and stores energy in an over-the-center bistable mechanism. This bistable mechanism is composed of two beams that

pivot about a common axis, and an extension spring. The actuator is linked to the two beams with Nylon wires (highlighted on the first photograph of Figure 112). The mechanism reaches a stable configuration as the actuator reaches the end of its stroke (state 3). Backlash in the interface between actuator and bistable mechanism allows the actuator to return most of the way to its initial position. Finally, at the end of its return stroke, the actuator unlatches the bistable mechanism from its stable configuration, resulting in a rapid energy release suitable for hopping. The simple prototype shown on Figure 112 uses a 107 mm DE actuators and easily jump its own characteristic height.

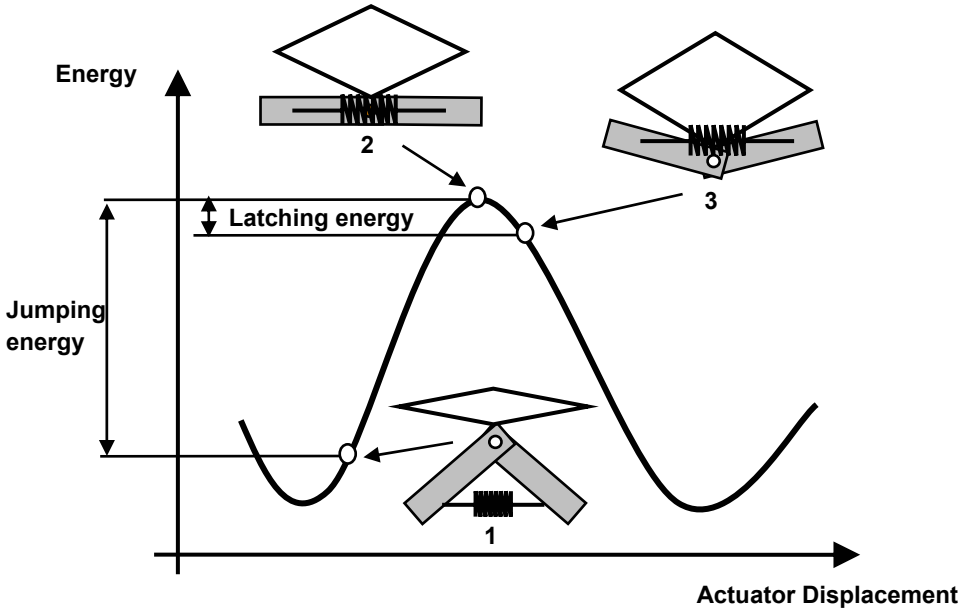

Figure 111: DE actuator hopping mechanism.

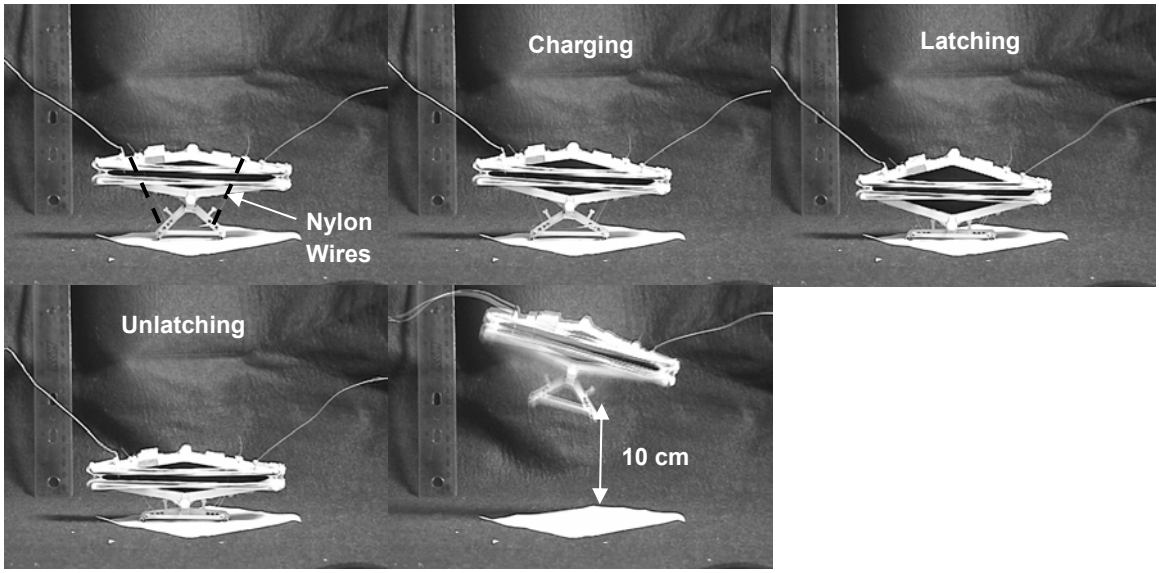

Figure 112: Sequence of images of the mobility system prototype performing a jump. Total cycle time is about 20 seconds.